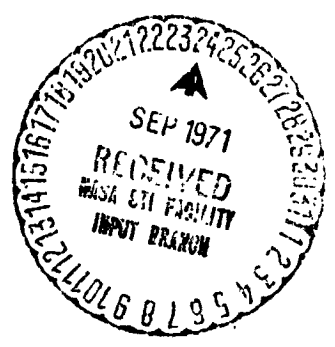9G45-70

# USE of GROUND-TRUTH MEASUREMENTS
# to MONITOR ERTS SENSOR CALIBRATION

## TECHNICAL REPORT NO. 16
## VOLUME II

OCTOBER 1970
CONTRACT NO. NAS 5-10343

ROMEO R. SABATINI
GEORGE RABCHEVSKY

SEP 1971
RECEIVED
NASA STI FACILITY
INPUT BRANCH

**prepared for**

**NATIONAL AERONAUTICS AND SPACE ADMINISTRATION
GODDARD SPACE FLIGHT CENTER
GREENBELT, MARYLAND**

**ALLIED RESEARCH ASSOCIATES, INC.**
VIRGINIA ROAD · CONCORD, MASSACHUSETTS

# USE of GROUND-TRUTH MEASUREMENTS to MONITOR ERTS SENSOR CALIBRATION

## TECHNICAL REPORT NO. 16
## VOLUME II

OCTOBER 1970
CONTRACT NO. NAS 5-10343

ROMEO R. SABATINI
GEORGE RABCHEVSKY

prepared for
NATIONAL AERONAUTICS AND SPACE ADMINISTRATION
GODDARD SPACE FLIGHT CENTER
GREENBELT, MARYLAND

**ALLIED RESEARCH ASSOCIATES, INC.**
VIRGINIA ROAD · CONCORD, MASSACHUSETTS

## FOREWORD

This report is Volume No. II of three volumes containing studies of ERTS Data Management, Dissemination and Processing performed by personnel of ARA for the National Aeronautics and Space Administration, Goddard Space Flight Center, under Contract No. NAS 5-10343. The work described herein is an extension of the studies reported on in Allied Research Associates, Inc. (ARA) Technical Report No. 11, December 1969, entitled "Management, Processing and Dissemination of Sensory Data for the Earth Resources Technology Satellite" by Merritt, et al. The current study involved an investigation of the use of ground-truth data to monitor ERTS sensor calibrations. This monitoring can be conducted at the ERTS Data Center. The authors are indebted to Messrs. E. Merritt and P. Sherr for their review and editing of the report.

ABSTRACT

The Earth Resource Technology Satellite (ERTS) sensors, i. e., the Return Beam Vidicon (RBV) and Multispectral Scanner (MSS), utilize light energy detectors and associated electronics that may be subject to changes in output for a given scene reflectance.

On-board systems for monitoring system response have been provided. However, these monitoring systems are, themselves, subject to change. Additional procedures, therefore, are needed for monitoring of sensor calibration.

A survey of potential ground-truth sites and a review of appropriate literature indicate that it will be possible to monitor ERTS sensor calibrations at the ERTS Data Center. Two alternate procedures are defined which will permit judgements to be made with regard to possible sensor degradation or malfunction.

The first method, simpler from an analysis point of view, requires the periodic overflight of ground-truth sites by an aircraft with sensor systems similar to those on board ERTS. Such flights should be made concurrent with local ERTS passage.

The second technique requires comparisons between radiance values measured by the sensors on ERTS over ground-truth sites and those computed from radiation transfer models using known optical properties of the surfaces at the sites and of the atmosphere. The application of this technique requires repeated on-site measurements of those parameters which are of significance to the radiation transfer process. However, it is possible to select sites in which these physical parameters do not vary significantly in time. For such sites, frequent monitoring of these parameters may not be necessary.

A procedure combining both techniques is proposed. The concept of ground-truth sites is central to this procedure and hence ground-truth site requirements are discussed and site selections are presented. Prelaunch and postlaunch data requirements over these sites are specified. Techniques for the computation of the radiance to be measured over test sites are discussed and sample calculations based on available data are presented. The application of these data in real-time sensor calibration monitoring schemes is specified in detail.

iv

TABLE OF CONTENTS

TABLE OF CONTENTS, contd.

## LIST OF ILLUSTRATIONS

LIST OF ILLUSTRATIONS, contd.

LIST OF ILLUSTRATIONS, contd.

LIST OF ILLUSTRATIONS, contd.

LIST OF TABLES

# 1. INTRODUCTION

The ERTS sensors, i. e. , the Return Beam Vidicon (RBV) and Multi-spectral Scanner (MSS), utilize light energy detectors and associated electronics that may be subject to changes in output for a given scene reflectance. These changes may occur over both short and long time periods. They may be random or periodic. The designers of the RBV and MSS were aware of the possibility of response changes in the system and have provided on-board systems for monitoring system response. However, these monitoring systems are, themselves, subject to change. Additional procedures, therefore, are needed for monitoring of sensor calibration. In this study we have examined the hypothesis that measurements made at selected ground-truth sites and/or measurements made of selected sites appearing in the RBV/MSS imagery (as reproduced on photographic film or as digital products) can provide an appropriate ERTS Data Center calibration monitoring system.

## 2. SUMMARY

A survey of potential ground-truth sites and a review of appropriate literature indicate that it will be possible to monitor ERTS sensor calibrations at the ERTS Data Center. Two alternate procedures are defined which will permit judgements to be made with regard to possible sensor degradation or malfunction.

The first method, simpler from an analysis point of view, requires the periodic overflight of ground-truth sites by an aircraft with sensor systems similar to those on board ERTS. Such flights should be made concurrent with local ERTS passage. Although it would be desirable to have ground resolutions in the aircraft data approximate those obtained by the satellite, it is not essential if the aircraft ground-truth data are obtained over a large site having relatively uniform surface characteristics. By means of these periodic aircraft overflights, the surface reflectance of a ground-truth site can be monitored and reflectance changes noted which can then be related to possible corresponding changes in the ERTS imagery. Changes in calibration of the aircraft sensors can of course be detected through frequent calibration checks on the ground.

The second technique requires comparisons between radiance values measured by the sensors on ERTS over ground-truth sites and those computed from radiation transfer models using known optical properties of the surfaces at the sites and of the atmosphere. The application of this technique requires repeated on-site measurements of those parameters which are of significance to the radiation transfer process. However, it is possible to select sites in which these physical parameters do not vary significantly in time. For such sites, frequent monitoring of these parameters may not be necessary.

It is significant to note that the proposed techniques can be complementary. In fact, we propose that a procedure combining both techniques be adopted. The resulting scheme will be useful not only in the monitoring of sensor calibration, but also in furthering our understanding of the radiative properties of surface materials and the atmosphere.

The concept of ground-truth sites is central to the proposed calibration monitoring scheme. Consequently, in the following sections, ground-truth site requirements are discussed and site selections are presented. Prelaunch and postlaunch data requirements over these sites are specified. Techniques for the computation of the radiance to be measured over test sites are discussed and sample calculations based on available data are presented. Finally, the application of these data in real-time sensor calibration monitoring schemes is specified in detail.

# 3. EXPECTED RADIANCE AT SATELLITE SENSORS

The surface characteristics and the atmospheric conditions determine, in general, the energy flux measured by a spacecraft sensor for a given solar position. This section presents the results of calculations of the expected energy flux, available in the RBV and MSS channels over various ground test-site surfaces similar to those described in Section 4 and Appendix A. The calculations are for both a "clean" (Rayleigh) and a "turbid" atmosphere. In order to perform these calculations, the solar irradiance, atmospheric transmissivity, and the atmospheric contribution to the satellite-measured radiances in the spectral intervals corresponding to the channels of the RBV and MSS were derived from existing data. These data and the method of computation are discussed below. Also presented in this section are comparisons between radiances derived from actual aircraft measurements and radiances computed from model atmospheres. The results of these comparisons suggest that the computation scheme discussed in this section can be effectively used to provide "simulated" data for the monitoring of satellite sensor degradation.

## 3.1 Spectral Characteristics of the RBV and MSS Sensor Systems

The spectral responses of the RBV and the MSS instruments on ERTS-A are shown in Figures 1a and 1b (Hovis, personal communication, September 1970). These data are first approximations as further calibration tests are needed. However, in the absence of final calibration curves, we made use of the data shown in computations of expected radiances discussed in subsequent paragraphs. It is evident from the longwave cutoff of the spectral response functions that the two sensors are designed to measure the solar radiation reflected by the earth-atmosphere system and attenuated by the atmosphere through the processes of absorption and scattering.

## 3.2 Spectral Reflectance of Test-Site Covers

Appendix C is a detailed discussion of the factors affecting reflectance of test sites. Surface reflectance is discussed in Appendix C with regard to:

1. Semi-desert and desert vegetation
2. Soils
   a. Soil Texture
   b. Soil Moisture
   c. Humus and Iron Oxide Content

3

      d.    Mineralogical Composition

      e.    Soluble Salt Content

3.    Surface Structure

4.    Influence of Weathering on Surface

The following is a brief summary of the most important surface factors affecting reflectance:

1.    Soil components which lower the general reflection of visible light are humus and iron oxides.

2.    Components which give rise to an increase in general reflectance include quartz, carbonates, bicarbonates, chlorides, kaolinite and alumina.

Typical surfaces used in the calculations shown later in this section are shown in Table 2. Reflectance curves for these surfaces are shown in Appendix B.

## 3.3 Solar Elevation Angle and Atmospheric Optical Thickness

The Earth Resources Technology Satellite (ERTS) is scheduled to be launched into a sun-synchronous polar orbit passing overhead at 9:30 a.m. local time (10:00 a.m. local time at the latest). Figures 2a and 2b give the range of solar elevation angles expected throughout the year over the coterminous United States at 9:30 a.m. and 10:00 a.m. The graphs were drawn from data given in the Smithsonian Meteorological Tables (Ref. 4).

The variations in solar elevation cause variations in the path length traversed by a solar ray through the atmosphere to reach the ground, i.e., the optical thickness or optical air mass. More precisely, the optical air mass, m, is expressed as a multiple of the path length for a light source at the zenith and is related to the solar elevation angle, $\theta$, by

$$m = \frac{1}{\sin\theta} \cdot \tag{1}$$

This relationship is graphically illustrated in Figure 3. Also shown in Figure 3 are the extreme values of m for $40^{\circ}$N latitude computed for 9:30 a.m. Since the optical air mass over the coterminous United States is expected to range from 1.2 to 4, it is evident that the effects of the solar elevation angles must be included in computations of expected irradiance. In the actual computations discussed in subsequent paragraphs, the air mass effect is incorporated implicitly by using calculated slant-path atmospheric transmissivities which are dependent on the solar elevation angle $\theta$.

4

In addition to the air mass effect, there is a second effect dependent on the solar elevation angle which needs to be considered. Simply stated, this effect may be called the "sin θ" decrease in solar irradiance resulting from non-normal incidence. Consider a "beam" of solar radiation of ur.t cross section area, say 1 cm$^2$, and total radiant power of P watts. The power density or irradiance of this beam at normal incidence, i.e., θ = 90°, would be P watts/cm$^2$. However, at θ ≠ 90°, the area of the surface intercepted by the "beam" is (sin θ)$^{-1}$ cm. Since the total power remains at P watts, the irradiance at θ is then given by P/(sin θ)$^{-1}$ or P sin θ watts/cm$^2$. It is therefore clear that

$$I(\theta) = I(\theta = 90°) \sin \theta \qquad (2)$$

where I(θ) and I(θ = 90°) are respectively the irradiance at an elevation angle of θ and the irradiance at normal incidence. It should be pointed out that Eq. (2) holds at the top of the atmosphere as well as at the surface of the earth.

### 3.4 Solar Irradiances and Atmospheric Transmissivities for "Clean" (Rayleigh) and Turbid Atmospheres

The mcst important factor affecting solar radiation through the atmosphere is scattering. For a molecular or "clean" atmosphere, the spectral attenuation follows Rayleigh's Law; i.e., the scattering is inversely proportional to the 4th power of the wavelength of radiation. The curves in Figure 4 show the scattering attenuation effect on solar radiation through a Rayleigh atmosphere. These curves were constructed from data given by Kondrat'yev (Ref. 1). They show the solar irradiance at the earth's surface at normal incidence through different atmospheric optical thicknesses, m, and for the irradiance at the top of the atmosphere (Ref. 3).

A more realistic picture of the solar irradiance at the surface of the earth is obtained by including the effect of scattering and absorption by aerosols and gases in a turbid atmosphere. The curves in Figure 5 from P. Moon (Ref. 2), show the solar irradiance at the earth's surface at normal incidence through different atmospheric optical thicknesses. These curves were derived from actual measurements made by various investigators and included the effects of aerosol scattering and absorption.

The curves in Figure 4 and Figure 5 are presented here to show graphically the effects of a Rayleigh and turbid atmosphere on solar radiation reaching the ground. The format of the data, however, is not sufficiently flexible to permit their use in detailed computations of expected radiances within limited spectral intervals. In

our calculations we used instead the spectral transmissivity data tabulated by Elterman (Ref. 5) for a dry Rayleigh and a dry turbid atmosphere, and Fowler's (Ref. 4) absorption data for the water vapor bands between 0.70 and 0.74 μm, 0.79 and 0.84 μm, 0.86 and 0.99 μm, and 1.03 and 1.23 μm. Figures 6a and 6b show the air mass or solar elevation effect on the transmission coefficient through a Rayleigh atmosphere and a dry turbid atmosphere. Figure 7 shows Fowler's data for various amounts of atmospheric water vapor expressed in terms of precipitable water (w) defined as

$$w = \frac{1}{D}\int \rho_v(z)dz \qquad (3)$$

where

$\rho_v(z)$  is the vertical distribution of absolute humidity

and

D  is (a) the density or (b) the specific gravity of liquid water

In the first instance, w would be in units of cm-precipitable water while in the second instance, w would be in units of  $g/cm^2$. For a given distribution of $\rho_v(z)$, the two definitions of w are numerically equal and in essence specify the liquid water equivilent of the total water vapor in a vertical column of atmosphere of unit area in cross section. As a point of reference, the U. S. Standard Atmosphere contains 1.9  $g/cm^2$ of precipitable water. For the specified surface temperature of $15^oC$ and a lapse rate of $6.5^o/km$, this value of w corresponds to a mean relative humidity of 63% from the surface to 10 km. Other typical values of w are 0.5 to 1.0  $g/cm^2$ for a mid-latitude winter atmosphere and 2.5 to 3.0  $g/cm^2$ for a mid-latitude summer atmosphere. The effects of these variabilities in atmospheric moisture on computations of expected radiances in spectral regions containing the absorption bands may be seen in Table 1. In this table, atmospheric transmissivities, computed from Elterman's Turbid Model, for the four water vapor absorption bands have been corrected for attenuation by different amounts of water vapor as specified by the equivalent precipitable water contents.

## 3.5  Method of Calculations

The basis for our calculations for the radiances measured by the RBV and MSS sensors are:  (1)  The curve of solar irradiance at the top of the atmosphere shown in Figure 4;  (2)  slant-path atmospheric transmissivities shown in Figure 6a for Rayleigh and turbid atmospheres, appropriately corrected for 2 $g/cm^2$ of precipitable water;  and (3)  the spectral responses of the RBV and MSS instruments given in Figures 1a and 1b.

6

TABLE 1

TRANSMISSIVITIES OF A TURBID ATMOSPHERE (Elterman, Ref. 5) CORRECTED

FOR WATER VAPOR CONTENT, IN THE NEAR INFRARED BANDS

| Limits of Absorption Band, μm | No Moisture | | | | Precipitable Water | | | | | | | | | | | | | | | |
|---|---|---|---|---|---|---|---|---|---|---|---|---|---|---|---|---|---|---|---|---|
| | | | | | 0.5 g/cm² | | | | 1.0 g/cm² | | | | 2.0 g/cm² | | | | 3.0 g/cm² | | | |
| | | | | | | | | | Solar Elevation Angle | | | | | | | | | | | |
| | 90° | 60° | 42° | 20° | 90° | 60° | 42° | 20° | 90° | 60° | 42° | 20° | 90° | 60° | 42° | 20° | 90° | 60° | 42° | 20° |
| 0.70 - 0.74 | 88 | 86 | 82 | 68 | 87 | 84 | 79 | 64 | 87 | 83 | 78 | 63 | 84 | 81 | 76 | 59 | 82 | 80 | 74 | 54 |
| 0.79 - 0.84 | 89 | 87 | 85 | 72 | 87 | 85 | 81 | 68 | 85 | 84 | 80 | 67 | 83 | 81 | 78 | 62 | 80 | 79 | 75 | 56 |
| 0.86 - 0.99 | 90 | 88 | 86 | 74 | 80 | 78 | 75 | 62 | 78 | 76 | 72 | 57 | 73 | 71 | 67 | 50 | 69 | 67 | 62 | 48 |
| 1.02 - 1.23 | 91 | 89 | 88 | 77 | 82 | 80 | 77 | 64 | 78 | 76 | 72 | 59 | 72 | 71 | 67 | 53 | 70 | 67 | 62 | 48 |

Figure 8 shows schematically the significant factors which ultimately determine the radiance reaching a satellite sensor. This radiance consists principally of two parts. The first is that portion of the solar irradiance scattered by the atmosphere in the direction of the sensor prior to reaching the surface of the earth. In Figure 8, this component of the expected radiance is denoted by $R_A$. The second part consists of that portion of the solar irradiance which reaches the surface of the earth and is reflected out to space in the direction of the sensor. In Figure 8, this component is denoted by $R_s$. The total radiance, $R_\theta$, reaching the satellite sensor is then given by

$$R_\theta = R_s + R_A. \tag{4}$$

For a given spectral interval, $\lambda_1 \leq \lambda \leq \lambda_2$, corresponding to the spectral response limits of any one of the channels of either of the ERTS sensors, the solar irradiance $I_\theta$ reaching the surface of the earth is given by

$$I_\theta = \sin \theta \int_{\lambda_1}^{\lambda_2} I(\lambda) \, T_\theta(\lambda) \, d\lambda \tag{5}$$

where

$I(\lambda)$ is the spectral solar irradiance at the top of the atmosphere and at normal incidence (see Figure 4)

and

$T_\theta$ is the monochromatic one-way transmissivity of the atmosphere (Figure 6b) at an elevation angle $\theta$, i.e., $T_\theta(\lambda)$ includes the air mass effect corresponding to a solar elevation angle $\theta$.

The "$\sin \theta$" term in Eq. (4) describes the "$\sin \theta$" spreading effect discussed in Section 3.3.

A fraction of the irradiance defined by Eq. (5) is reflected by the surface in the direction of the satellite sensor. The fraction reflected, defined as the reflectance, is a function of the surface material and, generally, is a function also of the angle of incidence and the viewing angle. For a perfectly diffused reflecting surface (i.e., a Lambertian surface), the reflectance is independent of angle of incidence or of view. The reflectances of natural surfaces, at high solar elevation angles, approximate that of a diffused reflector. In our computations, we have made use of this approximation and assumed that the reflectances, $r(\lambda)$, are dependent only on wavelength and not on angle. With this Lambertian assumption the ratio of the radiation reflected in the direction of the satellite sensor to the total radiation reflected into the whole

8

upper hemisphere above the reflecting surface is given by $(\pi)^{-1}$. For a nadir-viewing satellite sensor then, the reflected radiance it receives from the reflecting surface alone is

$$R_s = \frac{\sin \theta}{\pi} \int_{\lambda_1}^{\lambda_2} I(\lambda)\, T_\theta(\lambda)\, T_Z(\lambda)\, r(\lambda)\, \phi(\lambda)\, d\lambda \text{ watts meter}^{-2}\text{ster}^{-1} \quad (6)$$

where the significance of $\sin \theta$, $(\pi)^{-1}$, $I(\lambda)$, $T_\theta(\lambda)$ and $r(\lambda)$ have been discussed previously. The term $T_Z(\lambda)$ describes the monochromatic transmissivity of the atmosphere in the zenith direction for the solar radiation reflected by the surface to the nadir-viewing sensor. $\phi(\lambda)$ is the spectral response function of the sensor channel in question as presented in Section 3.1.

Finally, to obtain $R_\theta$ we must add to Eq. (6) the contribution of the scattered atmospheric radiation to space, $R_A$. The intensities of the solar radiation scattered to space by the atmosphere have been computed by a number of investigators using classical techniques in small particle scattering and model atmospheres. Fraser (Ref. 6), on the other hand, has computed what are essentially reflectances, or Specific Intensities, for the atmosphere. We have found it appropriate to use his data for a continental atmosphere. Figure 9 shows the specific intensity curves constructed from Fraser's data. With the definition of Specific Intensity as given by Fraser, the contribution by atmospheric scattering is then

$$R_A = \frac{1}{\pi} \int_{\lambda_1}^{\lambda_2} I(\lambda)\, J_\theta(\lambda)\, \phi(\lambda)\, d\lambda \text{ watts meter}^{-2}\text{ster}^{-1} \quad (7)$$

where the significance of the terms $I(\lambda)$, $\pi$, and $\phi(\lambda)$ are as discussed previously for Eq. (6). The term $J_\theta(\lambda)$ is the Specific Intensity of Fraser. The $\theta$ subscript denotes its dependence on solar elevation. By comparing Eq. (7) with Eq. (6) the equivalence of $J_\theta(\lambda)$ and $r(\lambda)$ is readily seen.

By combining Eqs. (4), (6) and (7), the total radiance measured by a channel of the RBV or MSS with spectral response function, $\phi_\lambda$, is given by

$$R_\theta = \frac{1}{\pi} \int_{\lambda_1}^{\lambda_2} \phi(\lambda)\, I(\lambda) \left[ T_\theta(\lambda)\, T_Z(\lambda)^{n(\lambda)} \sin \theta + J_\theta(\lambda) \right] d\lambda. \quad (8)$$

Eq. (8) provides the basic form of the radiation transfer from which we computed the expected radiances for the various channels. In practice, however, the integration indicated in the equation was replaced by summation of finite differences. Furthermore, wherever appropriate, the wavelength dependences of the parameters

in the equation were replaced by mean values averaged over the spectral interval
defined by the spectral response function.

To illustrate the computation method we shall present a calculation for the
total radiance, $R_\theta$, measured by Channel 1 of the MSS, at solar elevation angle
$\theta = 60^\circ$, over a water surface and through a turbid atmosphere. We shall use
average transmissivities, reflectance, and instrument spectral response over the
range of 0.5 to 0.6 μm to evaluate the terms in Eq. (7). The use of the averages is
justified by the absence of large variations of the above parameters in the 0.5 to
0.6 μm interval. Thus we have the following values:

$$\overline{T}_{(\theta = 60)} = \quad 0.78 \quad \text{(from Figure 6b)}$$

$$\overline{T}_Z = \quad 0.81 \quad \text{(from Figure 6 b)}$$

$$\overline{r} = \quad 0.03 \quad \text{(from Figure B-19, Appendix)}$$

$$\overline{\phi} = \quad 0.87 \quad \text{(from Figure 1b)}$$

where the over-bar denotes averaging over wavelength. In addition, the data in
Figure 9 shows that

$$J_{(\theta = 60)} \simeq \quad 0.05.$$

With these averaged values, Eq. (8) becomes

$$R_A \simeq \frac{1}{\pi} [\, \overline{\phi}_\lambda \, (\sin \theta \, \overline{T}_\theta \, \overline{T}_Z \, \overline{r} + \overline{J}_\theta \,] \int_{\lambda_1}^{\lambda_2} I_\lambda \, d_\lambda$$

$$\simeq \left[ \frac{\overline{\phi}_\lambda \, (\sin \theta \, \overline{T}_\theta \, \overline{T}_Z \, \overline{r} + \overline{J}_\theta) \sum_i (I_\lambda)_i \, \Delta \lambda}{\pi} \right]. \tag{9}$$

Using the data from Figure 4, we obtained

$$\sum (I_\lambda)_i \Delta \lambda \simeq 190 \text{ watts meter}^{-2}.$$

Then substituting the indicated mean values into Eq. (9) and the appropriate values
for $\theta = 60^\circ$ and $\pi$, we obtained

$$R_{\theta = 60} \text{ (Channel 1 of MSS)} = 3.4 \text{ watts meter}^{-2} \text{ster}^{-1}$$

for measurements made over a water surface. Similar calculations were performed
for all of the channels of the RBV and MSS with $\theta = 60^\circ$, $42^\circ$, $20^\circ$ and for reflectance

values corresponding to a number of different types of natural surfaces. (The selection of $\theta$ = 42° was made because at 42°, m = 1.5 which made it easy to evaluate the transmissivity terms.) For reference, we also computed the expected radiances over a surface of unit reflectance as measured through a Rayleigh and a turbid atmosphere. The results of this set of reference calculations are shown in Figures 11 through 14. Typical expected radiance values from natural surfaces are shown in Figures 15 through 21*. The data are for a turbid atmosphere with 2 $g/cm^2$ of moisture and for the surfaces given in Table 2 which include some of the types of surfaces found at the test sites discussed in Section 4. Laboratory and in situ reflectance measurements available in the literature have been used. Appendix B shows a collection of reflectance curves for natural surfaces obtained from the literature (Refs. 7 through 17). The calculated radiance curves for natural surfaces in Figures 15 through 21 are identified with a figure number referring to the reflectance curve used in the calculations.

TABLE 2

TYPES OF SURFACES USED IN THE CALCULATIONS

| | |
|---|---|
| Black Loam Soil | Coulson (Ref. B-3) Figure B-15 |
| Desert Sand | Coulson (Ref. B-3) Figure B-11 |
| Flood Plain Gravel | Orr, et al (Ref. B-6) Figure B-14 |
| Salt Bed | Ashburn and Weldon (Ref. B-4) Figure B-13 |
| Snow | Kondrat'yev, et al (Ref. B-9) Figure B-21 |
| Weathered Tuff Bedrock | Orr, et al (Ref. B-6) Figure B-14 |
| Vegetation Average | Kondrat'yev, et al (Ref. B-9) Figure B-17 (Average of Curves #1, 2 and 3) |
| Water | Kondrat'yev (Ref. B-8) Figure B-19 |
| Brush and Windblown Sand | Ashburn and Weldon (Ref. B-4) Figure B-13 |

---

*Figures 15-21 also present comparative calculations based on aircraft observations taken by Hovis. These calculations are represented as △, ▢, or ○ along the 60° solar elevation line.

11

## 3.6  Brief Discussion of Results

### 3.6.1  Effects of Turbidity and Solar Elevation Angle

Radiances calculated for the turbid atmosphere, defined by Elterman (Ref. 5) and modified by the addition of 2 $g/cm^2$ of water vapor, were approximately two-thirds of the radiances for a Rayleigh atmosphere and decrease with decreasing solar elevation angles, but less rapidly with decreasing surface reflectances.

An increase in path length (with decreasing solar elevation angles) causes an increase in the moisture and aerosols encountered by the radiation and, therefore, a corresponding decrease of the transmissivities and radiances measured.

A decrease (increase) of atmospheric water vapor from the 2 $g/cm^2$ used in our calculations results in an increase (decrease) in the energy measured by the RBV Channel 3 and MSS Channels 3 and 4.  These are the three channels having spectral response function spanning water-vapor absorption bands.  The effects of atmospheric water-vapor content on these channels are shown in Table 3  in which are tabulated the percentage departures of expected radiances from a referenced atmosphere having a water-vapor content of 2.0  $g/cm^2$ precipitable water.  These percentage-departure values are based on expected radiances, $R_\theta$, computed for measurements made through a turbid atmosphere over a surface with unit reflectance.  Because the $R_A$ term in Eq. (8) is generally insignificant, the contribution by atmospheric scattering to the expected radiance was neglected in these calculations.

A deviation of the aerosol distribution from that used by Elterman (see Figure 6b) would change the transmissivity of the atmosphere and correspondingly, the calculated radiances.  By comparing Figure 6a with Figure 6b, we estimate that by doubling (halving) the aerosol content of the atmosphere the radiance measured by the RBV and MSS channels would roughly decrease (increase) by 10 to 15% at high and moderate solar elevation angles with a bright scene.  However, we do not have the data to compute accurately the expected variability of the radiance assumed over test sites resulting from a variable atmospheric aerosol content.  An aircraft and ground-based measurement program such as that discussed in Section 2 should be useful in obtaining such data.

Changes in ozone distribution do occur with season and latitude.  These changes are not large enough to affect the calculations appreciably since the spectral regions of interest are located away from significant ozone absorption bands.

12

TABLE 3

EFFECT OF ATMOSPHERIC MOISTURE ON RADIANCE CALCULATIONS FOR A BRIGHT SCENE*

| | Precipitable Water | | | | | | | | | | | |
| | No Moisture | | | 0.5 g/cm² | | | 1.0 g/cm² | | | 3.0 g/cm² | | |
| | Solar Elevation Angle | | | | | | | | | | | |
| | 60° | 42° | 20° | 60° | 42° | 20° | 60° | 42° | 20° | 60° | 42° | 20° |
|---|---|---|---|---|---|---|---|---|---|---|---|---|
| RBV #3 | + 6 | + 6 | + 9 | + 4 | + 4 | + 6 | + 2 | + 2 | + 4 | - 2 | - 2 | - 4 |
| MSS #3 | + 6 | + 6 | + 9 | + 4 | + 4 | + 6 | + 3 | + 3 | + 3 | - 2 | - 2 | - 5 |
| MSS #4 | +18 | +35 | +45 | +14 | +18 | +22 | +10 | +10 | +14 | - 7 | - 8 | - 9 |

* Results are in percentage departure from calculations for a turbid atmosphere as defined by Elterman with 2 g/cm² of moisture added.

13

### 3.6.2 Effects of Reflectance Variation

Natural surfaces vary widely in their reflective properties, the variation being in terms of both total reflectance and dependence of reflectance on wavelength, angle of incidence, angle at which the surface is viewed and the physical character of the surface itself (see Section 2 and Appendix A for discussion of surface types).

The dependence of reflectance on the angle of incidence and angle of view has been strikingly illustrated in the work by Coulson (Refs. 7, 8, 9 and 10) and Ashburn, et al. (Ref. 14). From Coulson's data, spectral reflectance curves of various natural substances have been drawn for the nadir viewing situation and for various angles of incidence of the radiation. These are shown in Appendix B. These laboratory and in situ measurements show that even for viewing in the nadir direction, there is an increase in the reflectances of most natural surfaces especially sand and vegetation at low solar elevation angles.

All calculations presented here, except for desert sands and water, assumed Lambert surface diffuse reflectance, a condition which is approximately met in nature for radiation toward the zenith and for high to medium solar elevation angles. The actual values used were taken from Coulson's data.

The calculations for desert sand and water included the variation of reflectances with solar elevation angle which explain the slightly different slope of the radiance curves for these surfaces in Figures 15 through 21.

Because of a general increase in reflectances with lower solar elevation angles, the calculated radiances shown in Figures 15 through 21 would be slightly higher at the lower solar angles.

### 3.6.3 Relative Contrast of the RBV and MSS Video

Assuming that the densities on the video are approximately linear with radiances and solely on the basis of the available radiances in each RBV and MSS channel obtained from our calculations for typical surfaces, we can draw the following general conclusions.

1. Vegetation and water produce nearly similar low radiances and, therefore, are almost undifferentiated in all channels except MSS 4 and RBV 3 where the high reflectances of vegetation in the near infrared makes it brighter than water and most soils.

2. MSS 4 has the highest radiance values and the highest differentiation between surfaces. This channel should produce the highest contrast information.

14

3.   Over any given surface, RBV 3 has the lowest radiance values of all of
the channels.  Low contrast pictures are to be expected.  However, vegetation can
be expected to be clearly delineated in the pictures.

3.7  Comparison of the Calculated Radiances to Aircraft Spectrometer
     Measurements

In this section the computations presented in Section 3.5 are compared with
some actual aircraft measurements.  Figures 22, 23 and 24 from Hovis (Refs. 18
and 19) show spectral distributions of solar reflected energy measured by a spectro-
meter in an aircraft over ocean waters, a forested area and a mature wheat field.
From these curves the total energy measurable in each of the RBV and MSS spectral
bands was calculated as follows:

1.   The curves were integrated graphically for the total energy in each RBV
and MSS band using the spectral response functions shown in Figures 1a and 1b.

2.   An atmospheric transmissivity factor, calculated from data by Elterman
(Ref. 5) and corrected for water-vapor effects, was applied to the energy measured
in (1) to account for the depletion of the atmosphere from the airplane to space.
The amount of water vapor used was also computed from the airplane altitude to
space using the standard atmosphere with mean relative humidity of 63% up to 10 km
(see Section 3.4).

3.   The contribution of the scattered radiation from the atmosphere outward
to space, $R_A$, was added.  This term is a fraction of the values given in Figure 8
since some of the scattered atmospheric radiation is already implicit in the aircraft
data.  The actual values were estimated from optical thickness data given by Elterman
(Ref. 5).  From a height of 1 km it is about 65% for RBV 1 and MSS 1 and 55% for the
other channels.  From 3 km it is 35% for RBV 1 and MSS 1 and 25% for all other
channels.

The calculations from these aircraft measurements are presented as indi-
vidual points on the graphs of Figures 15 through 21.  The calculated radiance for a
water surface using aircraft measurements in all cases correspond quite closely to
the values computed from the model atmosphere.  The differences shown in Figures
17, 20 and 21 between the calculated radiances for vegetation and those deduced from
Hovis' aircraft measurements over forested mountains are most probably due to the
lower reflectance of the forested mountains than the averaged reflectance assumed
for vegetation using data from Figure B-16 (~40% for the near infrared.)

15

No aircraft spectrometer measurements over desert regions are available
at present, but such measurements are planned for the very near future (Hovis,
Ref. 19, personal communication). These should be made over uniform desert
surfaces, such as described in Section 4, large enough to be seen from satellite
heights. These aircraft measurements, when interpreted with measurements made
at the surface, should provide information of the expected magnitude of variability
in satellite-measured radiance over the test sites resulting from a variable atmos-
phere. Conversely, if measurements of the optical properties of the atmosphere
are measured by the aircraft or measured independently by lidar or other techniques,
the aircraft measurements can be used to deduce surface reflectance values. The
computation technique discussed in this section, coupled with aircraft spectrometer
measurements from which surface reflectances for the test sites can be derived,
can provide extremely useful data for the monitoring of satellite sensor calibration.
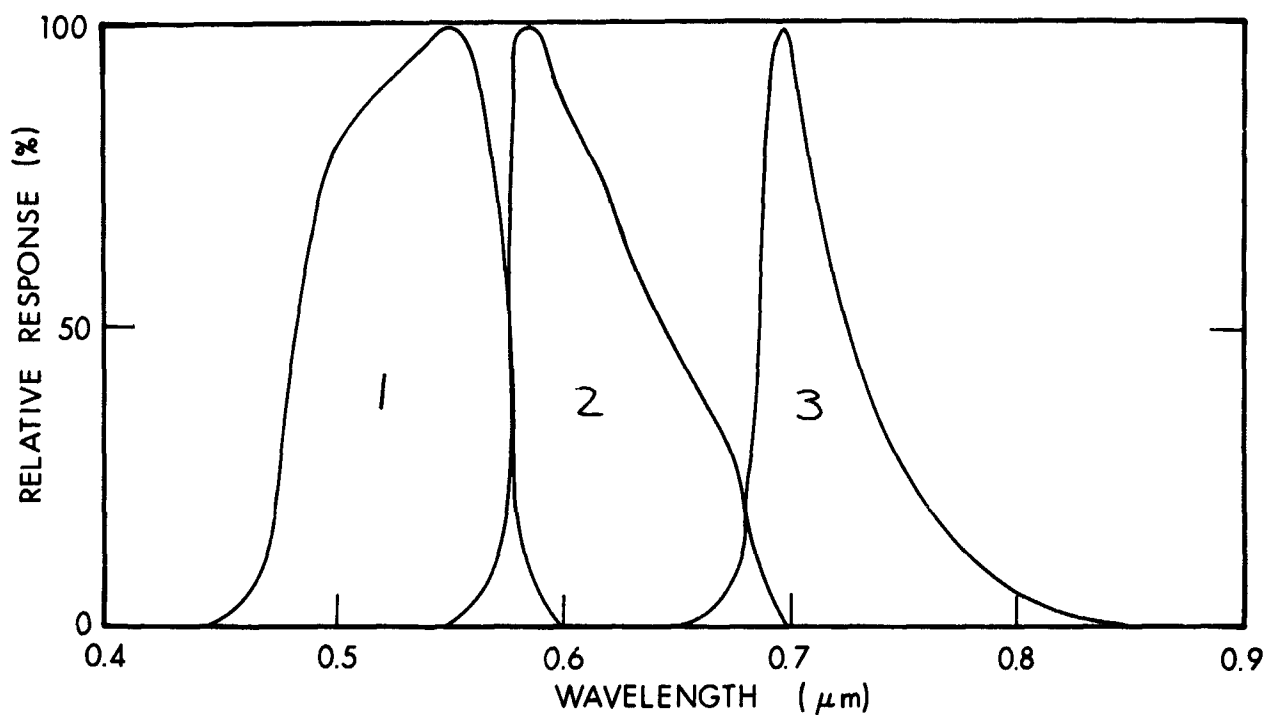
Figure 1a    Spectral Response for ERTS-A Return Beam
Vidicon (RBV).
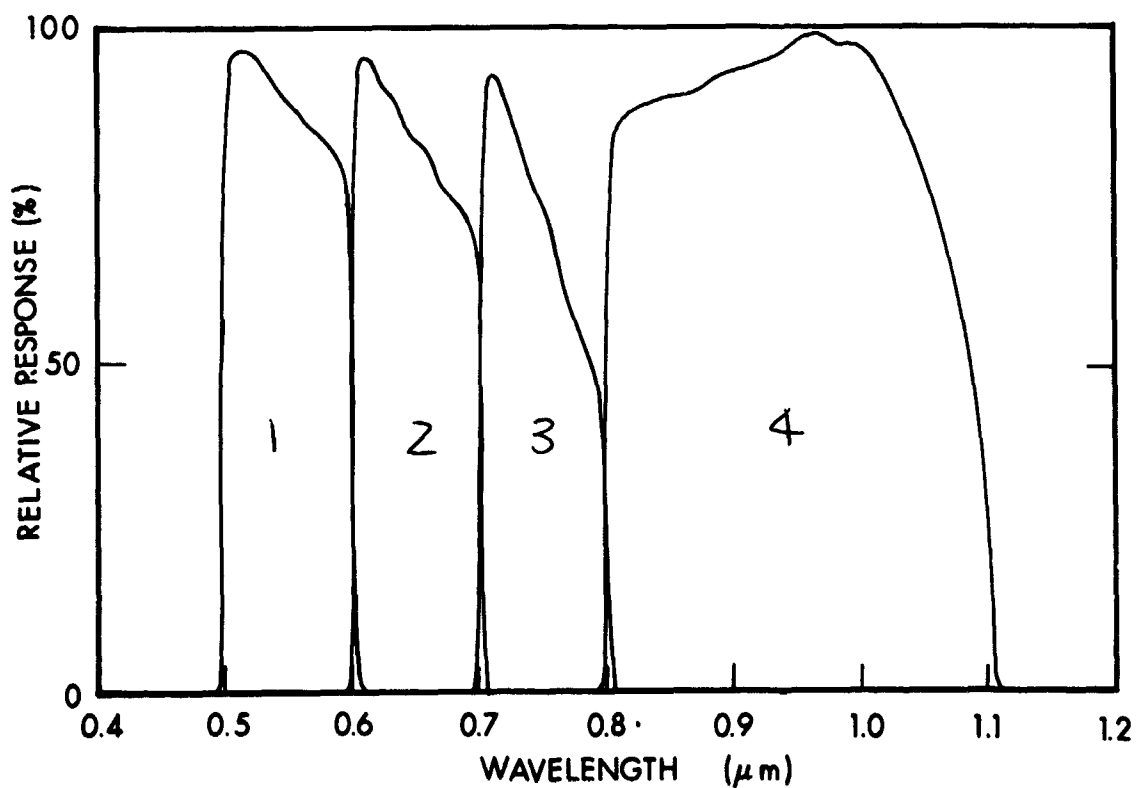


Figure 1b    Spectral Response for ERTS-A Multi-Spectral
Scanner (MSS).
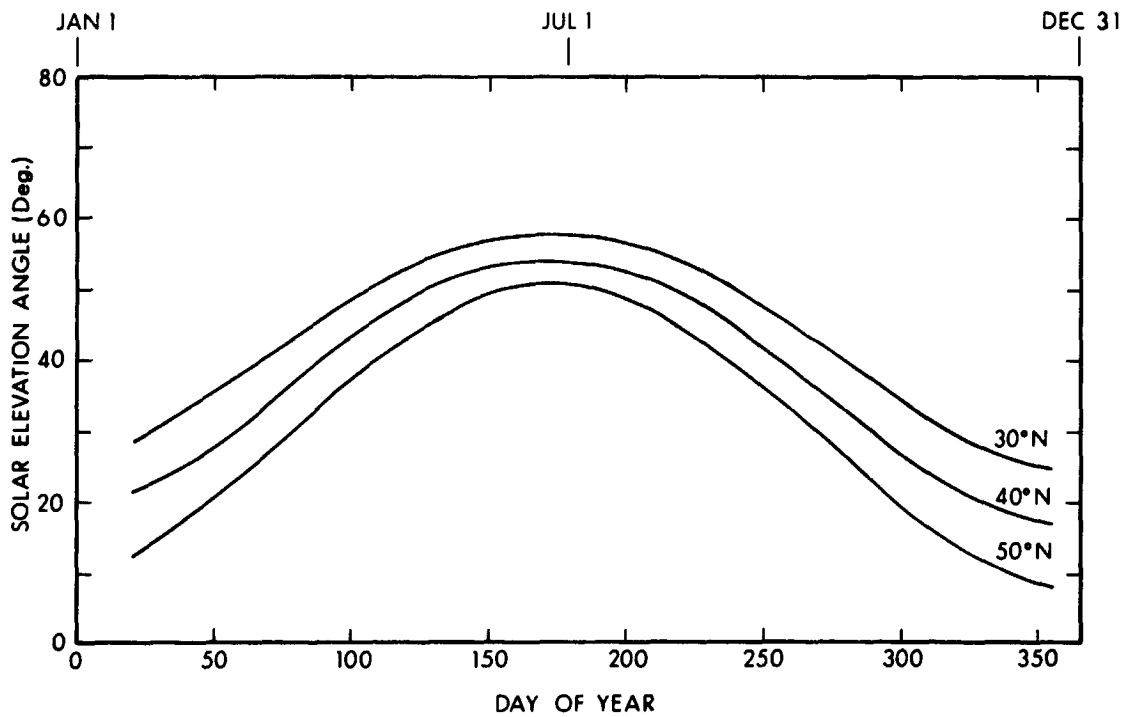
Figure 2a   Solar Elevation Angles at 9:30 AM at 30°, 40°
and 50°N Latitude.
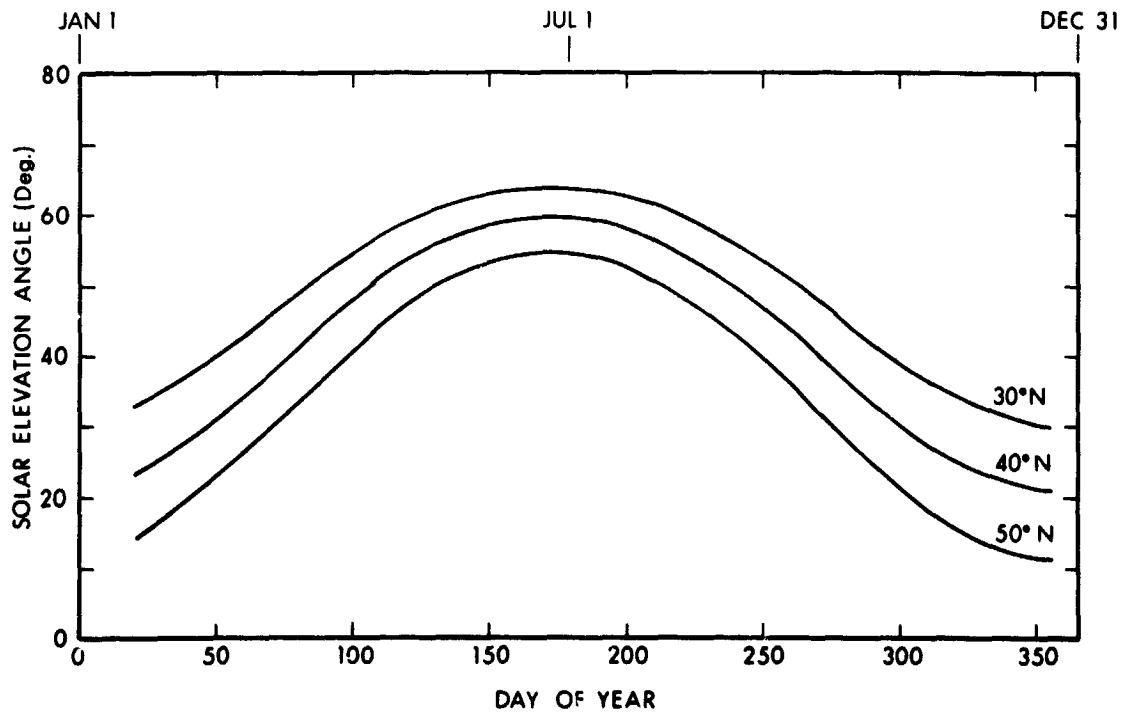


Figure 2b   Solar Elevation Angles at 10:00 AM at 30°, 40°
and 50°N Latitude.

18
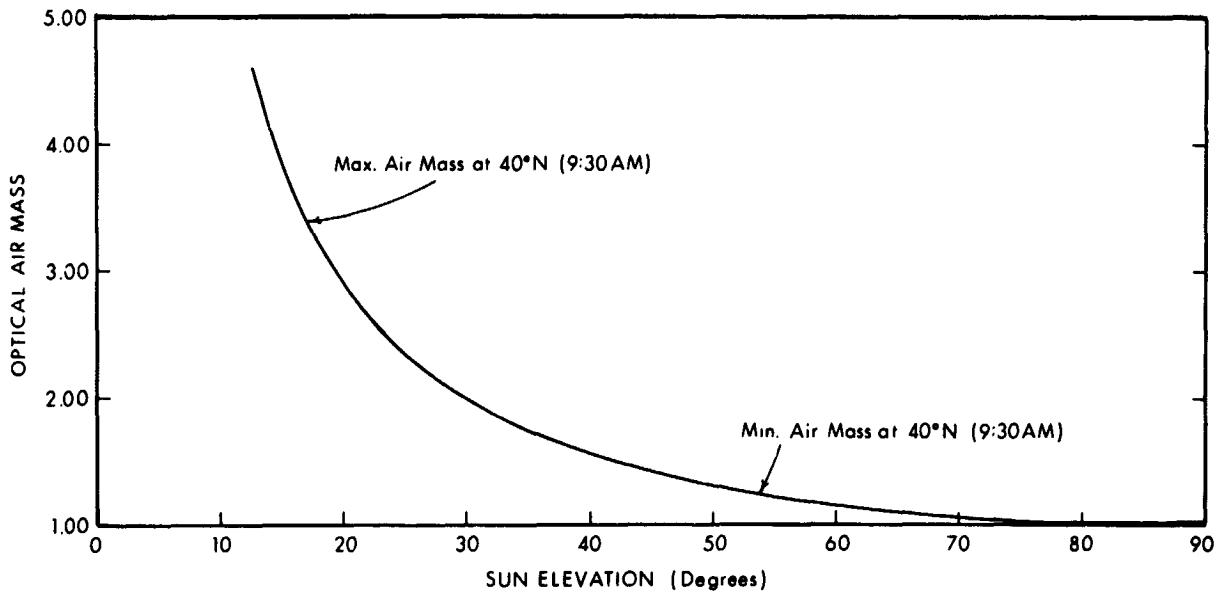
**Figure 3    Air Masses for Different Solar Elevations.**
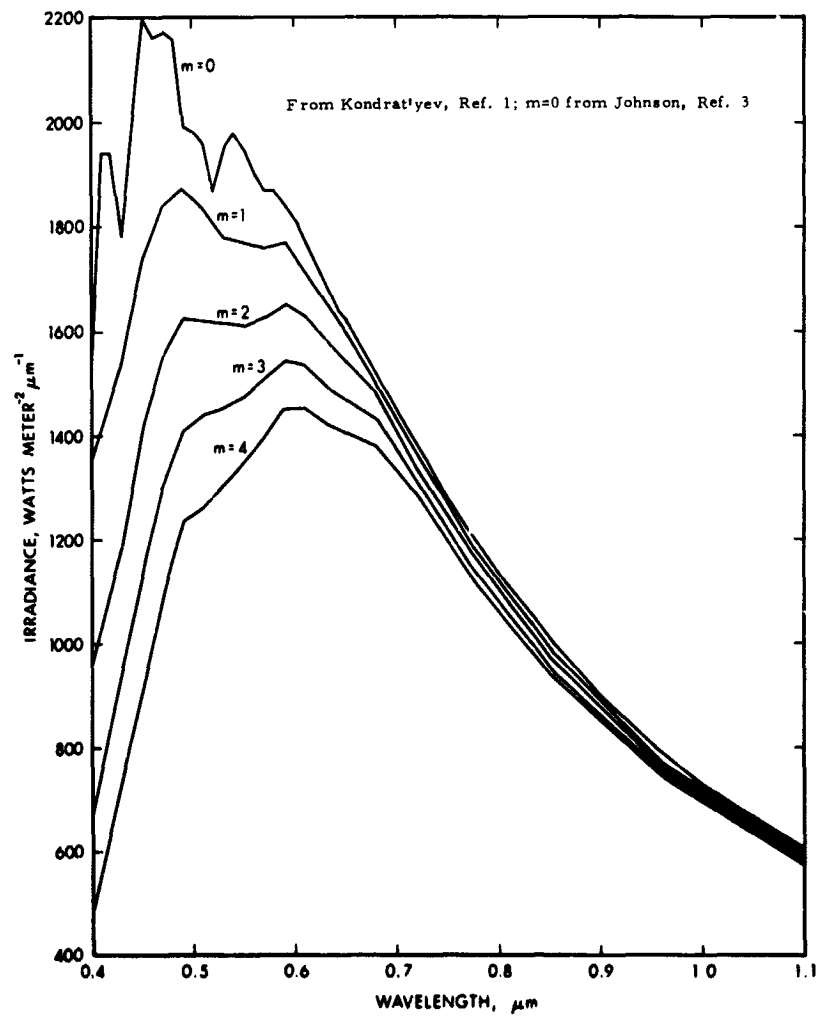


**Figure 4    Solar Irradiance at the Earth's Surface for Different Atmosphere (Rayleigh-Type) Optical Thicknesses.**

19
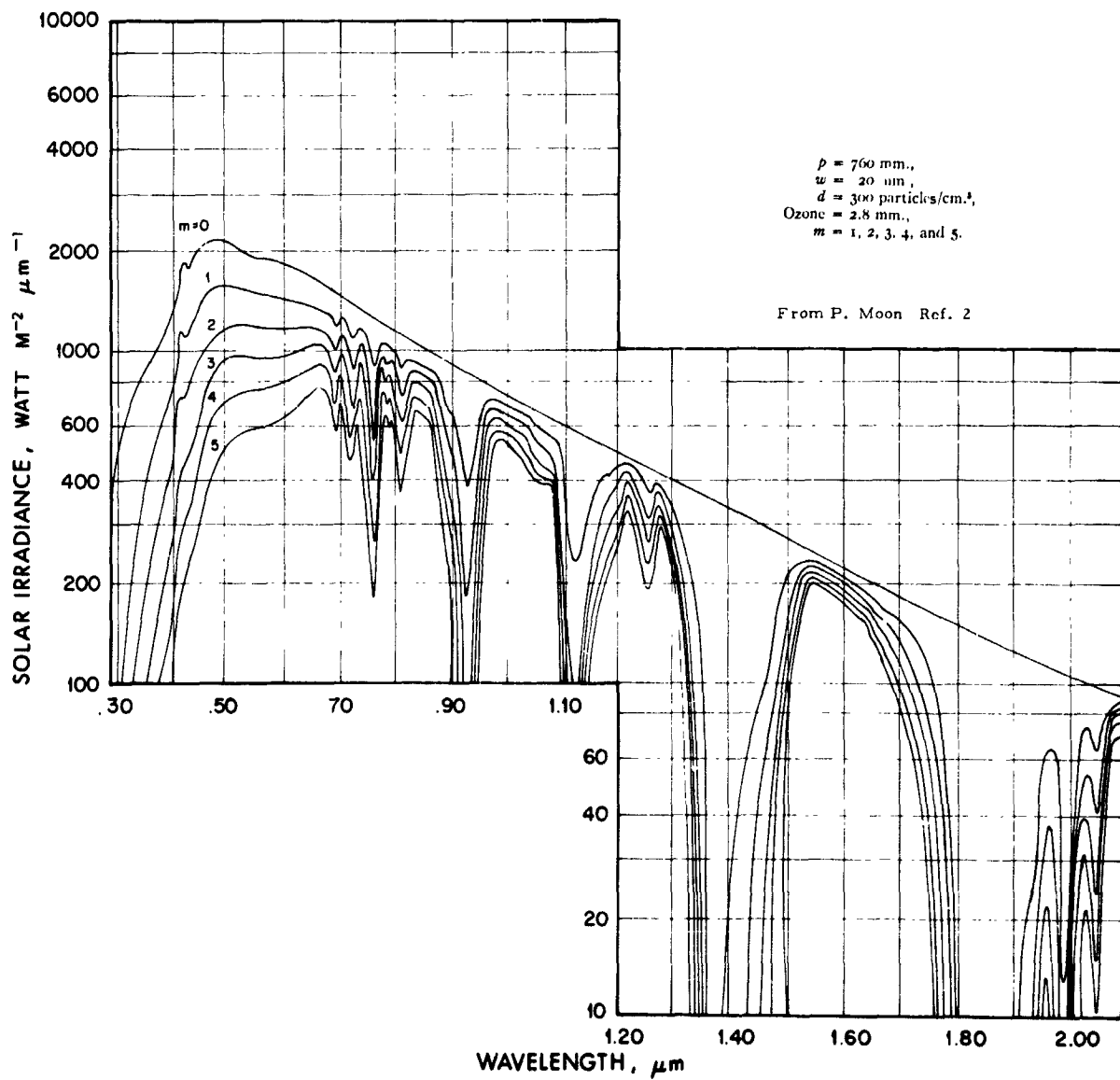
Figure 5    Solar Irradiance at Sea Level for Different
Air Masses for a Turbid Atmosphere.
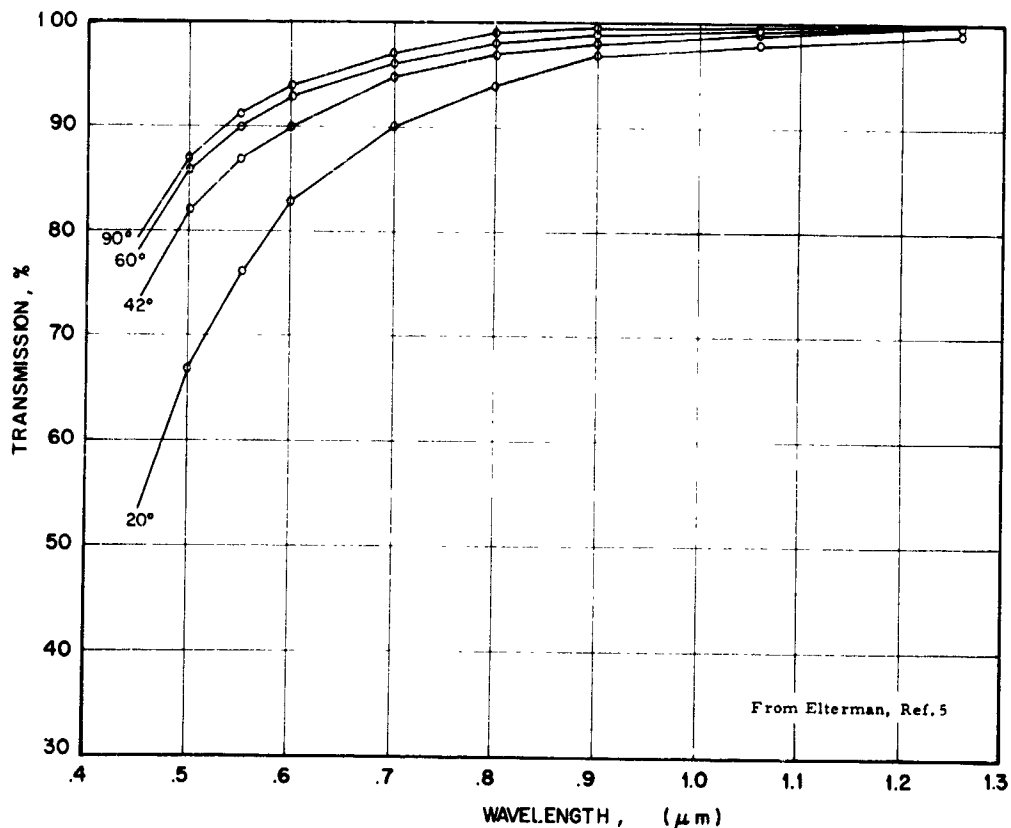
Figure 6a    Transmission for a Rayleigh Atmosphere at Solar
Elevation Angles of 90°, 60°, 42°, and 20°.
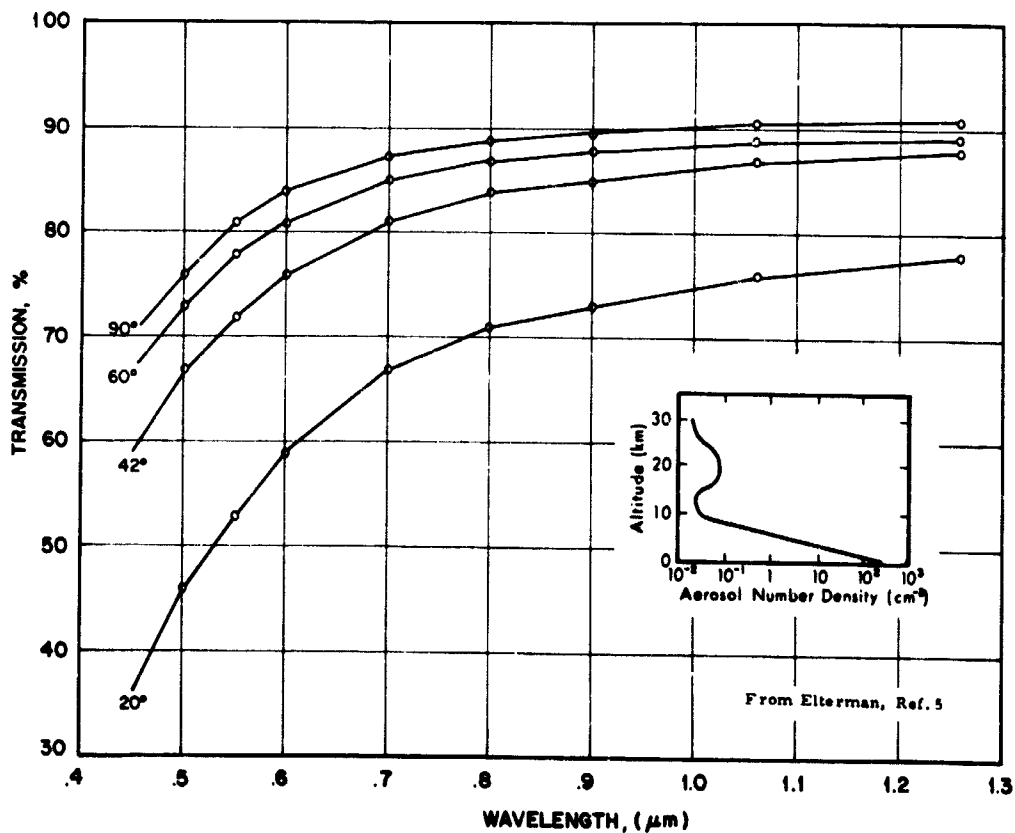


Figure 6b    Transmission for a Dry Turbid Atmosphere at Solar
Elevation Angles of 90°, 60°, 42°, and 20° with Aerosol
Distribution as Shown and 0.229 cm of Ozone.

21
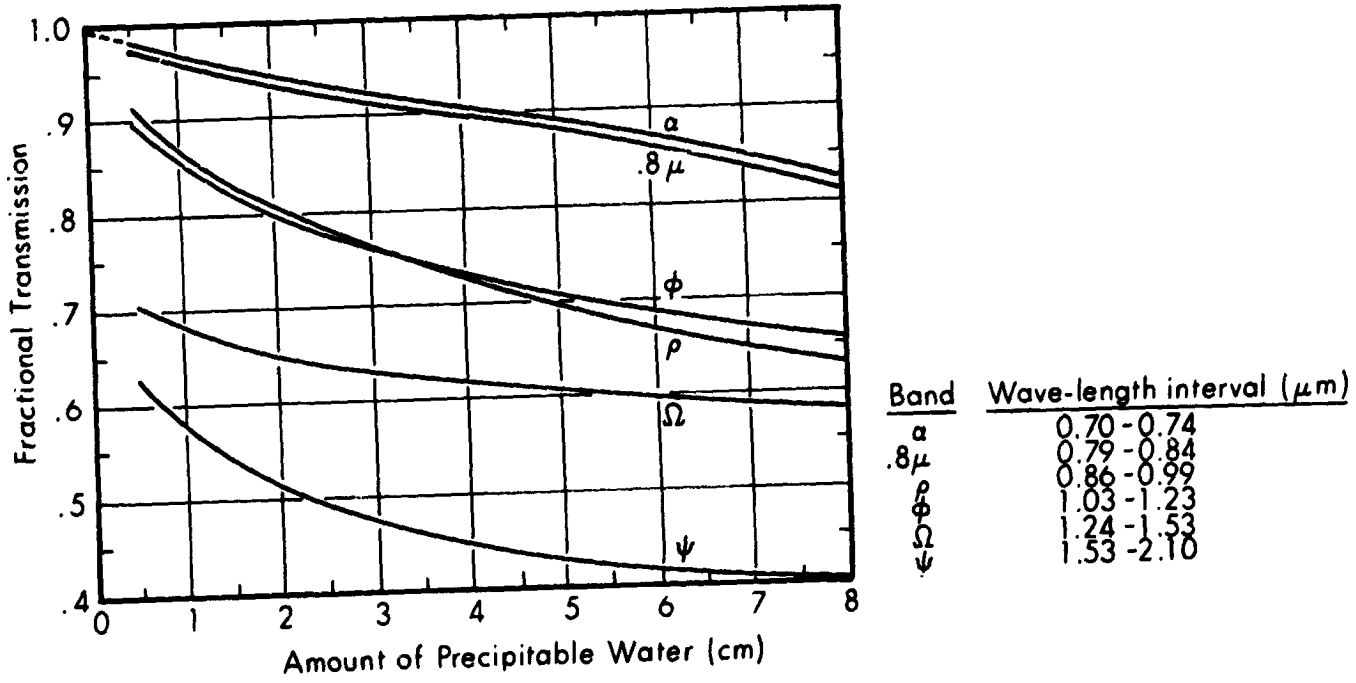
Figure 7    Transmission of Solar Radiation by Water Vapor.
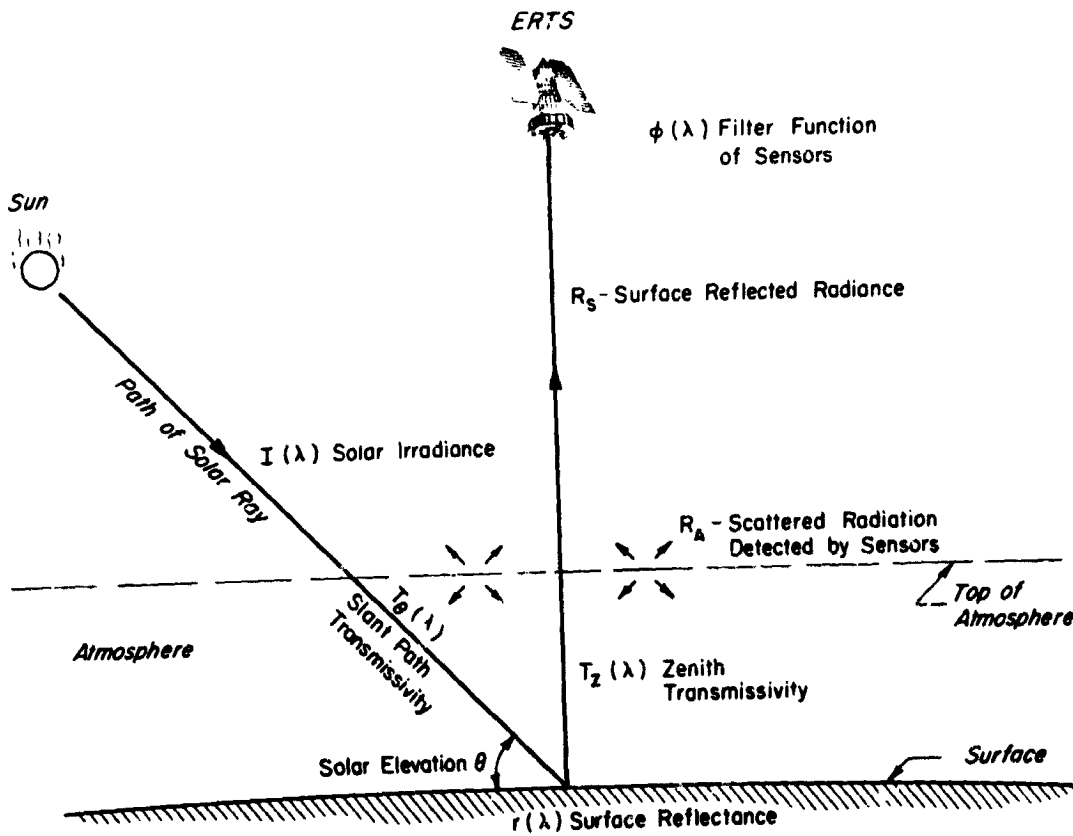


(Radiation reaching the sensors will not depart from the nadir more than $7^\circ$ at the corners of RBV pictures. )

Figure 8    Path of Solar Radiation Through the Atmosphere to the ERTS Sensor.
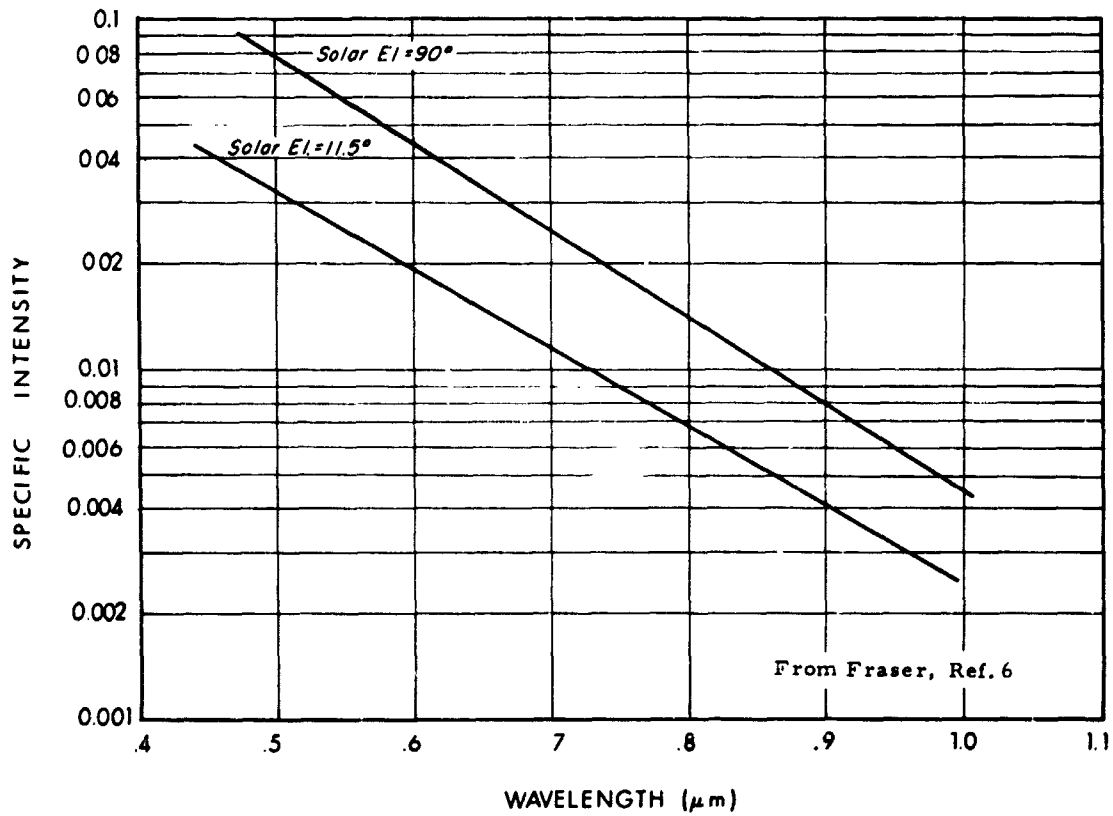
Figure 9    Specific Intensity of Scattered Radiation from
            Atmosphere Alone for Viewing the Nadir.
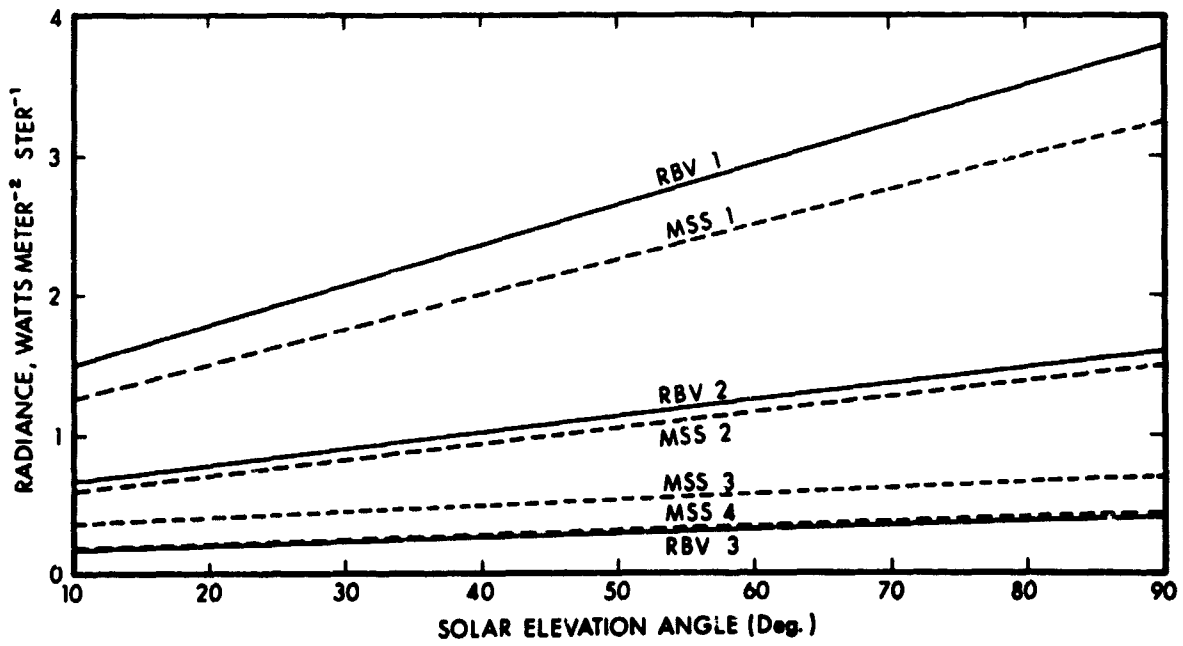


Figure 10   Radiance Available to RBV and MSS Channels
            from Atmosphere Alone ($R_A$).

23
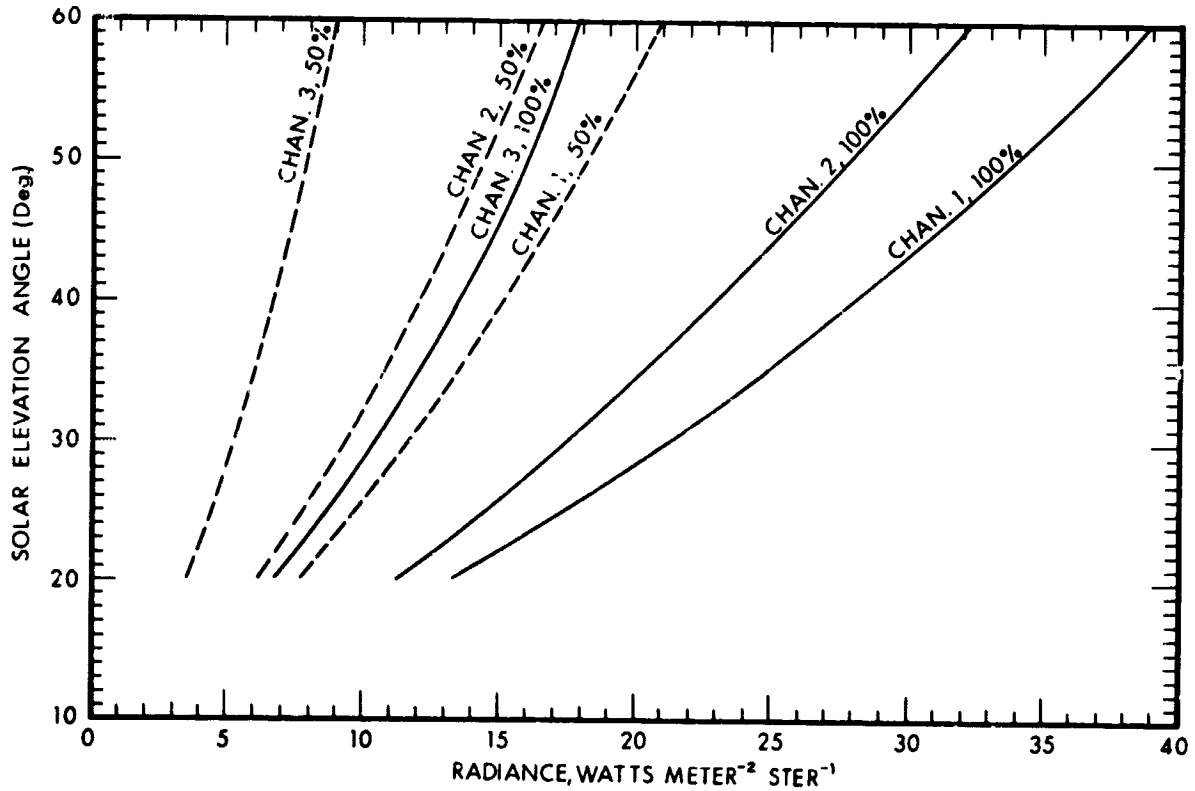
Figure 11    Radiance Sensed by RBV at Nadir from Surfaces of
50% and 100% Reflectance - Rayleigh Atmosphere
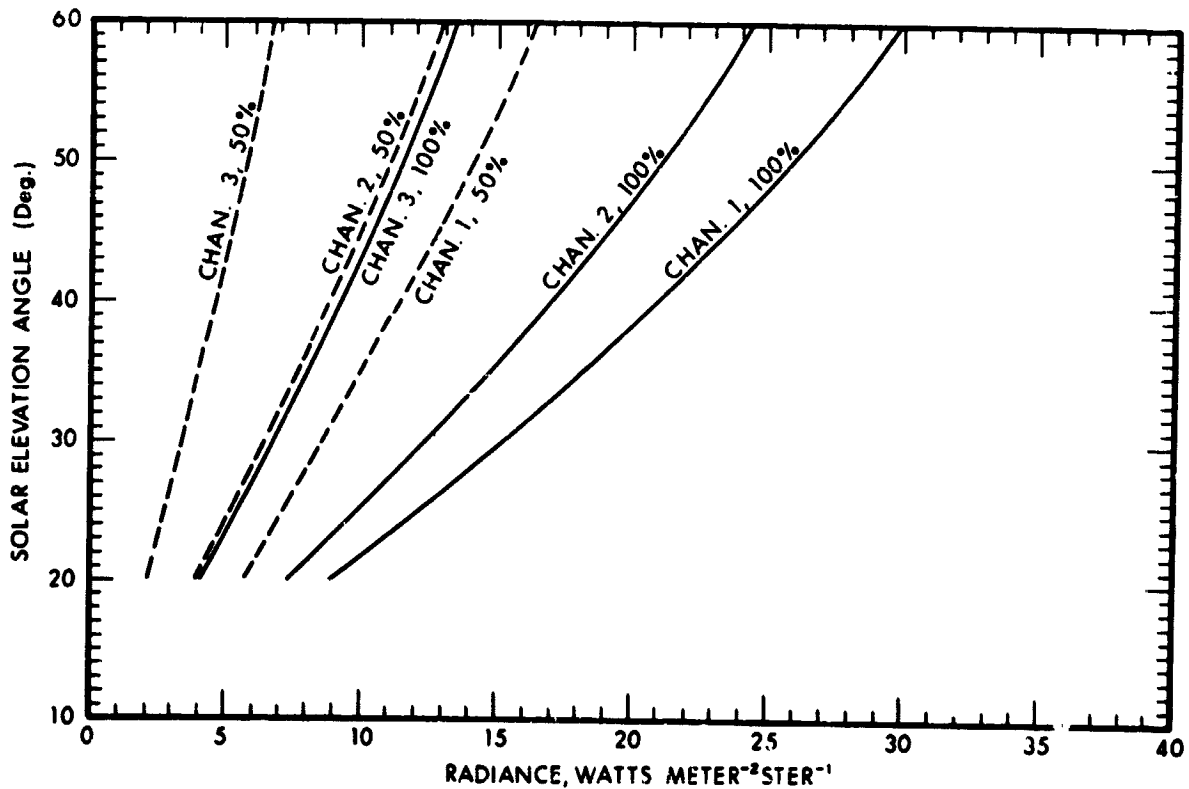


Figure 12    Radiance Sensed by RBV at Nadir from Surfaces of
50% and 100% Reflectance - Turbid Atmosphere
(2 g/cm$^2$ moisture)
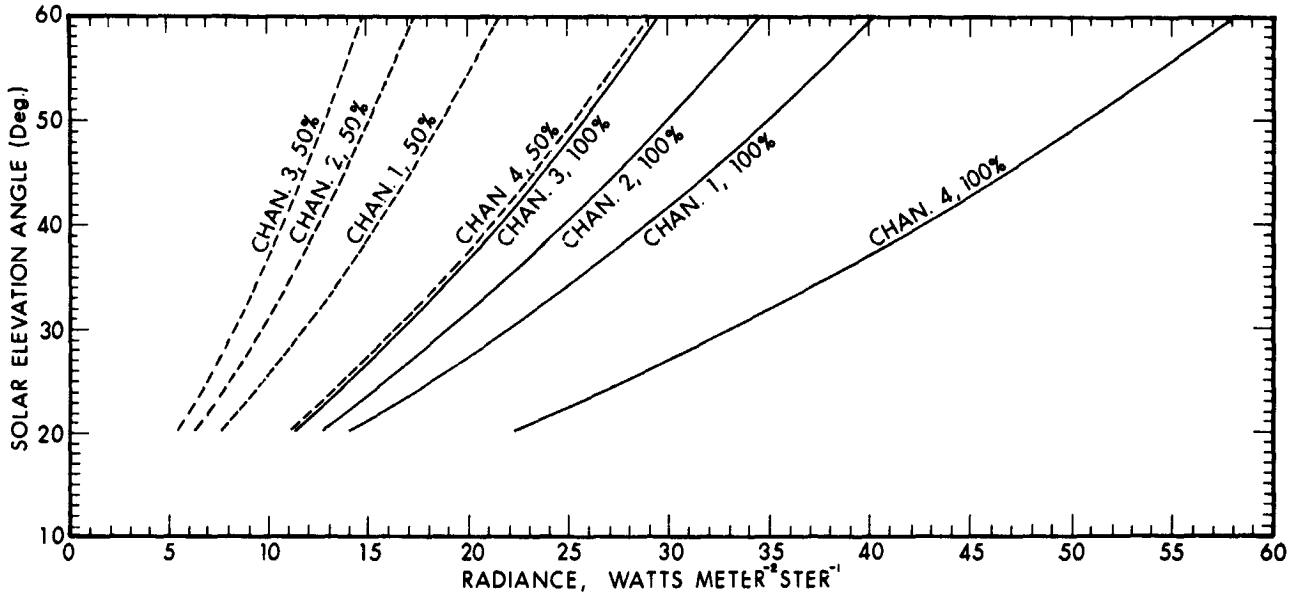
Figure 13    Radiance Sensed by MSS at Nadir from Surfaces of
50% and 100% Reflectance - Rayleigh Atmosphere
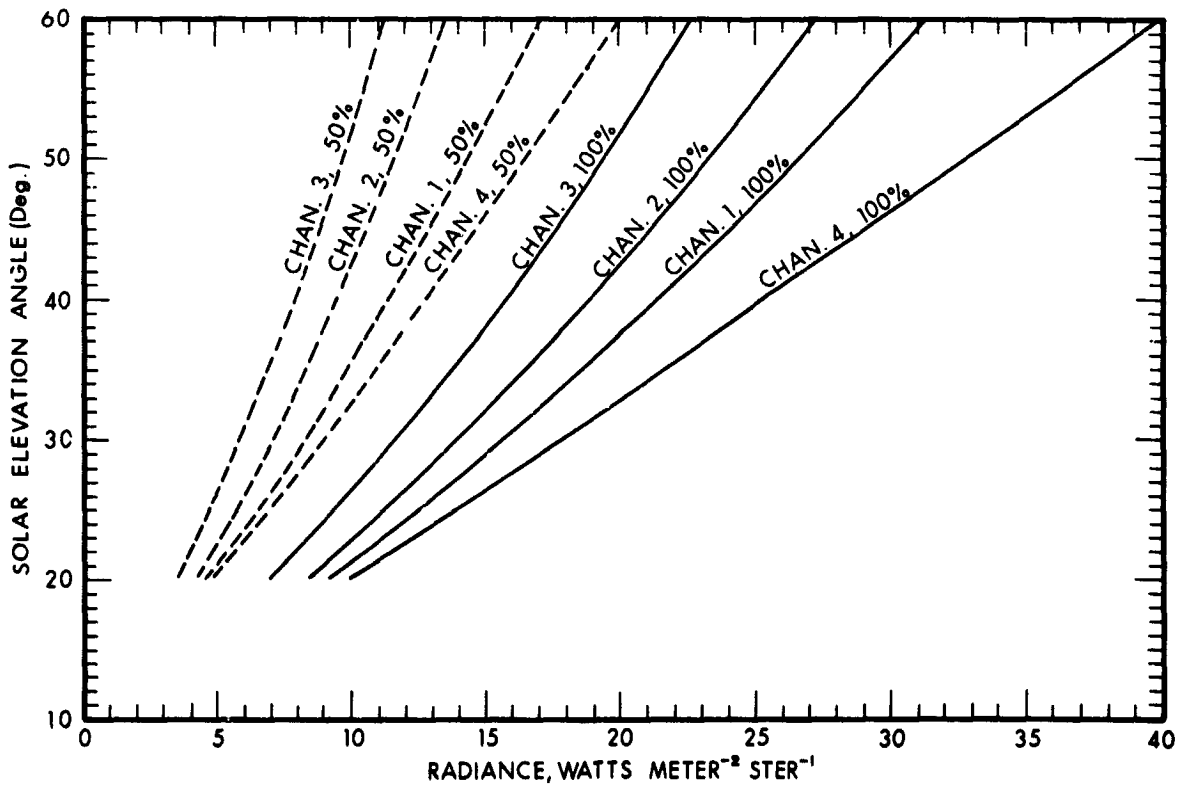


Figure 14    Radiance Sensed by MSS at Nadir from Surfaces of
50% and 100% Reflectance - Turbid Atmosphere
(2 g/cm$^2$ moisture)
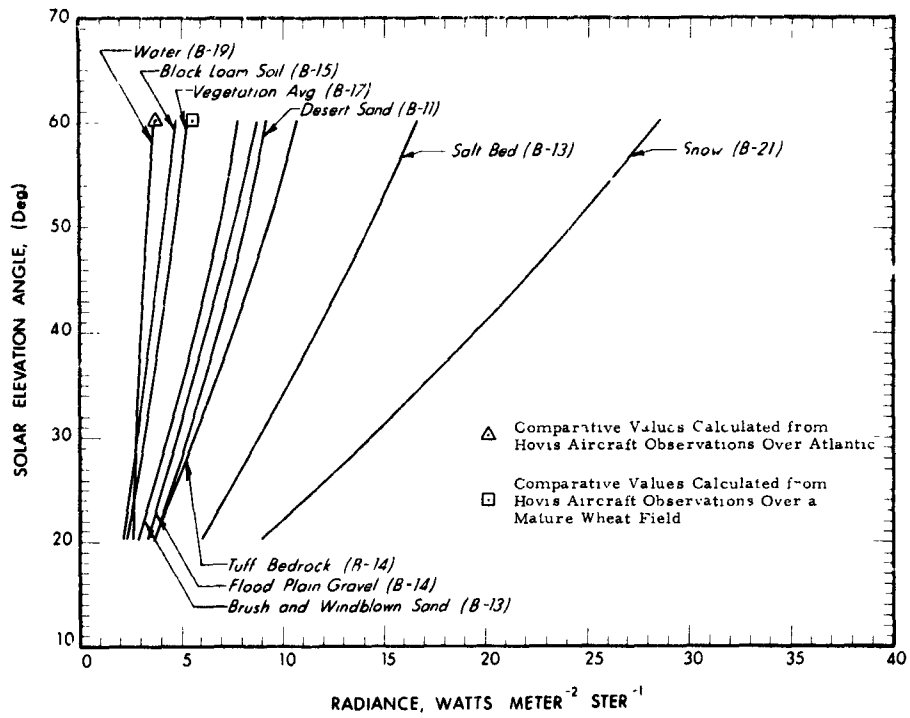
Figure 15   RBV No. 1: Radiances for Typical Natural Surfaces -
Turbid Atmosphere (2 g/cm$^2$ moisture)
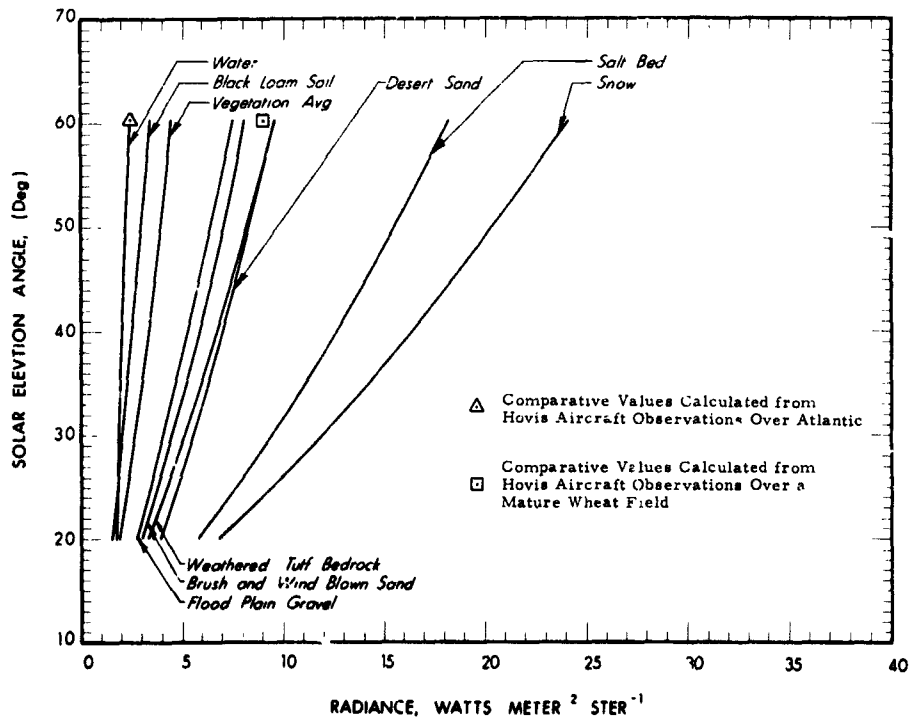


Figure 16   RBV No. 2: Radiances for Typical Natural Surfaces -
Turbid Atmosphere (2 g/cm$^2$ moisture)

26
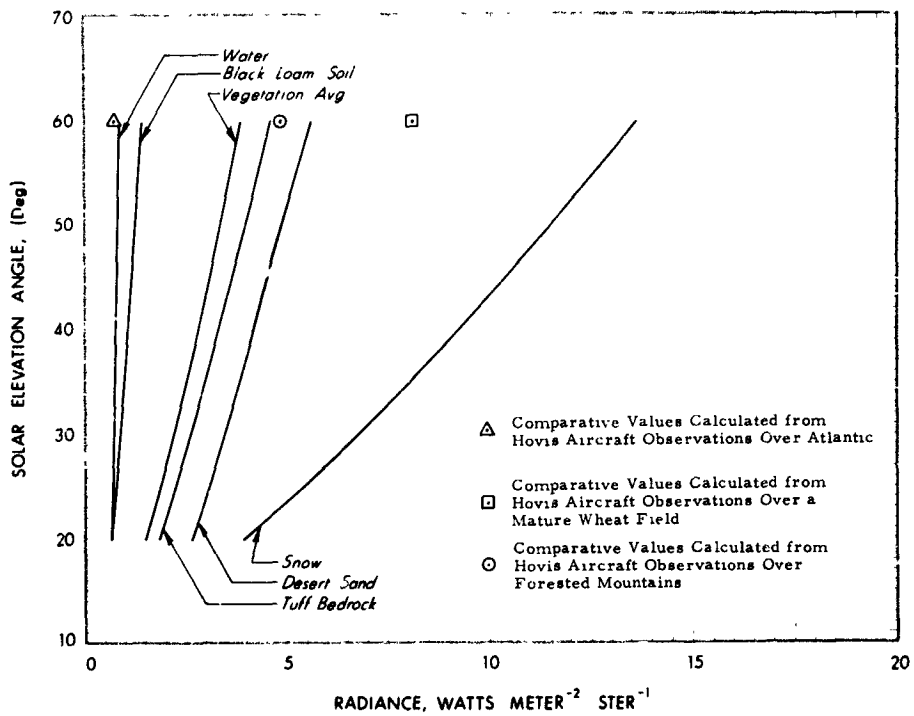
Figure 17    RBV No. 3: Radiances for Typical Natural Surfaces -
Turbid Atmosphere (2 g/cm$^2$ moisture)
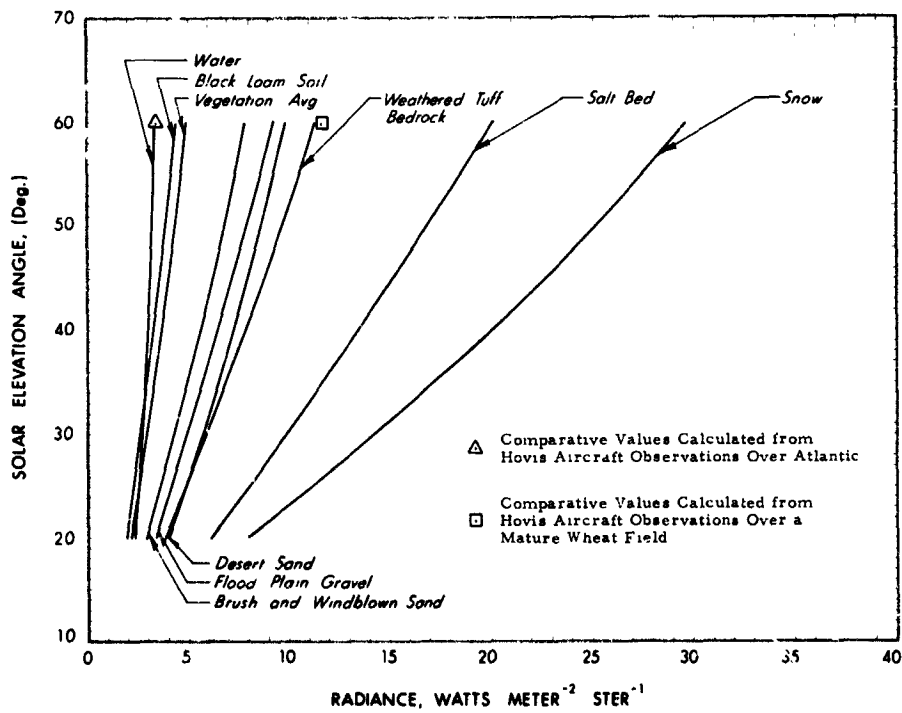


Figure 18    MSS No. 1: Radiances for Typical Natural Surfaces -
Turbid Atmosphere (2 g/cm$^2$ moisture)

27
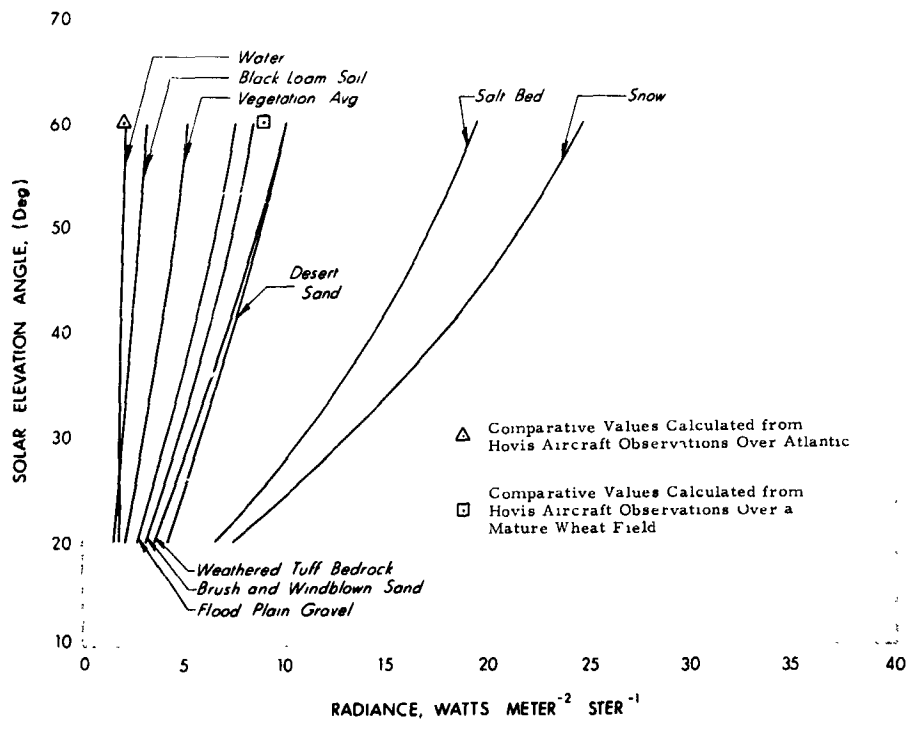
Figure 19    MSS No. 2: Radiances for Typical Natural Surfaces -
Turbid Atmosphere (2 g/cm$^2$ moisture)
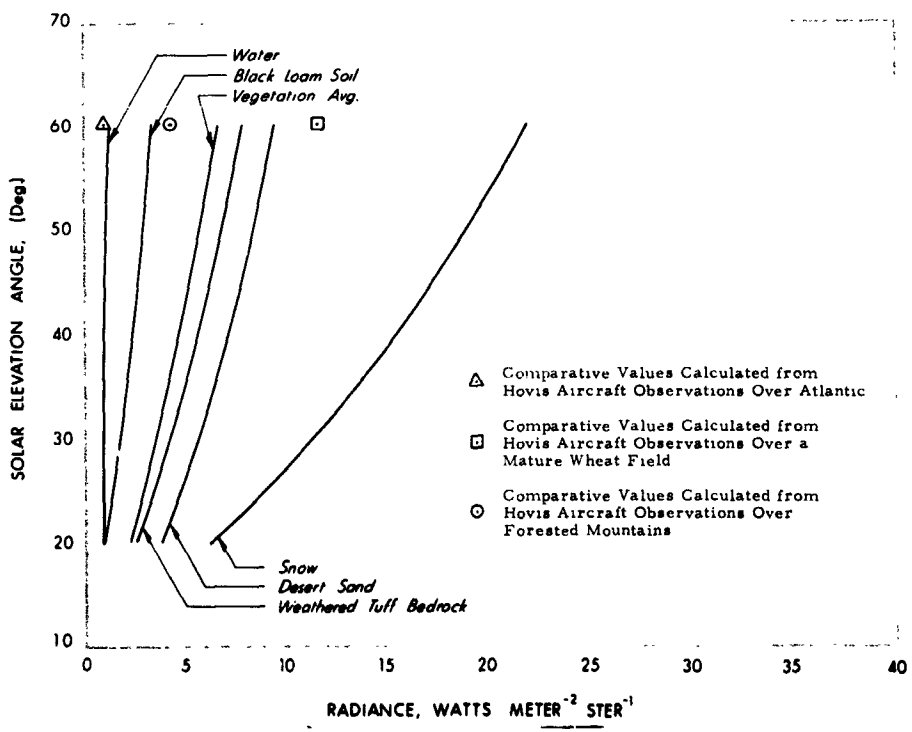


Figure 20    MSS No. 3: Radiances for Typical Natural Surfaces -
Turbid Atmosphere (2 g/cm$^2$ moisture)

28
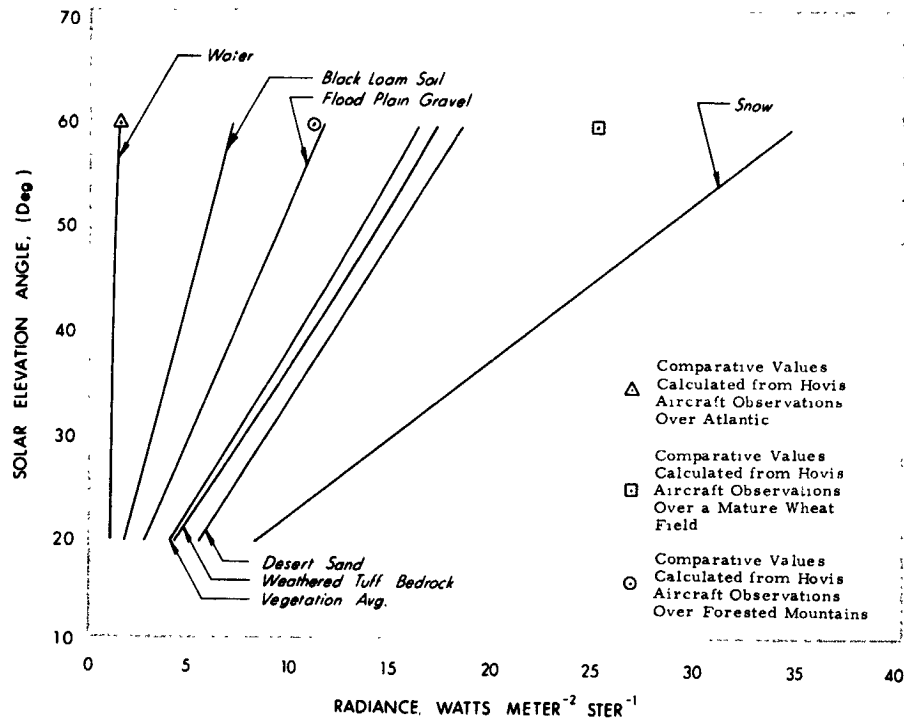
Figure 21    MSS No. 4: Radiances for Typical Natural Surfaces -
Turbid Atmosphere (2 g/cm² moisture)
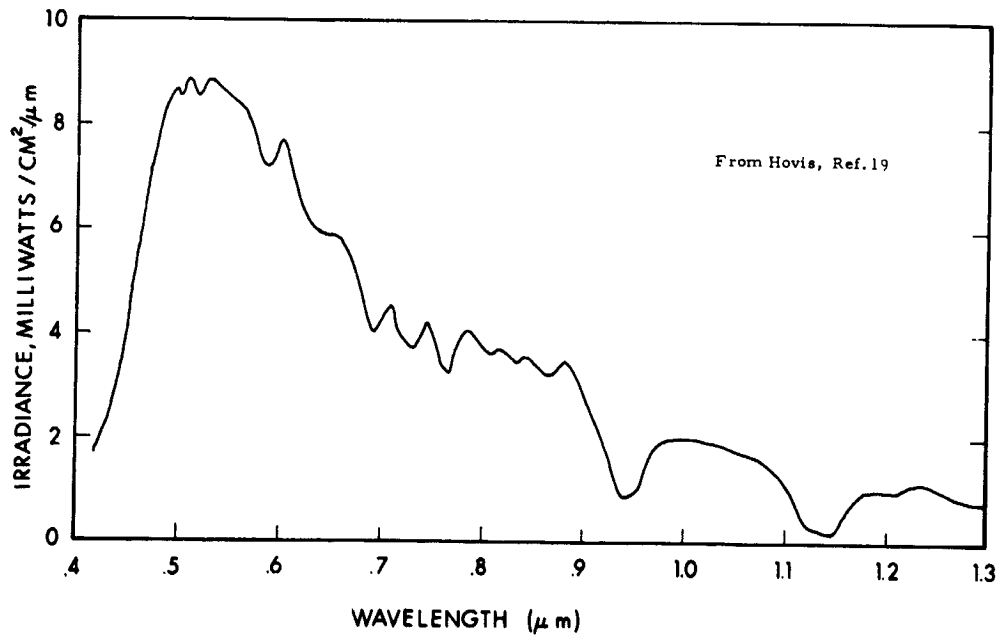


Figure 22    Aircraft Spectrometer Measurement of Solar
Reflected Radiation over Gulf Stream at 1000 meters
(Solar Elevation Angle ~ 60°)
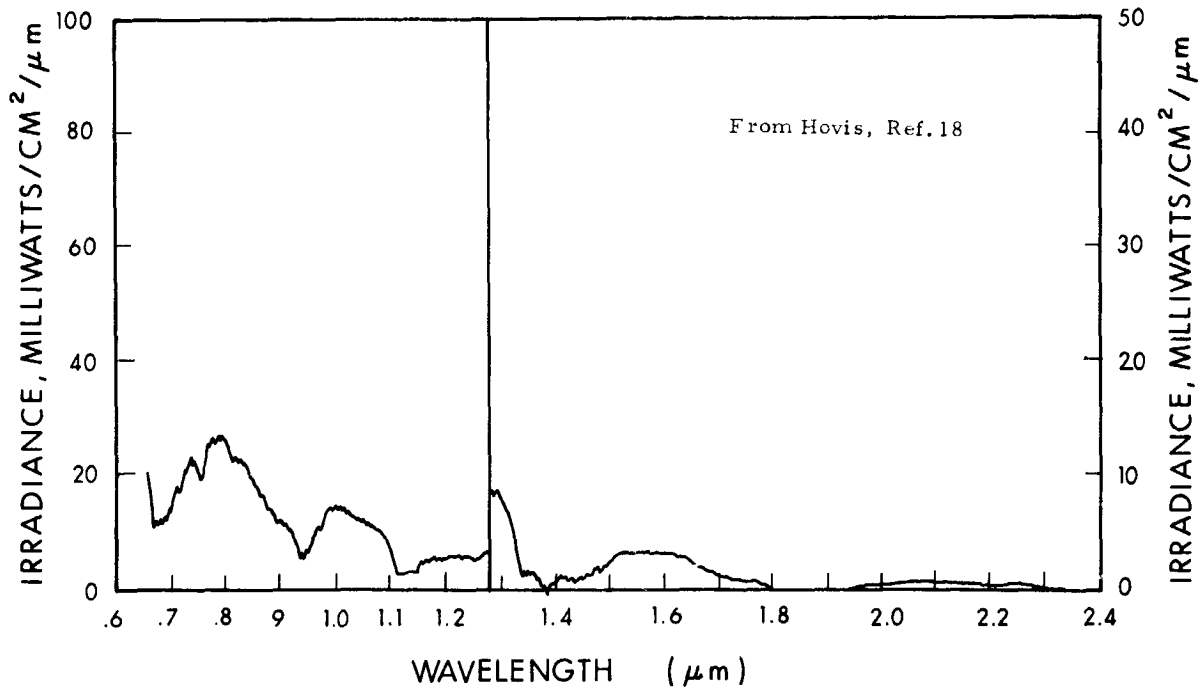
Figure 23    Aircraft Spectrometer Measurement of Solar
Reflected Radiation over Heavy Forested Area,
Big Sur, California, from ∼2-1/2 km (Solar
Elevation is 60°, May 23, 1968)
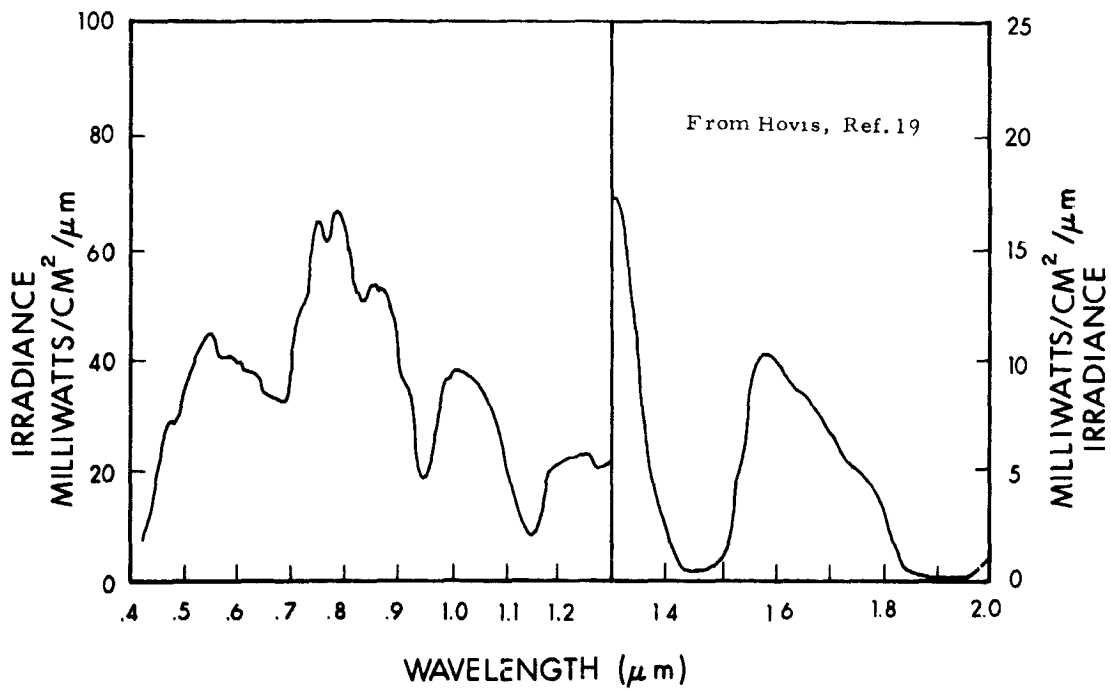


Figure 24    Aircraft Spectrometer Measurement of Solar
Reflected Radiation Over a Mature Wheat Field,
Kansas, from ∼2-1/2 km (Solar Elevation ∼60°,
July)

30

## 4. SENSOR MONITORING TECHNIQUES AND PROCEDURES

In this section, two techniques for the monitoring of sensor degradation by means of ground-truth data are separately discussed. The first employs aircraft measurements and the second is dependent on radiance values computed by means of modeling techniques. Based on an evaluation of these techniques, a procedure for the operational monitoring of sensor degradation by the ERTS Data Center is specified and recommended. The techniques and procedures discussed include specifications of prelaunch and postlaunch measurements of surface, subsurface and atmospheric parameters at the ground-truth sites.

### 4.1 Aircraft Technique

The basic problem faced in monitoring the responses of satelliteborne sensors is that the postlaunch calibrations of such sensors cannot be checked in a controlled laboratory environment. As mentioned earlier, these will be made on board the system for monitoring system response. This monitoring system is itself subject to change over a period of time. The calibrations of comparable aircraft sensors, however, can be checked repeatedly in laboratories. This makes it possible to monitor sensors on board orbiting satellites by comparing their measurements with those made concurrently over the same ground-truth site by identically calibrated aircraftborne sensors.

Temporal changes in the radiometric character of a given test site due to physical changes in surface or subsurface properties can therefore be accurately monitored by the calibrated aircraftborne sensors. Large departures in satellite measurements in excess of those reasonably expected from aircraft data can then be attributable to spacecraft sensor calibration degradation or sensor malfunction.

In actual operation, it is envisioned that the adverse effects resulting from differences in spatial resolution between the aircraft and satellite measurements can be minimized by careful selection of the ground-truth sites. It is highly desirable, for example, that the test sites have uniform surface characteristics over large horizontal extents. This will make it possible to obtain a large number of aircraft data points over the given site such that representative means can be computed and compared with the concurrent satellite measurements made at a coarser resolution. The effects of the difference in optical thickness between the aircraft and satellite measurements can be accounted for by applying

31

to the aircraft data, the type of correction factors computed from model atmospheres as discussed in Section 3. 5.

With this approach to the monitoring of sensor calibration, the requirements for postlaunch on-site measurements, other than the aircraft radiometric measurements, are minimal. While it would be of scientific interest to note changes in the physical properties of the surface and subsurface materials, and their effects on reflectance, the only observation really essential is the cloud field over the entire test site at the time of the aircraft measurements and satellite passage. These cloud observations will determine the extent to which the aircraft data are useful. Because of the desirability of having uniform surface characteristics over large horizontal extents at ground-truth sites, prelaunch on-site measurement requirements are quite substantial. These requirements are discussed in detail in Section 4. 3.

## 4. 2 Modeling Techniques

The comparison between actual aircraft spectrometric measurements and the calculated radiances presented in Section 3. 7 suggests that the modeling technique discussed in Section 3 can be used to provide a good approximation of the expected radiances measured by the ERTS sensors over surfaces of known reflective properties. Sites can be selected such that the temporal variations in surface and subsurface properties are small (see Section 4. 3. 2). For each of these sites, sets of expected radiance curves can then be computed (similar to those presented in Section 3. 5). Large departures between satellite-measured values over the sites and those predicted by the model calculations can be taken to be indicators of calibration degradation.

As is the case in the aircraft technique, the main emphasis in on-site data-gathering is in the prelaunch phase of operations. However, it would be desirable to frequently monitor some surface and subsurface properties, such as moisture content, which are known to undergo short-term fluctuations. The monitoring of these properties will provide information from which changes in surface reflectivity can be deduced.

## 4.3 Test Site Selection and Ground Data Collection

### 4.3.1 Test Site Characteristics

It is evident from Sections 4.1 and 4.2 that selection of appropriate test sites is of the utmost importance to both of the suggested calibration monitoring techniques.

The more data for a particular target test site, the easier it will be to monitor the calibration of the satellite sensors. The calibration of the RBV and MSS sensors will be facilitated using ground test sites with the following characteristics:

1.  Calibration sites should be dispersed over the United States so as to provide opportunity for readings during as many passes as possible.

2.  Spectral characteristics of each test site surface must lie in the response range of the three RBV and four MSS channels.

3.  A large, stable water body should be located nearby to serve as a low-response check on calibration.

4.  The site area should be large enough to be seen with the unaided eye on the final prints.

5.  The local vertical relief within the test site should not vary more than 100 ft. If the maximum relief exceeds 100 ft, these variations should be located and their effects identified.

6.  The surface of the site should be of uniform lithologic composition. If variations are present, their locations must be known.

7.  Because dry sand lies at the upper limits of the linear RBV response, the surficial cover of the site should contain large areas of sand-sized particles of uniform texture and shape.

8.  The site should be generally devoid of a dense vegetal cover. Sparse vegetation of known distribution may be acceptable.

9.  Presence of perennial streams and lakes, etc., will be detrimental to the calibration study. Sparse intermittent streams and playas of known location are acceptable.

33

### 4.3.2 Potential Ground-Truth Sites

Based on the above requirements, three major ground-truth sites and 35 minor sites were selected for use in the study. Each of the sites has similar characteristics, i. e., fairly large area covered primarily with sand. Most of the sites are located close to a fairly large water body so that interfacing with the sand-covered area will be provided. In most cases, the minor site listing also identifies the USGS topographic map which contains the suggested site.

#### Major Sites

The three major sites are all located in the Basin and Range province of the United States' southwest (Figure 25 presents a locator map). This area contains five geomorphic sections. Our test sites include:

1. The Smoke Creek and Black Rock Deserts
2. The Great Salt Lake Desert
3. The Sonoran Desert

A complete description of these areas is contained in Appendix A.

#### Minor Sites

In addition to the three large calibration sites suggested in this report, the following is a list of minor target areas. The surface cover of these sites is covered by sandy materials; no detailed investigation, however, was conducted for any of these localities. The sites are not listed in a preferential order.

1. Cape Cod Coastal Dunes, Massachusetts
   (USGS Map NK-19)

2. Assateague Island, Maryland and Virginia
   (USGS Map NJ-18)

3. The Outer Banks of Pamlico Sound, North Carolina
   (USGS Map NI-18)

4. Cape Kennedy, Florida
   (USGS Map NH-17)

5. Cumberland Island, Florida
   (USGS Map NH-17)

6. St George Island, Florida
   (USGS Map NH-16)

Figure 25    Locator Map of Major Test Sites
            (Courtesy of Jeppesen and Company, Denver)

7. Sanibel Island, Florida
   (USGS Map NG-17)

8. Galveston Island, Texas
   (USGS Map NH-15)

9. Corpus Christi Bay Sand Bars along the Laguna Madre, Texas
   (USGS Quadrangle Map - Corpus Christi)

10. Matagorda Island, Texas
    (USGS Map NH-14)

11. Black Mesa, Southeast of Raton, New Mexico
    (USGS Map NJ-13)

12. Sand Dunes along the Topeka, Santa Fe and Panhandle Railroad, New
    Mexico
    (USGS Map NI-13)

13. White Sands National Monument, New Mexico
    (USGS Map NI-13)

14. Sand Dunes and Hills, Arkansas River, Kansas
    (USGS Map NJ-14)

15. Little Colorado Desert and Area 40 Miles Southeast of it, Colorado
    (USGS Map NK-12)

16. Sand Hills, Nebraska
    (USGS Map NK-14)

17. Sand Hills Along the South Platte River, Colorado, Nebraska
    (USGS Map NK-13)

18. Sand Hills South of South Platte River, Colorado
    (USGS Map NK-13)

19. Sand Hills Northeast of North Platte River, Nebraska
    (USGS Map NK-13)

20. Sand Hills West of Seminoe Reservoir, Wyoming
    (USGS Map NK-13)

21. Sevier Lake Playa, Utah
    (USGS Map NJ-12)

22. Railroad Valley and Playa, Nevada
    (USGS Map NJ-11)

23. Desert Valley, Nevada
    (USGS Map NK-11)

24. Yuma Desert South of Yuma, Arizona
    (USGS Quadrangle Map - El Centro)

25. Painted Desert, Arizona
    (USGS Map NI-12)

26. Tule Desert, Arizona
    (USGS Map NI-12)

27. Imperial Valley Sand Dunes, California
    (USGS Map NI-11)

28. Dunes of Death Valley Near Stove Pipe Wells, California
    (USGS Quadrangle Map - Death Valley)

29. Coastal Dunes of California
    (USGS Maps NK-10, NJ-10 and NI-10)

30. Owens Lake Playa, California
    (USGS Map NJ-11)

31. Coastal Sand Dunes North of Ten Mile Creek, Reedsport, Oregon
    (Ref. 23, pp 148-149).

32. Sand Hills in the Christmas Lake Valley, Oregon
    (USGS Map NK-13)

33. Sand Dunes East of Summer Lake, Oregon
    (USGS Map NK-10)

34. Alvord Desert, Oregon
    (USGS Map NK-11)

35. Sand Dunes and Hills, Moses Lake, Washington
    (USGS Map NL-11)

4.3.3 On-Site Measurements

At the ground-truth sites, on-site measurements of the physical properties
of the surface, subsurface materials and of the atmosphere are required during

both the prelaunch site survey and definition phase and the subsequent postlaunch sensor monitoring phase. Measurements made during the site survey and definition phase will be used primarily to provide data from which expected radiances, and their variability (such as seasonal trends), can be computed. As discussed in Appendix C, and Sections 3 and 4, the data required are quite numerous. The following provides a summary list of some of the more importa + physical parameters needed to properly define the range of expected reflectance values of the surficial materials at a ground-truth site.

1. Measurement of the moisture content of the surface layer (0-0.5 cm).

2. Measurement of the mineralogical composition of the sampled locality.

3. Measurement of the texture of the surface cover.

4. Measurement of the color of the weathered surface.

5. The processes of erosion and deposition of the sampled locality should be noted, including also its topographic position in relation to the overall calibration site.

6. Delineation of the presence, or absence, of density and type of vegetal cover.

7. Spectrometric measurement of the surface reflectance and/or temperature for various solar positions.

8. Reflectance measurements of plants or group of plants.

9. Reflectance measurement of exposed soil surfaces beneath the plants to determine their effect on the readings.

In conjunction with these surface measurements, it would be necessary to obtain aircraft measurements of the reflectance at a number of different spatial resolutions so that the influence of surface nonuniformities on low spatial resolution measurements of reflectance can be determined.

In addition to these measurements to determine the in situ values of surface reflectance, a study of the properties of the clean atmosphere above each of the sites needs to be conducted. Such a study will require systematic measurements of the optical transparency of the atmosphere by means of instruments such as actinometers so that the seasonal, and possibly synoptic scale, variability in the spectral transmissivities of the atmosphere can be determined.

38

Subsequent to launch, the monitoring of the time-varying surface parameters, such as the moisture content and changes in vegetal cover, would be highly desirable. As indicated in Appendix C and Section 3, the reflectance of surfaces, especially of sandy surfaces suggested here, is highly dependent on surface and subsurface moisture. The monitoring of surface moisture during postlaunch operations is therefore extremely important at each of the ground-truth sites. Any substantial increase in soil moisture content deviating from the average would indicate that the reflectance values established for the site during the site definition phase need to be revised. If revision of such values is not possible, it would be necessary to terminate the use of the site for ground-truth measurements until such time as the on-site data indicate a return of the surface and subsurface properties to their initial values.

It is presently envisioned that the postlaunch monitoring of the on-site characteristics can be accomplished, in part, by means of unmanned instrument platforms. The data would be transmitted to a central location, such as the ERTS Data Center, by means of the ERTS satellite itself. In this way, personnel responsible for monitoring the on board calibration of the ERTS sensors can have ready and immediate access to the on-site data.

4. 4  Suggested Sensor Calibration Monitoring Procedure

Deficiencies in the use of ground-truth data for the monitoring of sensor calibration can be minimized by the use of a large number of calibration checkpoints; i.e., ground-truth sites. However, as the number of sites increase, the cost of operating the aircraft overflight scheme, as discussed in Section 4.1, would increase beyond justification if the overflights were to be conducted at each ground-truth site. Therefore, while ground-truth measurements from aircraft provide the most reliable means of checking the calibrations of the on board sensors, the cost and logistics of aircraft operations realistically restrict such measurements to a few times a year over a limited number of the selected sites. In between such aircraft measurements, use must be made of the modeling technique discussed in Section 4.2. This being the case, great importance is attached to the initial site definition measurements and the subsequent monitoring of changes in the on-site physical characteristics. The constant update of these on-site data and the application of these data to sensor calibration monitoring, we see as the proper function of the ERTS Data Center. In the following paragraphs, the operational procedures at the Data Center, as they relate to the sensor calibration problem, are discussed in detail.

39

### 4. 4. 1 Film Calibration Measurements

Measurements by the ERTS sensors over ground-truth sites will be utilized in conjunction with ground-truth data, as available, as an overall time sequence review of sensor integrity. The ERTS radiance measurements could be performed on either the film or on the digital data. We suggest that measurements of the film output be routinely made whenever data from a pass over a ground-truth site are available.

A calibration step wedge should be produced simultaneously with the pictures by the Ground Station. It will be sufficient to produce one gray-scale per RBV and MSS channel for each interrogation, although it is desirable that each frame have its own gray-scale. It is foreseen that at least the MSS will have inflight calibration checks with a lamp of known luminosity and the sun. These inflight measurements for which the radiances are known will be recorded by the Ground Station as density steps on film. At least three step wedges are required, more are desirable if the density to radiance relationship is not linear.

The ERTS Data Center (ERDC) should have available prior to launch a calibration table with the radiance values for each calibration density step on the film. The ERDC scientists should work prior to launch with the RBV and MSS experimenters to assign initial absolute film density values to each calibration density step for which radiances are known. These standard density values should be revised after launch as needed to obtain a better photographic product and/or to correct for inflight calibration shifts.

The calibration check by the ERDC verifies that film density to radiance relationship is being kept within acceptable limits by the Ground Station and the Photographic Lab. Densitometric measurements will be made with a Macbeth-type densitometer on the gray step wedges and compared with the standard. The ERDC will quickly inform the Ground Station and the Photographic Lab. of any discrepancy and will try to determine whether it is due to:

1. Ground Station equipment
2. Film-processing equipment
3. Sensor deterioration
4. Calibration lamp deterioration

Sensor deterioration will show up as a general lowering of picture contrast and also as lower radiance values in the digital outputs. Calibration lamp deterioration also will show up as deterioration of the digitized gray-scales only.

40

Ground Station equipment problems can be quickly differentiated from photographic film-processing problems by passing a film strip of known exposures through the photographic cycle.

The ERDC will measure densities of specific test sites by means of a Macbeth-type densitometer, calculate the equivalent radiance values, and record these values. These measured radiances should be compared with ground-truth measurements from aircraft, if available, and with calculations such as presented in Section 3. Of course, ground-truth values should be corrected for atmospheric effects before comparison to satellite measurements. Large discrepancies will be investigated and possible causes will be determined and documented in timely reports.

As a by-product of these calibration checks, a comparison of ground-truth radiance measurements and satellite measurements may yield the transmissivity of the atmosphere above the test sites.

### 4.4.2 Digital Data Calibration Check

Digital data calibration checks should occur periodically but at less frequent intervals than the checks on the film. It is foreseen that the printout will be digital maps in units of radiances and will be available at the scale required to show each resolution element. The ERDC will have ready for each of the selected calibration sites a transparent overlay at the same scale of the expected printout showing the latitude-longitude lines, the location of the test sites and other major features. The overlay can be prepared before launch. If the need arises, the overlay can be corrected for scale photographically.

After locating the test site, radiances will be averaged disregarding values near the boundaries. This average radiance will be recorded and compared with the radiance values obtained from the film, aircraft measurements, and model calculations such as presented in Section 3. Large discrepancies will be investigated and possible causes will be determined and documented in timely reports. Digital data calibration checks should also be made on the film gray-scale as an approximate review on the digitizing routines.

The measurement checks, whether made on film or on digital data, should be presented as a display of reflectance for each spectral band, as a function of time and site location as shown in Figures 26a and 26b. The ground-truth measurements should be presented on the same display. No atmospheric corrections should be applied but the source of each data point should be clearly identified.

41

RBV

B₁  R

B₂  R

B₃  R

⬡ = Black Rock Desert/Smoke Creek      ◯ = Great Salt Desert
△ = Sonoran Desert                     ◇ = Misc. Site

} Envelope

T₀    18 Days    T₁    18 Days    T₂    18 Days    T₃

a.)    RBV Band

MSS

B₁  R

B₂  R

B₃  R

B₄  R

T₁    18 Days    T₂    18 Days    T₃    18 Days    T₄
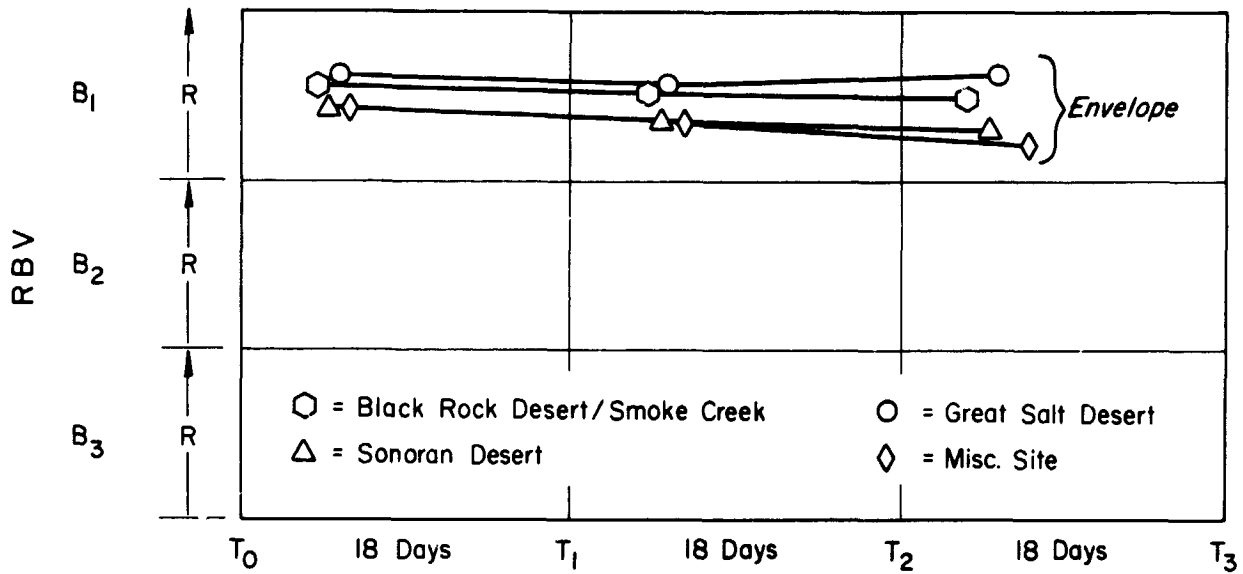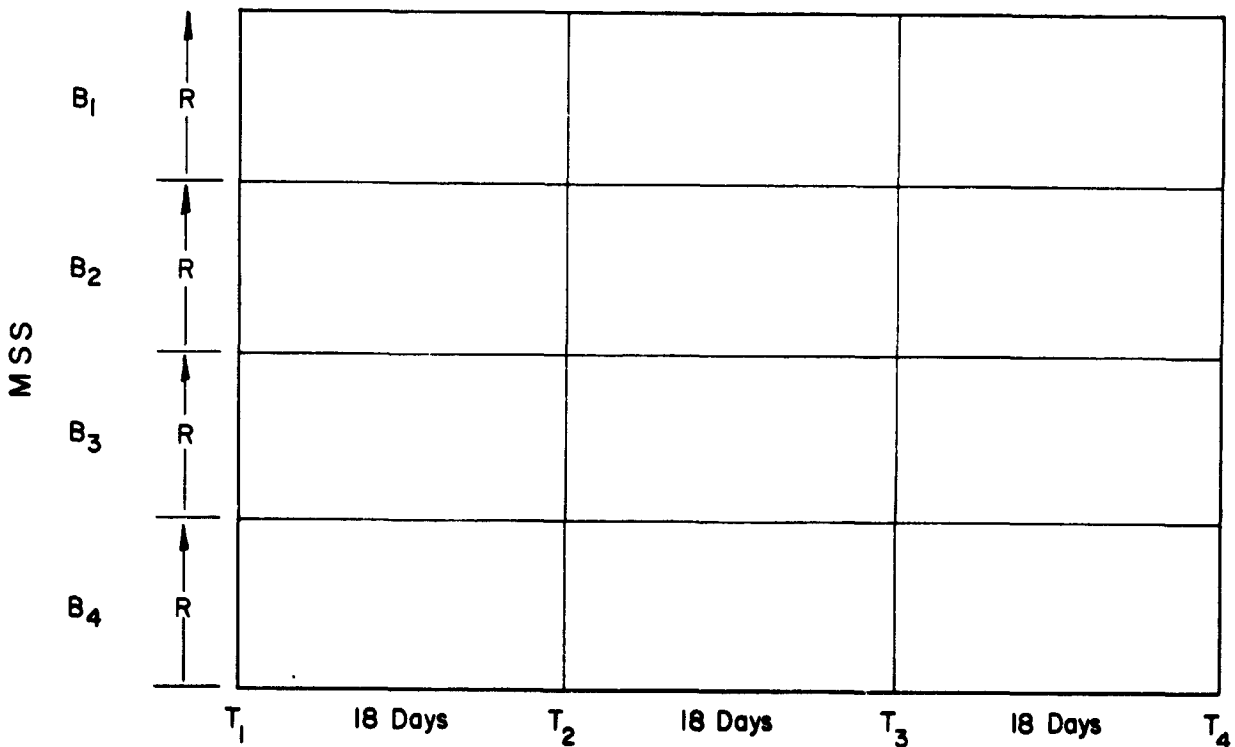
b.)    MSS Band

Figure 26    Display of Reflectance for Each Spectral Band
as a Function of Time and Site Location

42

The time trends of ERTS sensor radiances could be easily monitored along with the comparative time trends of ground-truth data. As soon as a statistically valid sample is obtained; e. g. , perhaps a week to a week-and-a-half after launch, the trend envelope would be defined and valid judgements would be possible.

4.5 Data Classification File Entries

The calibration measurements should be made available to data users through the Data Classification activities. This activity, providing a continuing monitoring of image quality, should receive the information measured by the Calibration Monitor (CM) and log it as a classification entry for the appropriate data orbit or image frame. The entry should identify, if possible, the magnitude of the calibration shift and its sign. A code should also be entered to identify whether the corrections have been applied to the routine data or will be applied only on special order data.

Since the ground-truth data, the aircraft, or in situ surface and meteorological measurements obtained in the calibration monitor procedure are of scientific interest, they too should be carefully documented and disseminated. The documentation of these data should include the location, time, observing instrumentation, calibration checks, etc. The ground-truth data would be extremely useful for subsequent correlation studies between changes in surface reflectance and other physical properties of the surface and subsurface materials. The dissemination of these data can be achieved by their inclusion in the ERTS data catalog. The exact formatting of the data catalog is currently under investigation and will be presented in greater detail in a subsequent report.

## 5. RECOMMENDATIONS

In this study, we have examined the use of ground-truth data to monitor calibrations of sensors in ERTS. We have not, however, fully explored the use of these ground-truth data in the computation of correction factors and the optimum data-processing techniques incorporating these correction factors. Possible procedures for these activities of the ERTS Data Center, we feel, should be actively investigated.

In the area of ground-truth measurements, we recommend that an investigation be conducted of the relationship between high-resolution, surface or near-surface radiometric and photometric measurements and low-resolution measurements of some surfaces made from aircraft or satellites. For surface with uniform characteristics, such as those recommended for the ground-truth sites in this report, the relationships between high- and low-resolution measurements are not difficult to derive. However, for most situations encountered in satellite-borne remote sensing, the nonuniformity of surfaces with variations smaller than the resolution of satellite sensors, often make it difficult to apply in situ ground-truth measurements in the computations of expected radiance or in the interpretation of the satellite data. We therefore recommend a program to conduct controlled measurements, at different spatial resolutions, over nonuniform surfaces whose point-to-point variations in radiometric and photometric properties are well-known. We further recommend that these measurements be used to develop spatial-averaging techniques by which high-resolution, ground-truth measurements can be effectively used to interpret and predict measurements made at satellite altitudes. The availability of such techniques would greatly increase the utility of satellite remote-sensing data.

44

REFERENCES

1.    Kondrat'yev, K. Y., "Actinometry",    965: NASA TT-F-9712, p 203.

2.    Moon, P. , "Proposed Standard Solar Radiation Curves for Engineering Use, "
      J. of Franklin Inst. , 30, 583-619.

3.    Johnson, 1961: Satellite Environment Handbook, Stanford University Press,
      Stanford.

4.    List, R. J. , 1966: Smithsonian Meteorological Tables, Sixth Revised Ed.
      Smithsonian Institution, Washington, D. C.

5.    Elterman, L. , 1968: UV, Visible, and IR Attenuation for Altitudes to 50 km,
      Air Force Cambridge Research Laboratories, AFCRL-68-0153.

6.    Fraser, R. S. , 1964: "Computed Intensity and Polarization of Light Scattered
      Outwards from the Earth and an Overlying Aerosol, " J. Opt. Soc. Am. ,
      54(2), 157-168.

7.    Coulson, K. L. , G. M. Bouricius and E. L. Gray, 1965: "Optical Reflec-
      tion Properties of Natural Surfaces, " J. of Geophysical Research, 70,
      4601-4611,

8.    Coulson, K. L. , 1966: "Effects of Reflection Properties of Natural Surfaces
      in Aerial Reconnaissance, " J. of Applied Optics, 5, 905-917.

9.    Coulson, K. L. , 1968: "Effect of Surface Reflection on the Angular and
      Spectral Distribution of Skylight, " J. of Atmos. Sci. , 25, 759-770.

10.   Coulson, K. L. , G. M. Bouricius and E. L. Gray, 1965:  Effects of Surface
      Reflection on Radiation Emerging from the Top of a Planetary Atmos-
      phere, Report No. R65-SD64, Space Science Laboratory, General Elec-
      tric Company, Philadelphia, 147 p.

11.   Krinov, E. L. , 1947: "Spectral Reflectance Properties of Natural Forma-
      tions, " (in Russian).   Translation by National Research Council of
      Canada, TT-439, Ottawa (1953).

12.   Kondrat'yev, K. Y. , Z. F. Mironova and A. N. Otto, 1964: "Spectral Albedo
      of Natural Surfaces, " Pure and Applied Geophysics, 59, 207-216.

13.   Kondrat'yev, K. Y. , 1965: "Actinometry" (in Russian).   NASA Technical
      Translation F-9712.

14.   Ashburn, E. V. and R. G. Weldon, 1956:"Spectral Diffuse Reflectance of
      Desert Surfaces," JOSA, 46, No. 8, 583-586.

15.   Orr, D. G. , S. E. Dwornik and L. M. Young, 1963: Reflectance Curves of
      Soils, Rocks, Vegetation and Pavement, Research Report No. 7746-RR,
      U. S. Army Engineer Research and Development Laboratories, Fort
      Belvoir, Va.  AD 410588.

REFERENCES, contd.

16.   Gerharz, R. and W. A. Fischer, Reflectance Measurements in the 0.6 to 2.5 Micron Part of the Spectrum, Technical Letter NASA-8, U. S. Dept. of Interior, Geological Survey (work performed under NASA Contract R-146), N66-21664.

17.   Kropotkin, M. A. and B. P. Kozyrev, 1964: "Study of the Reflection Spectra of Natural and Synthetic Materials in the .7 - 100 Micron Range," Optics and Spectroscopy, 17, No. 136.

18.   Hovis, W. A., 1968: Spectral Studies of Reflected Solar Energy: Fields, Red Tide, Kelp; 0.68 to 2.4 Microns; C-47 Aircraft, NASA Report No. X-622-68-451 (preprint), Goddard Space Flight Center, Greenbelt, Md.

19.   Hovis, W. A., 1970: Personal Communication.

20.   Steiner, D. and T. Guterman, 1966: Russian Data on Spectral Reflectance of Vegetation, Soil, and Rock Types, European Research Office, U. S. Army, Contract DA-91-591-EUC-3863/OI-652-0106.

21.   Shay, J. R. (ed), 1970: Remote Sensing, with Reference to Agriculture and Forestry, National Academy of Sciences, Washington, D. C.

22.   LeGault, R., 1970: Sources of Electromagnetic Radiation, AIAA Paper No. 70-287, Annapolis, Md.

23.   Scovel, M. J. L. et al, 1966: Atlas of Landforms, J. Wiley and Sons, Inc.

APPENDIX A

DETAILED DISCUSSION OF MAJOR GROUND TEST SITES

A.1     Smoke Creek and Black Rock Deserts

### Geography of the Calibration Site

The geographical location of the Smoke Creek and the Black Rock Deserts is shown in Figures A-1 through A-5. Figures A-1, A-2 and A-3 illustrate the configuration and the spatial distribution of both deserts. Figures A-2 and A-5 illustrate the geologic and geomorphic setting of the deserts. Figures A-6 and A-7 present aircraft views of the Smoke Creek Desert to demonstrate the spatial variations observed with high-resolution sensor systems.

Of the two deserts, the Black Rock Desert is the largest in aerial extent. This desert, however, is geographically less defined on the USGS topographical sheets (Figure A-1, Ref. 3) than the smaller Smoke Creek Desert. The desert extends for about 85 miles in a northeasterly direction and is approximately 20 miles wide. The width, however, is extremely variable, depending on the criteria of boundary delineation. Numerous intermittent streams and a few lakes occupy the northeastern portion of the desert. The Black Rock Desert is partly separated from the Smoke Creek Desert to the southwest of it by the Granite and the Selenite Ranges (Figure A-1). The Smoke Creek Desert is smaller in size, has well-defined geographical boundaries and has been studied in more detail (Ref. 1). Its location, only 10 miles north of the Pyramid Lake (Figure A-1) is also favorable for calibration purposes.

On the basis of this preliminary examination it is suggested that only the smaller Smoke Creek Desert be used as a potential ground calibration test site. The description of this site, presented below, is based mostly on the Clancy and Rush study (Ref. 1).

### Geomorphology

The Smoke Creek Desert is approximately 35 miles long and 10 miles wide, comprising about 1120 sq. mi. in valley area. The mountainous boundary of Smoke Creek Desert includes Granite Range at the northeast, Buffalo Hills at the north, a group of mountains belonging to an unnamed group of highlands at the west, Terraced Hills at the south and Fox Range at the east (Figure A-5). The highest mountain peaks in Smoke Creek Desert are Granite Peak (altitude: 9056 ft)

47

of Granite Range; Observation Peak, Spanish Springs Peak and Shinn Peak (altitude: 7964, 7526 and 7562 ft, respectively) in the western highlands; and Pah Rum Peak (altitude: 7606 ft) of Fox Range.

Geomorphologically, this desert is a plain surrounded by high mountains. More than 80% of the desert surface is a gently sloping and undulating lowland, situated approximately 5236 ft below the surrounding mountain divides. Of the entire lowland, the playa surfaces make up about 30% of its valley area. Altitude of the playa surface of Smoke Creek Desert ranges from approximately 3855 ft at the south to approximately 3820 ft near the northeast end.

The general local relief of the site is as follows (Figure A-1, Refs. 1 and 3):

| Blank Areas | 0 - 35 ft | (3820 to 3855 ft) |
|---|---|---|
| Stippled | 0 - 300 ft | (3855 to 4155 ft) |
| Solid | 0 - 4901 ft | (4155 to 9056 ft) |
| Total Relief | 5236 ft | |

### Geology

The desert valley floor is mantled by Quaternary terrestrial basin fill, made up primarily of sands and small patches of alluvium. The consolidated rocks surrounding the desert have been eroded to form pediment surfaces along the edge of most of the mountain fronts and are generally mantled with a relatively thin layer of alluvial material. The detrital fill is of uniform composition, derived almost totally from the Tertiary and partly Pliocene volcanic formations surrounding the basin. A small fraction of the sediment, however, is made up of sedimentary mineral suits wasted away from the Jurassic and Triassic formations that outcrop in the southeast portion of the surrounding ranges. A generalized geologic map is included (Figure A-2) depicting the general distribution of the source material for the basin fill.

### Soil Cover and Vegetation

The desert is underlain by an arid soil cover with poor pedogenic horizons. The soil is low in organic matter and lacks moisture for plant growth for long periods.

Alluvium in the desert consists of rock debris derived from the surrounding mountain ranges. As stated previously, the lithologic composition of the fragmental constituents generally reflects the composition of those ranges.

48

Thickness of the alluvium ranges from a mantle commonly less than a foot thick over much of the uplands, to more than a thousand feet in the valley troughs and the desert basin.

The desert surface and especially the playas and their peripheral areas are mantled by relatively thin eolian deposits. This material is moderately permeable where the individual grains are mostly sand-sized.

Due to hot, arid conditions, vegetation is largely absent. A sparse sagebrush steppe may be present along the few intermittent streams and playas.

Phreatophytes make up another group of vegetation, growing around the edges of playas and along larger creeks (Figure A-5). In this area they consist mainly of greasewood, saltgrass and rabbit brush; also, some cottonwood and willows grow in spring and seep areas.

### Climate and Hydrology

The area can be characterized as having an arid climate with low relative humidity and an abundance of sunshine. Summers have a relatively short growing season and large diurnal temperature fluctuations. Precipitation occurs as summer thundershowers, winter rains, and snowfall. Periods of low temperature are common during winter months.

The average monthly and seasonal precipitation during the year varies greatly. Maximum and minimum monthly averages range from 0.13 inches to 0.76 inches at Gerlack, Nevada, located at the north end of Smoke Creek Desert (Figure A-1). Precipitation during the six-month period from December through May at Gerlack averages 65% of the mean annual precipitation.

During periods of high-intensity rainfall or during snowmelt periods, part of the runoff reaches the desert floor but most of it is lost by evaporation. The runoff reaches and floods the lower depressions of the desert about every two or three years on the average. The exact magnitude of frequency of playa flooding is, however, unknown. Nonetheless, over the long term and for natural conditions, inflow to, and outflow from, an area are equal provided that the long-term climatic regime remains constant. Due to the irregularity in the quantity and duration of precipitation, only a limited number of perennial streams exist in the desert.

2A

USGS Map, 1959
Owyhee River Area

SCALE : 1/1,000,000

0    10    20 Mi.

115°

115°

DESERT

ROCK

BLACK

41°

41°

Gerlach

SMOKE CREEK DESERT

Area shown
in Fig. A-6

Area shown
in Fig. A-7

PYRAMID LAKE

40°

40°

Figure A-i    Owyhee River Area Relief Map

SCALE : 1/2,500,000

0       25mi       50

119°

USGS Geologic Map, 1960
Smoke Creek and Black Rock Desert

41°                41°

40°                40°

119°

LEGEND

6    Quaternary Alluvium
     and Sand

5    Pliocene Extrusive Volcanics
     (Basalt, Tuft, Rhyolite) and
     Interbedded Sedimentary Rocks

4    Miocene Sedimentary Deposits
     and Lenses of Volcanic Rocks

3    Tertiary Volcanic Rocks
     (Undifferentiated)

2    Triassic and Jurassic Undifferentiated
     Sedimentary and Metamorphic Rocks

1    Jurassic, Cretaceous, Some Tertiary
     Intrusive Volcanics (Granodiorite,
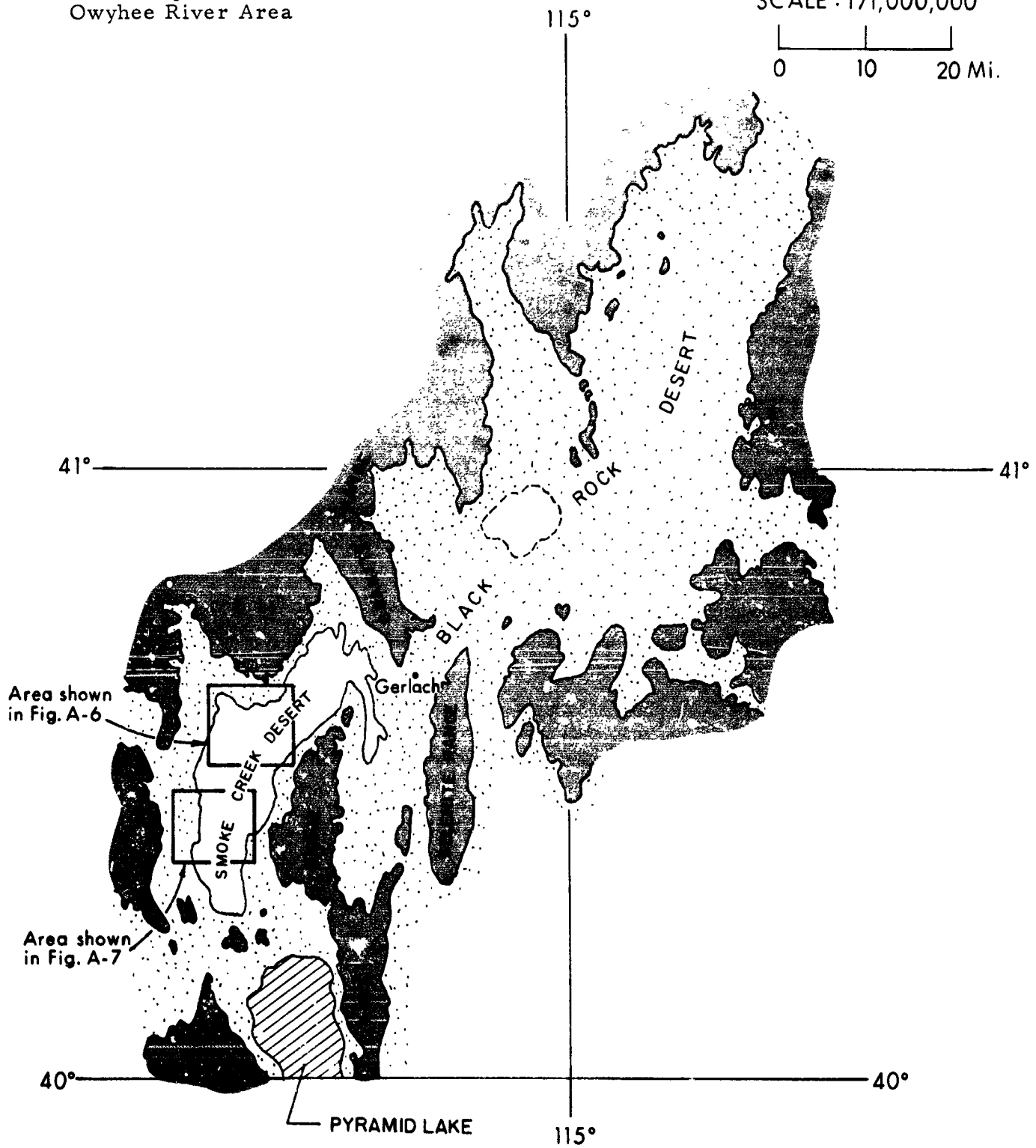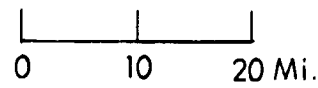     Gabbros, etc. )

Figure A-2    Smoke Creek and Black Rock Desert Area Geological
              Map

51

The Times Atlas, 1957
Pyramid Lake, Smoke Creek
and Black Rock Deserts

SCALE: 1/2,500,000

0    20    40    60 St. Mi.

119°

120°

41°                                                41°

40°                                                40°

120°              119°

PYRAMID L.

LEGEND

3    Desert
2    Playas
1    Highlands

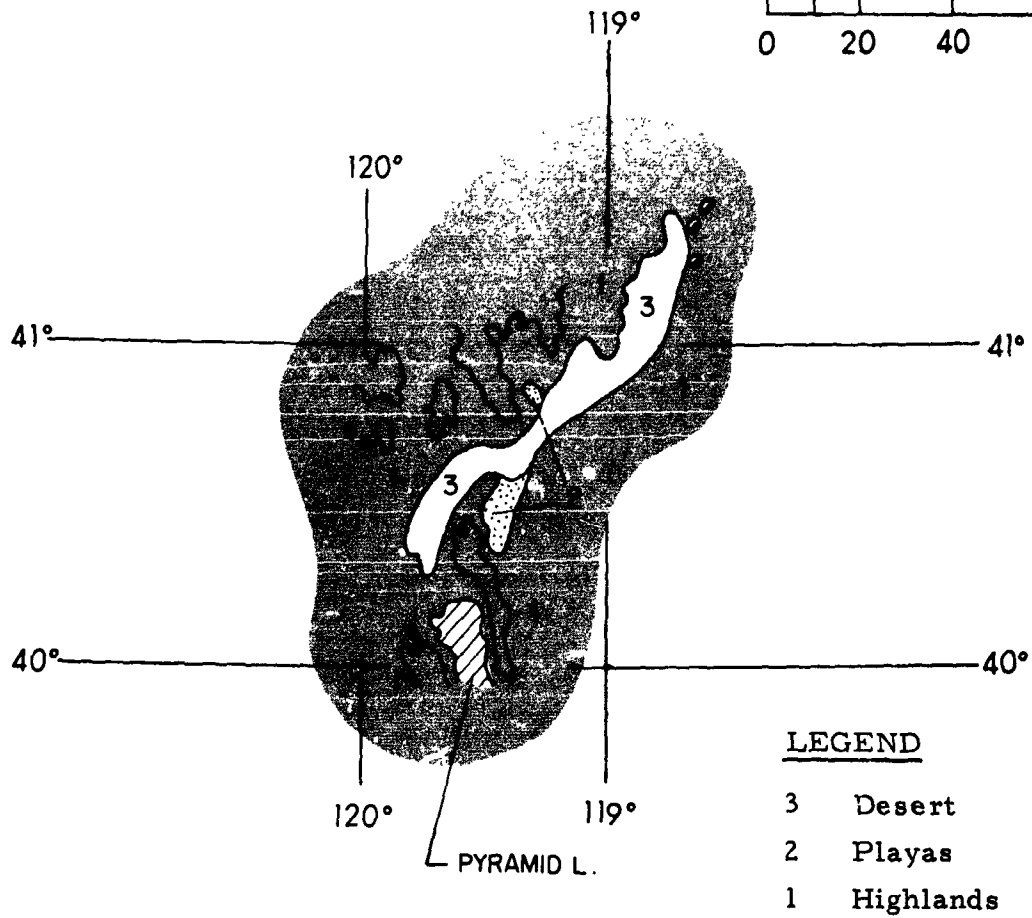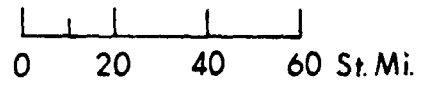Figure A-3   Pyramid Lake, Smoke Creek and Black Rock Desert
             Area Relief Map

52

Nimbus I AVCS, Orbit 124
Pyramid Lake, Smoke Creek
and Black Rock Deserts

LEGEND

3    Desert

2    Playas

1    Highlands
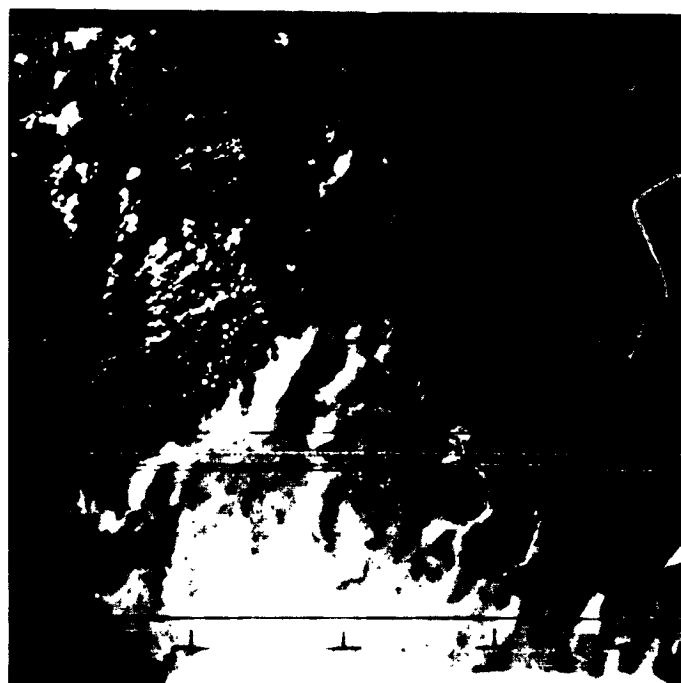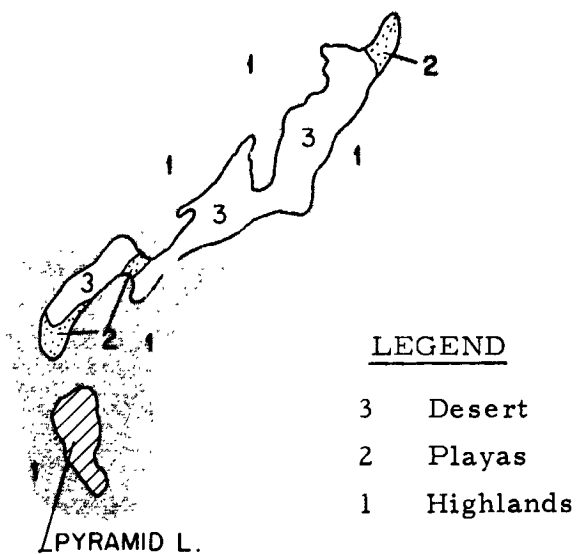


Figure A-4  Smoke Creek and the Black Rock Desert Area as
Viewed by Nimbus I

Clancy and Rush, 1968
Smoke Creek Desert Area

GRANITE RANGE

BUFFALO HILLS

SCALE

1 2 3 4 5 Mi

UNNAMED HIGHLANDS

SMOKE CREEK DESERT

DRY VALLEY

TERRACED HILLS

SAN EMIDIO DESERT

LAKE RANGE

LEGEND

4   Desert
3   Phreatophytes
2   Alluvium
1   Bedrock

Figure A-5   Smoke Creek Desert Area Relief Map

54

Figure A-6    Aircraft View of Smoke Creek Desert Area

Figure A-7   Aircraft View of Smoke Creek Desert Area

## A.2     Great Salt Lake Desert

### Geography of the Calibration Site

The geographical location of the Great Salt Lake Desert is shown in Figures A-8 through A-11.  Figure A-8 is a conventional geographic map of the Test Site;  Figure A-9 shows the desert as it is viewed by the Nimbus I (AVCS) meteorological satellite;  and Figure A-11 illustrates the geologic setting of the prop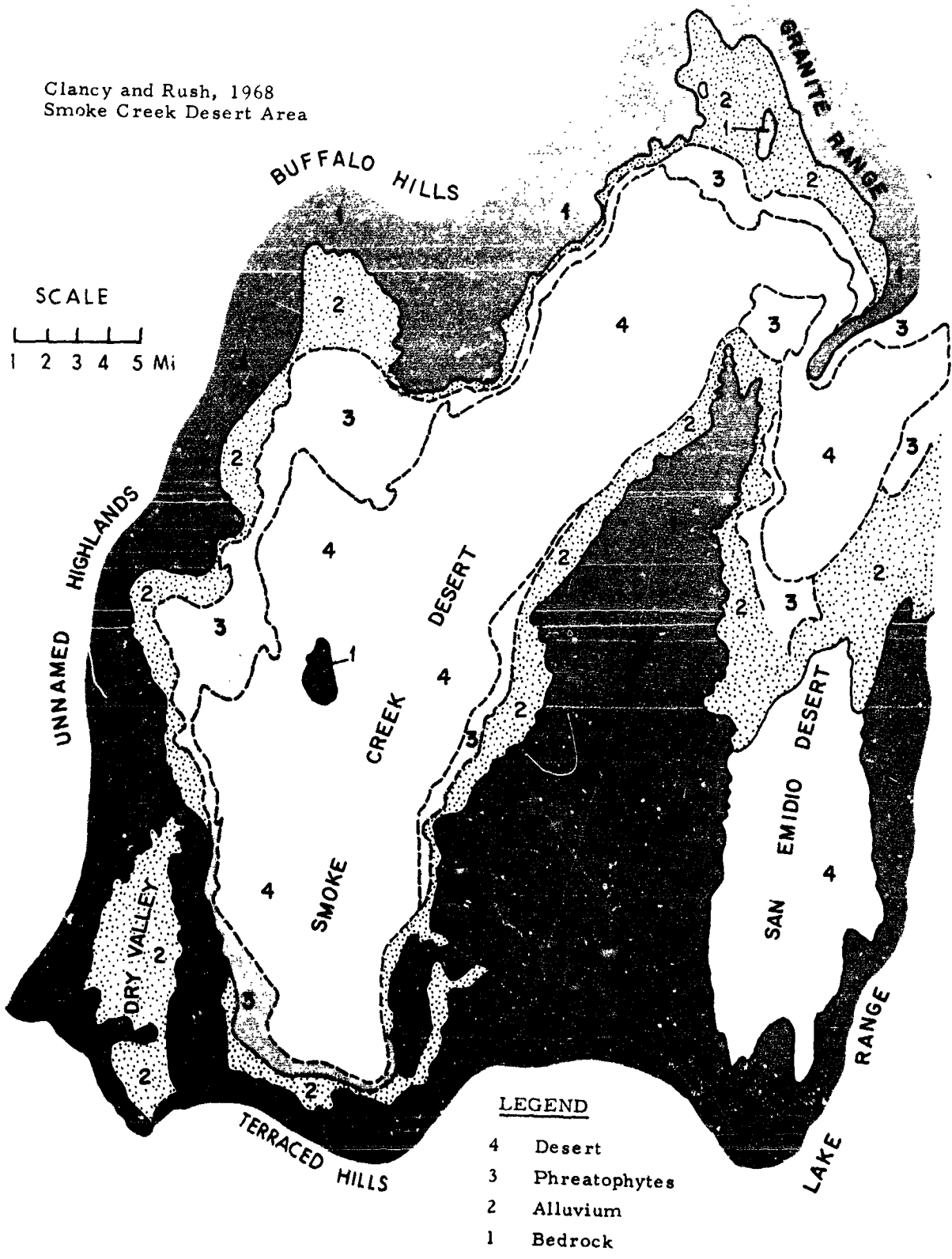osed calibration site.  Figures A-12 and A-13 present aircraft views of the desert.  Note the general lack of homogeneous areas in comparison with the Nimbus view.

The Great Salt Lake Desert is a broad, flat, low area situated southwest of the Great Salt Lake in northern Utah.  Figure A-8 illustrates the position of the mountain ranges surrounding the desert.

### Geomorphology

The Great Salt Lake Desert is an elongate depression approximately 50 miles wide and 110 miles long, extending in a north-south direction.  The floor of this intermontane basin is situated approximately 1984 ft below the highest peak (Pilot Peak) of the ranges (Pilot Ranges) in the west.  The highest relief in the east (Cedar Mountains) is approximately 868 ft.  The floor of the desert is not a uniformly flat plain;  the irregularities, however, are at this time unknown due to the lack of this information in published reports.  Several erosional remnants break the continuity of the desert floor and stand out as prominent mounts -- Newfoundland Mountains, Wildcat Mountain, etc., (see Figure A-8).  Overall, the land-surface form of this desert is classified (Ref. 5) as a flat plain with more than 80% of area gently sloping and with more than 75% of this slope being lowland.

In general, the soil cover of the desert floor is classified as a warm soil (Ref. 5) whose mean annual temperature is higher than $47^{\circ}F$.  Due to sparse and sporadic precipitation, the soil cover lacks moisture for plant growth for long periods.  The pedogenic horizon is thin and low in organic matter.  The soil is of Pleistocene lacustrine origin, composed texturally primarily of clay, sand and gravel.  The sand fraction predominates over gravel.  The mineralogical composition varies, with recent mineral components being derived from the erosion and weathering of the surrounding ranges made up primarily of sedimentary strata (Figure A-10).

USGS Map, 1955
Great Salt Lake Desert

SCALE: 1/1,000,000

0    10    20 mi.

GOOSE CREEK MTS.

HOGUE MTS.

PILOT RANGE

NEWFOUNDLAND MT.

GREAT SALT LAKE

41°

TOANA RANGE

Area shown in Fig. A-12

LAKESIDE MTS.

GOSHUTE MTS.

GREAT SALT LAKE DESERT

Area shown in Fig. A-13

WILDCAT MT.

CEDAR MT.

SKULL VALLEY

OCHRE MT.

41°

113°

113°

LEGEND

4    Standing Water
3    Desert
2    Playas
1    Highlands
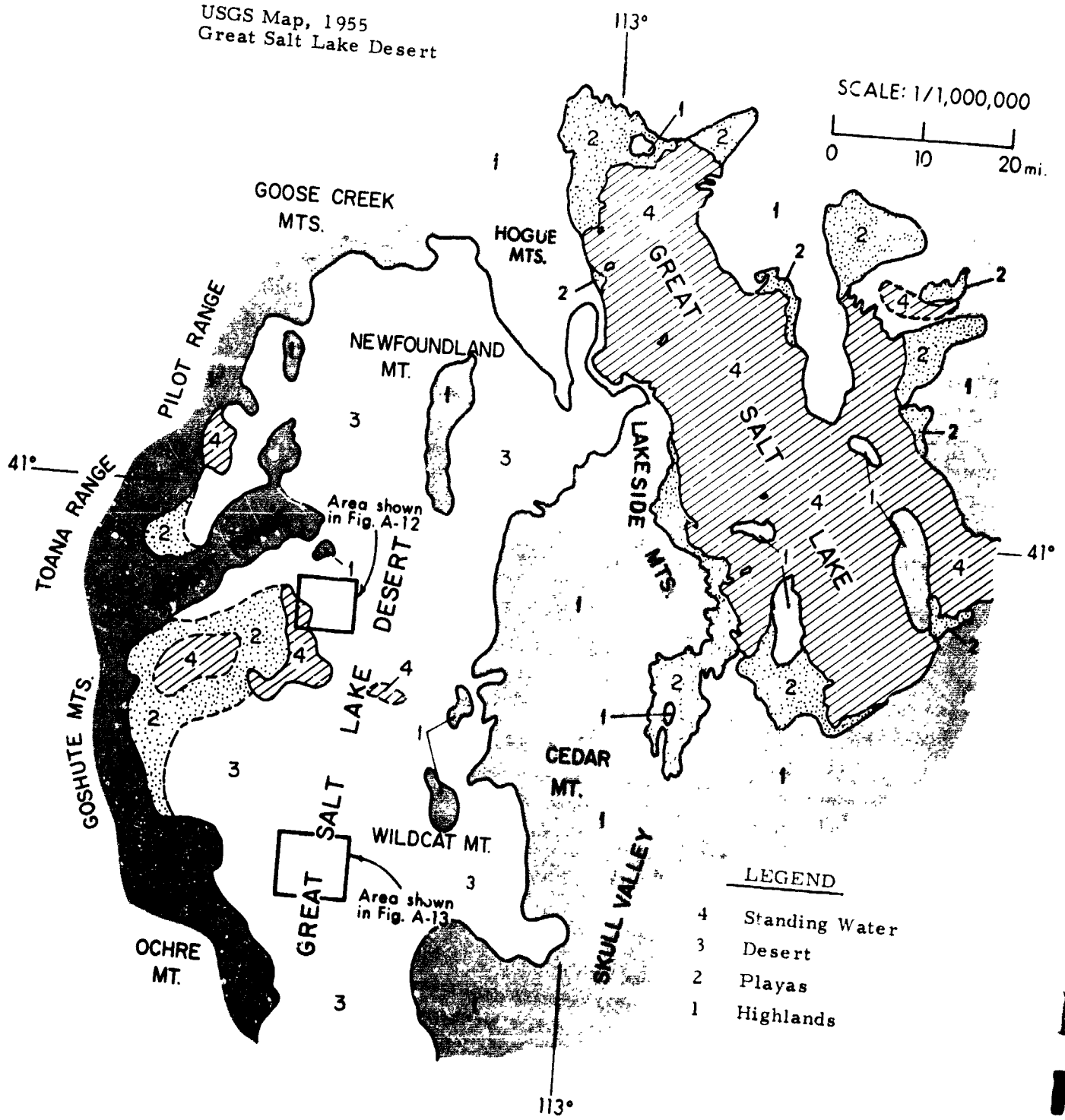
Figure A-8    Great Salt Lake Desert Area Relief Map

Figure A-9    Great Salt Lake Desert Area as Viewed by Nimbus I

SCALE: 1/2,500,000

LEGEND

11  Quaternary Alluvium
    and Sand

10  Pliocene and Pleistocene
    Continental Deposits and
    Associated Rocks

9   Carboniferous Rocks
    (Limestone, Shale,
    Quartzite, etc. )

8   Silurian and Ordovician
    Rocks (Limestone,
    Quartzite, etc. )

7   Cambrian Rocks (Limestone,
    Shale, Quartzite, etc )

6   Paleozoic Rocks
    (Undifferentiated)

5   Pre-Cambrian (Schist,
    Gneiss, Granite)

4   Pre-Cambrian Undivided
    Beltian Series

3   Pliocene and Younger Volcanic
    Rocks and Interbedded Continental
    Beds (Basalt Flows, Tufts, etc. )

2   Tertiary Intrusive Rock
    (Volcanic)

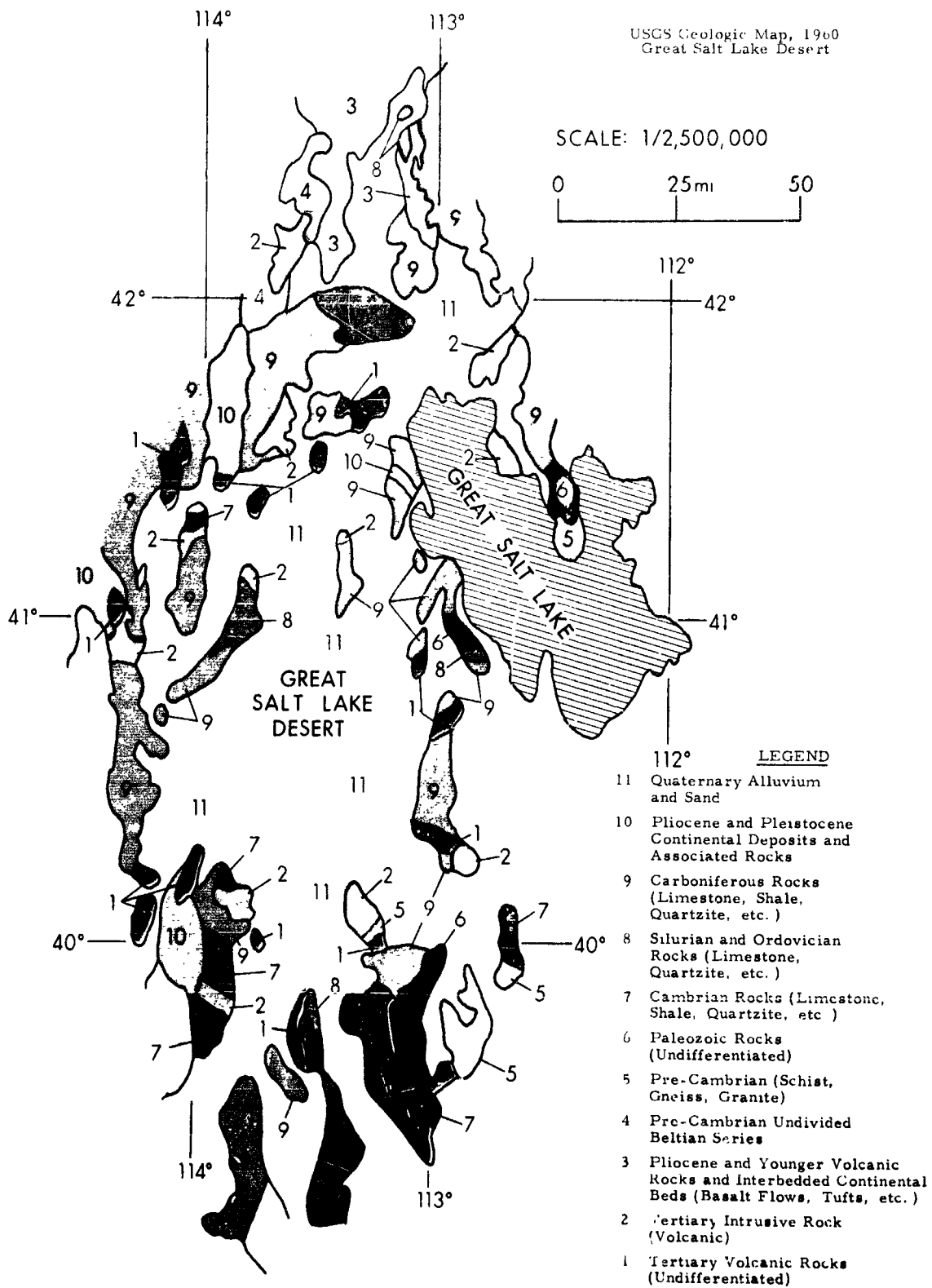1   Tertiary Volcanic Rocks
    (Undifferentiated)

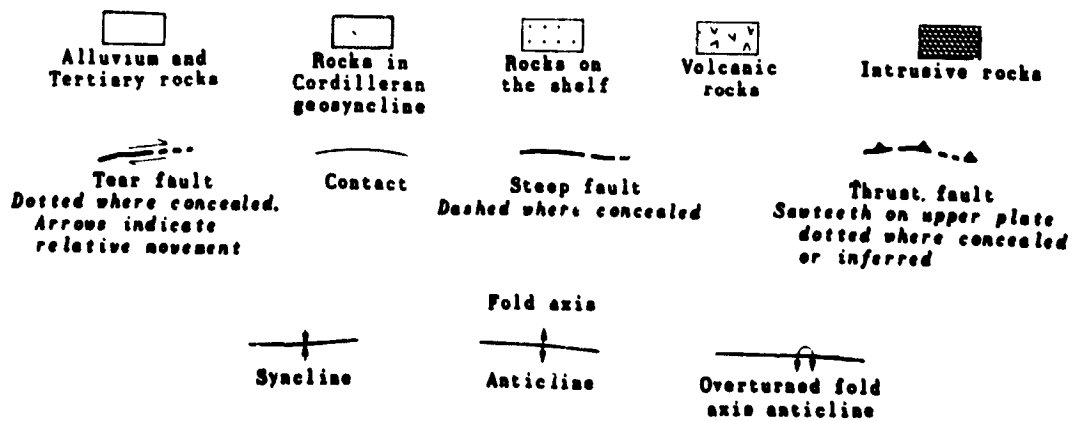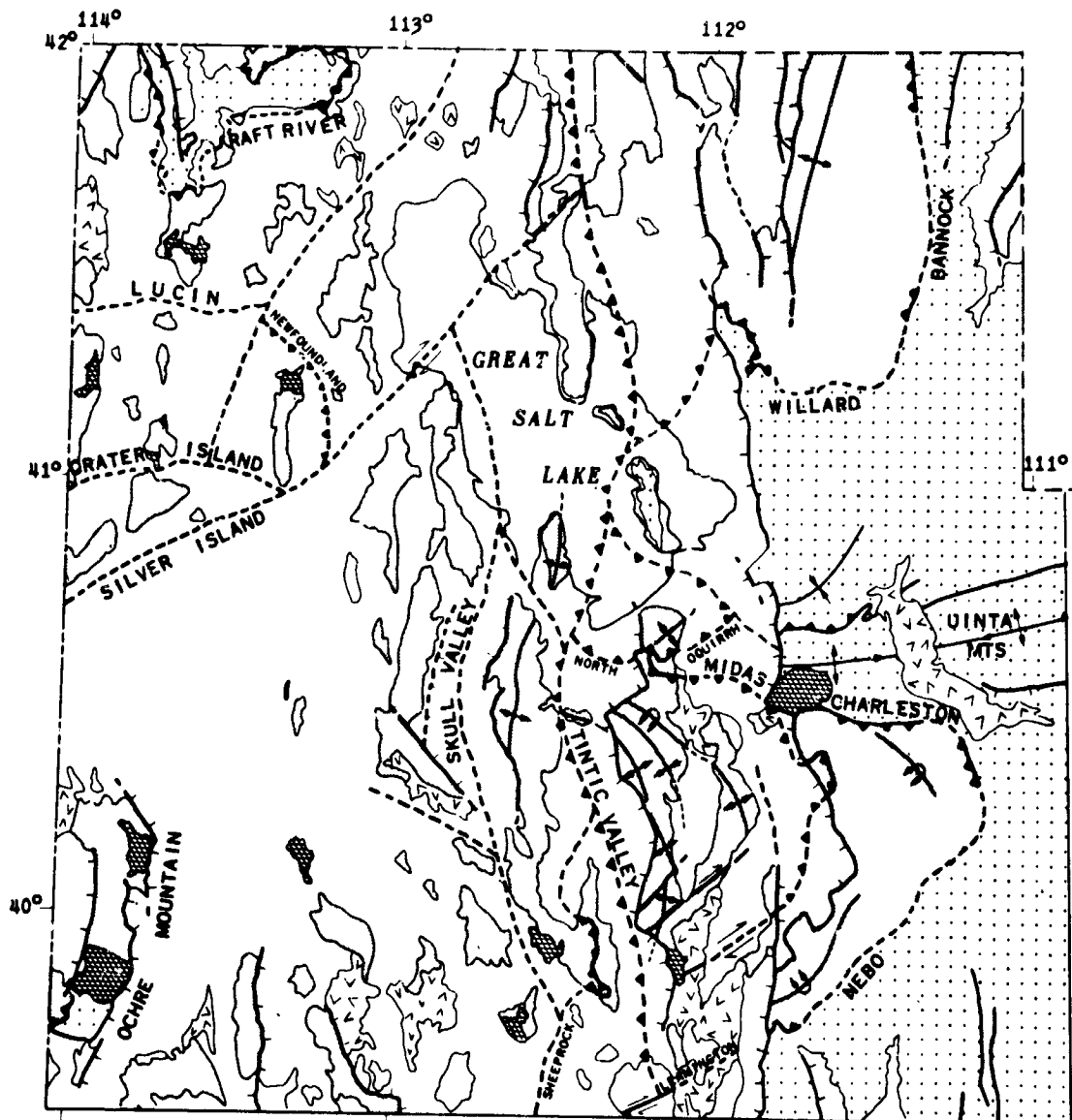Figure A-10  Great Salt Lake Desert Area Geologic Map

Figure A-11 Structural Map of Northwestern Utah Showing Major
Thrust and Tear Faults

61

Figure A-12 Aircraft View of Great Salt Lake Desert Area

Figure A-13 Aircraft View of Great Salt Lake Desert Area

Hydrological conditions in the Great Salt Lake Desert vary from month to month and year to year. Regardless of the fluctuating runoff, however, the drainage for the most part of the year is in the form of intermittent streams and small lakes of high-salinity playas. Water in any appreciable quantities reaches the desert floor as direct precipitation and as runoff mostly from the Wasatch Mountains and High Plateaus of Utah in the east.

The low annual precipitation and the resulting poor pedogenic soil horizon of low-organic content do not support a dense and varied vegetal cover. Overall, the vegetation is almost totally absent on the floor of the desert. Occasional patches of saltbrush-greasewood (Atriples-Sarcobatus) and Juniper-pinyon woodland (Juniperus-Pinus) may occur, but are confined mostly to the slopes and highland region (Ref. 5).

### Geology

Figure A-10 illustrates the distribution of bedrock geology surrounding the proposed test site. Block-faulting in western Utah and eastern Nevada produced a succession of northerly elongate ranges and the intervening semi-arid lowlands, of which the Great Salt Lake Desert is one. These intervening valleys are now filled with alluvium deposited from the Pleistocene to Recent times and covered in part by Tertiary lavas. The structural sketch map (Figure 11) illustrates the complexity of the geotectonics in the Great Salt Lake Desert region (Ref. 7).

A. 3   Sonoran Desert

### Geography of the Calibration Site

The geographical location of the Sonoran Desert is shown in Figures A-14, A-15, and A-19. Figure A-14 is a conventional geographic map of the Test Site; Figure A-15 shows the desert as it is viewed by the Nimbus I (AVCS) meteorological satellite; Figures A-16 and A-17 are Apollo 502 views of the area; and Figure A-18 illustrates the geologic setting of the proposed calibration site.

The Sonoran Desert occupies part of Mexico and part of the United States. In the United States it is located in the southwest region of Arizona (Figure A-19) and is, as mentioned previously, part of the Basin and Range physiographic province. Figures A-14 and A-19 illustrate the location of the major mountain ranges surrounding the desert.

## Geomorphology

The Sonoran Desert is characterized by a great preponderance of broad desert plains over mountain ranges. The ranges are relatively short and far apart, and generally have low elevations. The floor of the desert is approximately 1100 ft above sea level.

The most impressive feature of the landscape is the sharp contrast between steep and rugged mountains and wide expanses of desert plain. The plains merge with the smooth evenly graded alluvial slopes. The slopes attain considerable altitude where they meet the mountain fronts, but they scarcely detract from the general striking contrast between mountain and lowland. Such topography is characteristic of most mountainous desert regions. The debris is washed from the mountains and deposited in the adjacent valleys, thus gaining in areal extent and becoming more plainlike as the minor elevations are worn down and buried (Ref. 9).

The surface forms of the Sonoran Desert may be classified into three groups (Ref. 10):

1.  The mountains, commonly rugged and steep-sided, with either bare rock at the surface or only a thin cover of talus.

2.  The pediments, smooth carved-rock plains that generally border the mountains and are strewn with a thin, but discontinuous mantle of gravel.

3.  The bajadas, smoothly rounded alluvial aprons that slop forward into the axes of the "valleys".

Of these, the mountains and pediments are chiefly carved by erosion; the bajadas are chiefly depositional.

The basin fill commonly exhibits two lithologic facies, a coarse and commonly conglomeratic bajada type that was deposited around the outer margins of the basins, and a finer lacustrine facies deposited in the central parts of the basins.

Most of the landscape is to a varying degree the product of multiple geomorphic processes. At one time the intermontane basins were attributed in varying degrees to wind erosion. It is now generally believed that running water has played a greater role in developing the existing landscape than the wind, but locally the wind is an effective agent. All of the geomorphic processes, with the possible exception of solution by ground water, are operating in the province, but four in particular have produced the land forms that constitute the major part

of the present landscape. These are erosion and deposition by both concentrated and unconcentrated running water, wind erosion and deposition, volcanism and diastrophism. Their relative importance varies from place to place. More local in importance than the others are volcanism and wind action (Ref. 13).

The desert has an internal drainage and, because of the aridity, lacks any outlets to the sea. Additionally, because of aridity, the soil cover is thin, with a poor pedogenic horizon. The soil is of the warm, dry type, classified as aridisol. It is poor in organic content and is never moist as long as three consecutive months. The vegetal cover is consequently also extremely sparse, or nonexistent. Creosote bushbur sage (Larrea-Franseria) and Palo verde-cactus shrub (Cercidium-Opuntia) occupy the slopes of the more fertile localities and the highland areas (Ref. 5).

Geology

The rocks of the Sonoran Desert section as a whole are older than those of the Smoke Creek and Great Salt Lake Deserts. Precambrian granites and gneisses are much more widely exposed and thick sections of Paleozoic, Mesozoic and Cenozoic rocks are notably scarce. This difference is probably the result of two factors: (1) This region has been uplifted more than at the north, thus permitting erosion to penetrate more deeply into the geologic section. (2) It is in a more advanced stage of arid land pedimentation. The landscape here is also characterized by mountain ranges and intervening basins, commonly called bolsons, but typically the ranges are smaller, lower, and less extensive than in the Great Basin section. It may well be said that pediments and bajadas dominate the topography (Ref. 13).

A large proportion of the detached mountain ranges in the Sonoran Desert province consists of Paleozoic and Mesozoic sedimentary rocks. To the south in the area that extends to the coast, they consist of volcanic rocks and granite. The ranges of sedimentary and volcanic rocks appear to be detached roof pendants of a large granite batholith or more likely a group of coalescing batholiths.

The granite intrusions have complicated the sedimentary and volcanic rocks by metamorphosing and shattering them close to the contact and by jointing them excessively for some distance from the contact. Alternations of competent and incompetent strata, such as are found in parts of the Paleozoic and the Jurassic Barranca formation, show such a confusion of dips and small faults that it is very difficult to work out the main structural features. Only the most massive, resistant formations, such as the Permian limestone and the upper part of the Barranca formation, show the structure clearly and even these only at some distance from

66

the nearest granite contact (Ref. 11).   The mountains in part are clearly upfaulted.
Some still preserve the form of tilted blocks, although considerably modified by
erosion.   Some of the depressions are down-faulted, and some over-thrusting is
present in the Sonoran Desert.   In general, however, the structural elements of
this region have not been fully mapped.   A cursory analysis of Gemini and Apollo
photographs reveals a vast number of lineaments (faults, joints, fractures, etc. )
that do not appear on any published geological map of the area.

The Times Atlas, 1957
Sonoran Desert and Sand Hills

SCALE: 1/2,500,000

0   20   40   60 St.Mi.

* Also Called Algodones Dunes
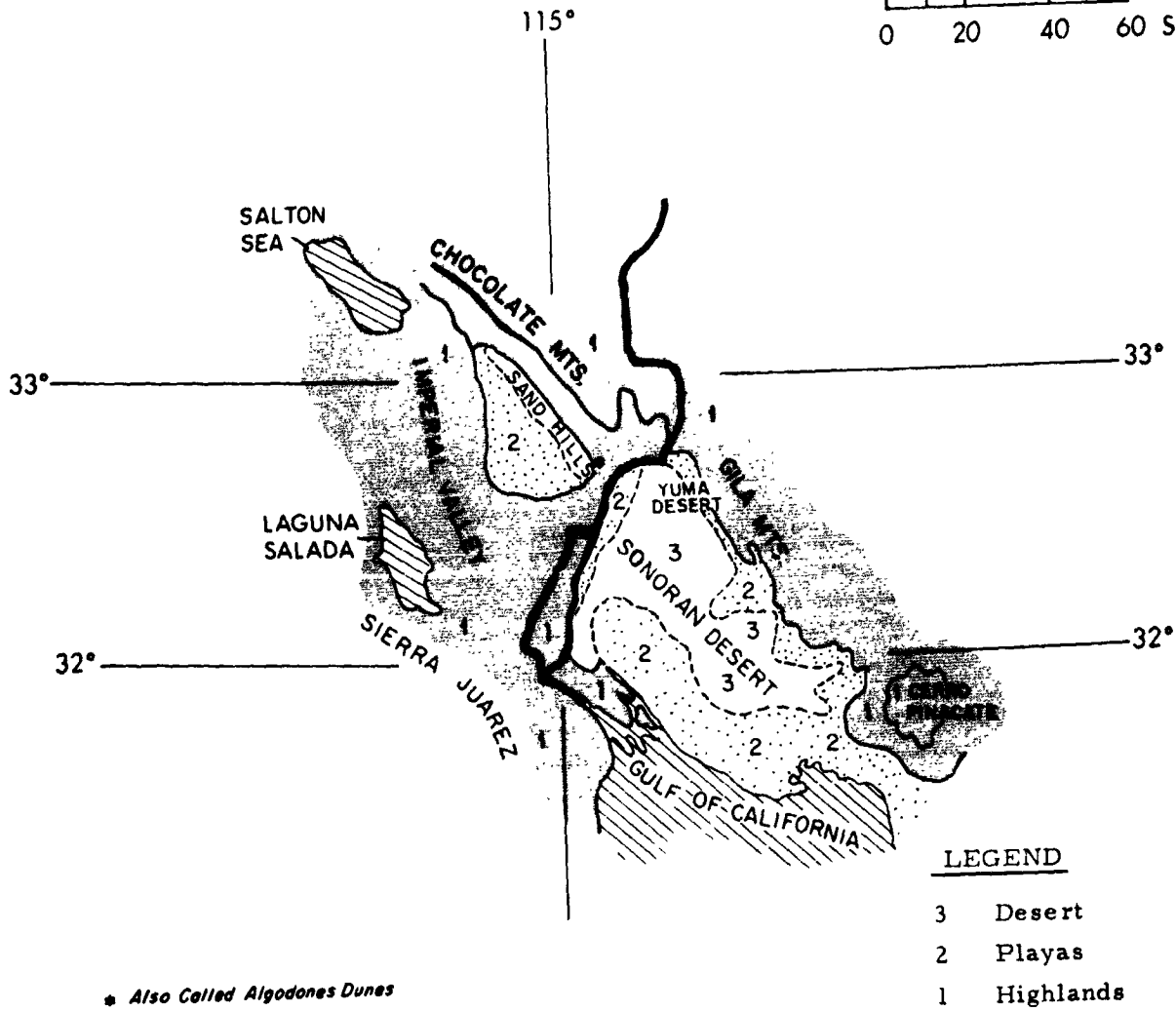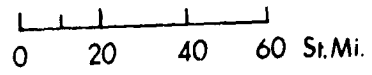
LEGEND

3   Desert
2   Playas
1   Highlands

Figure A-14 Sonoran Desert and Sand Hills Area Relief Map

Nimbus I AVCS, Orbit 80
Sonoran Desert and Sand Hills



SAND HILLS
(ALGODONES DUNES)
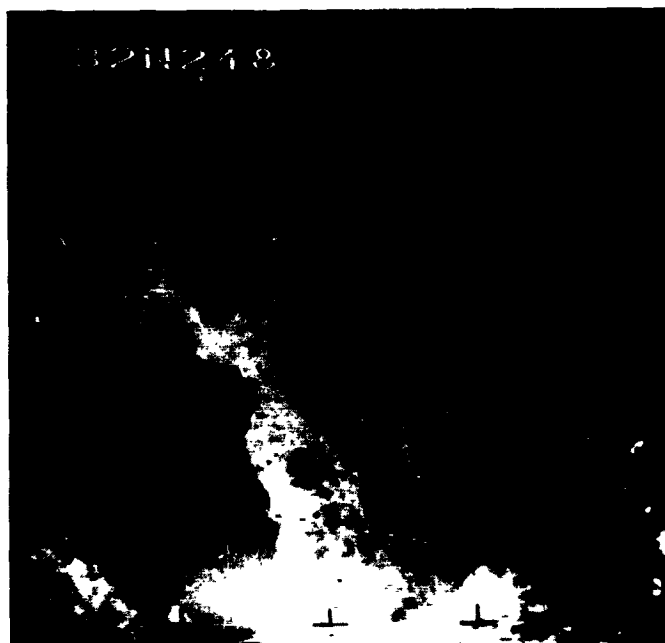
LEGEND

4    Hills
3    Desert
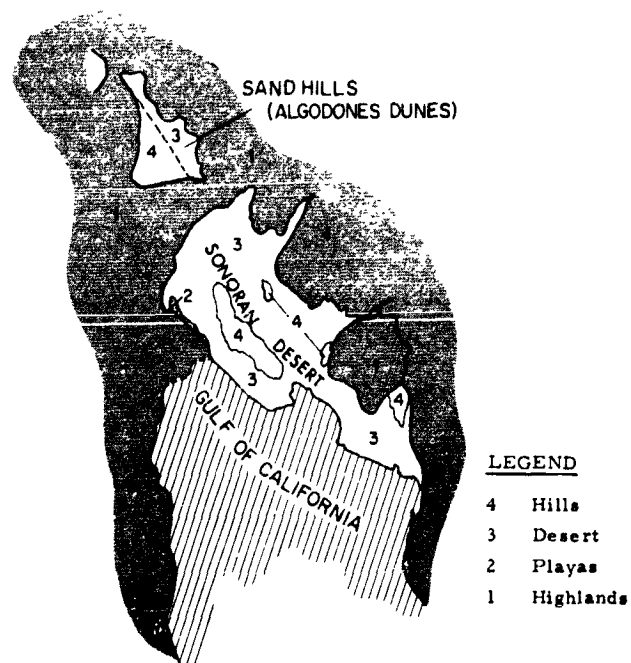2    Playas
1    Highlands

**Figure A-15  Sonoran Desert and Sand Hills Area as Viewed by Nimbus I**

69
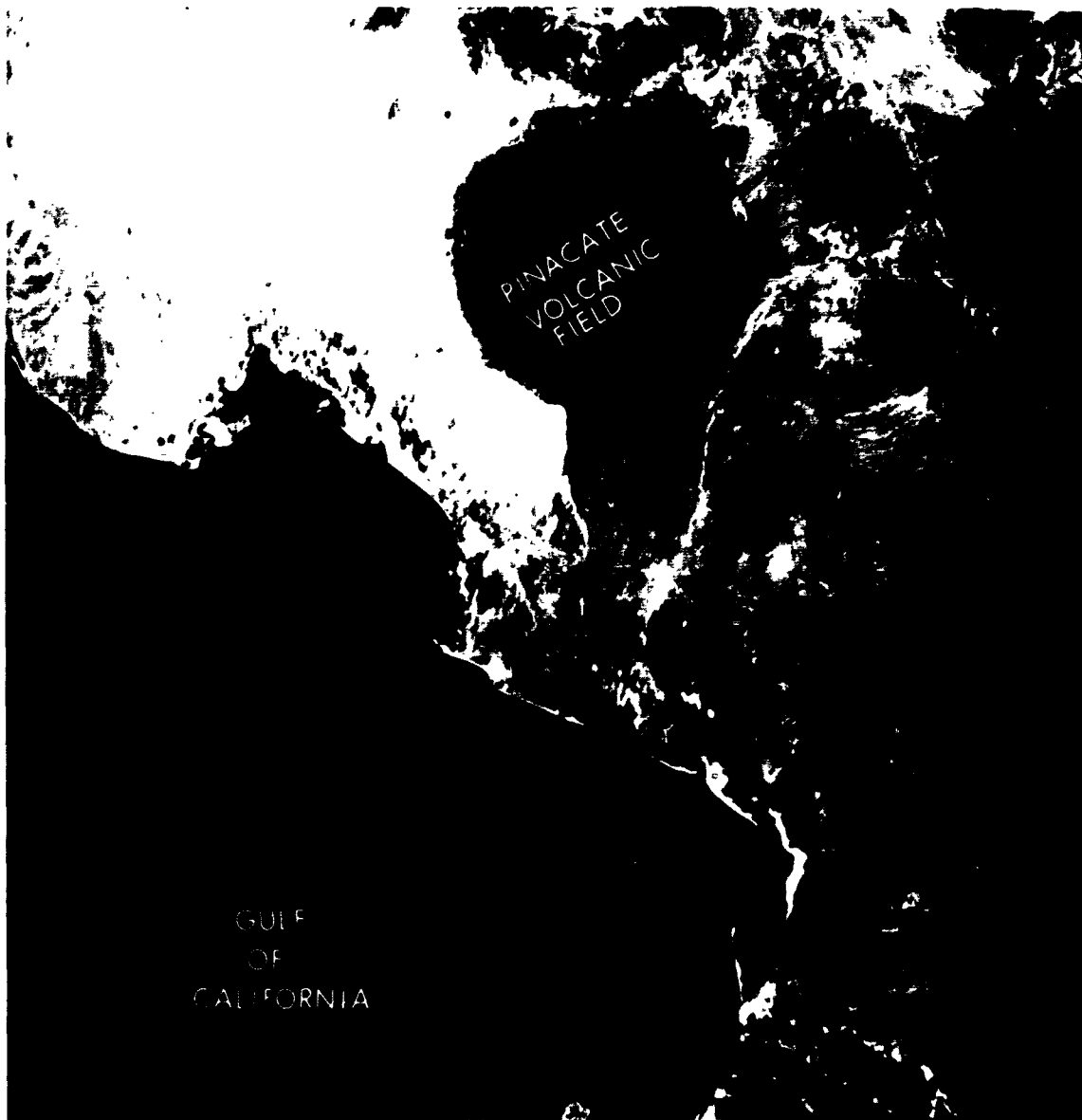
Figure A-16  Sonoran Desert and Pinacate Volcanic Field as
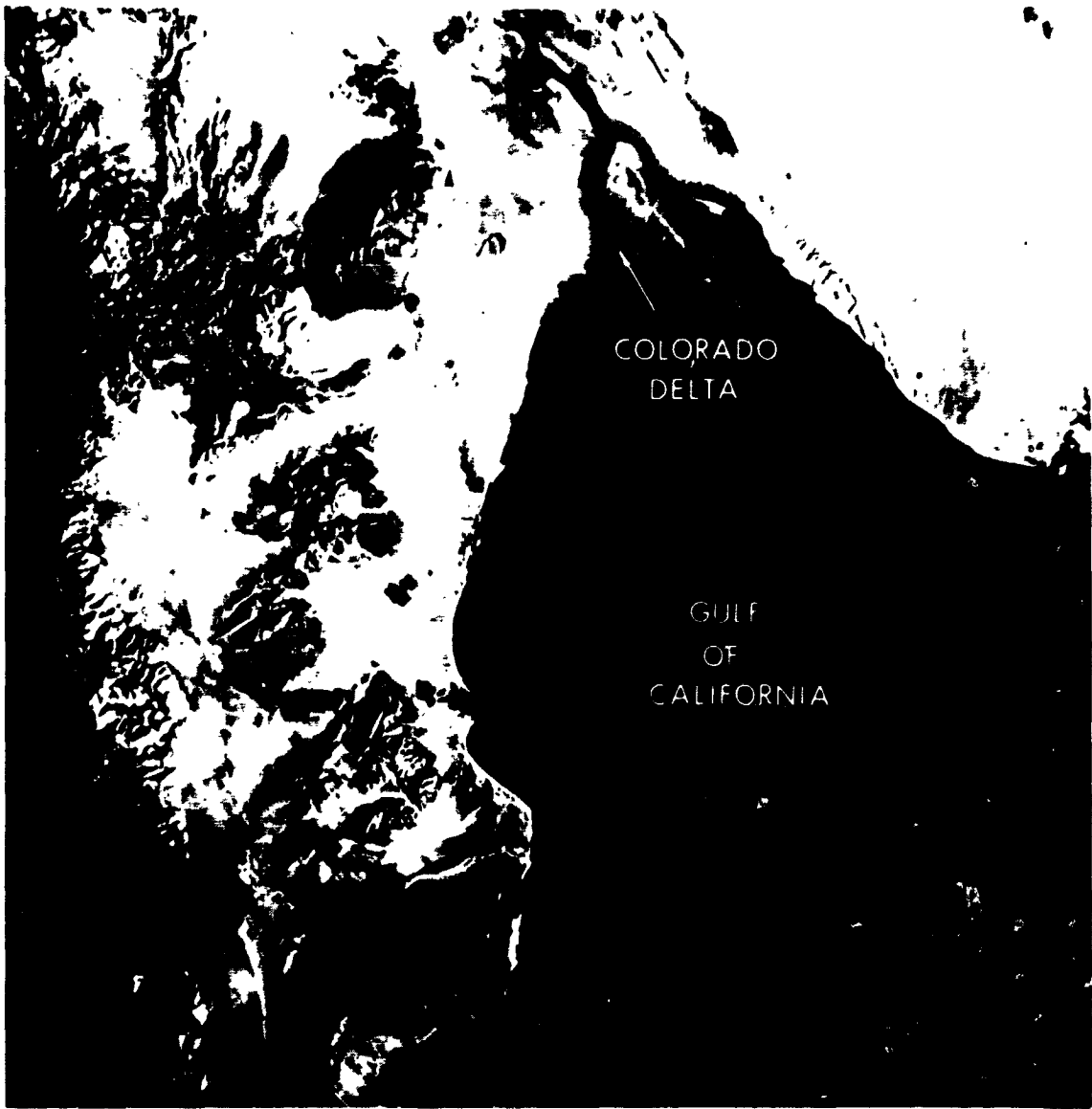Viewed by Apollo 502

COLORADO
DELTA

GULF
OF
CALIFORNIA

Figure A-17 Sonoran Desert and Colorado River Delta as Viewed
by Apollo 502

Geologic and Tectonic Map
Sonoran Desert Area

SCALE : 1/ 5,000,000.



LEGEND

7    Quaternary Terrestrial Volcanic Rocks

6    Mostly Tertiary Terrestrial Volcanics
     of Differing Composition and Degree of
     Deformation

5    Tertiary Marine Sedimentary Basin
     Deposits.   Deformed by Cenozoic
     Orogenies

4    Jurassic and Cretaceous Eugeosynclinal
     Deposits (Mostly Strongly Metamor-
     phosed by Mesozoic and Later Orogenies)

3    Cambrian to Jurassic (Mainly Jurassic)
     Miogeosynclinal Deposics.   Deformed by
     Laramide Orogeny (Late Mesozoic)
     Mostly Sedimentary Rocks

2    Late Jurassic to Middle Cretaceous
     Volcanic Rocks - Granite Plutons

1    Triassic, Jurassic and Middle Creta-
     ce us Rocks.   These Eugeosynclinal
     Deposits are Mostly Volcanics,
     Deformed (Metomorphosed by Nevedan)
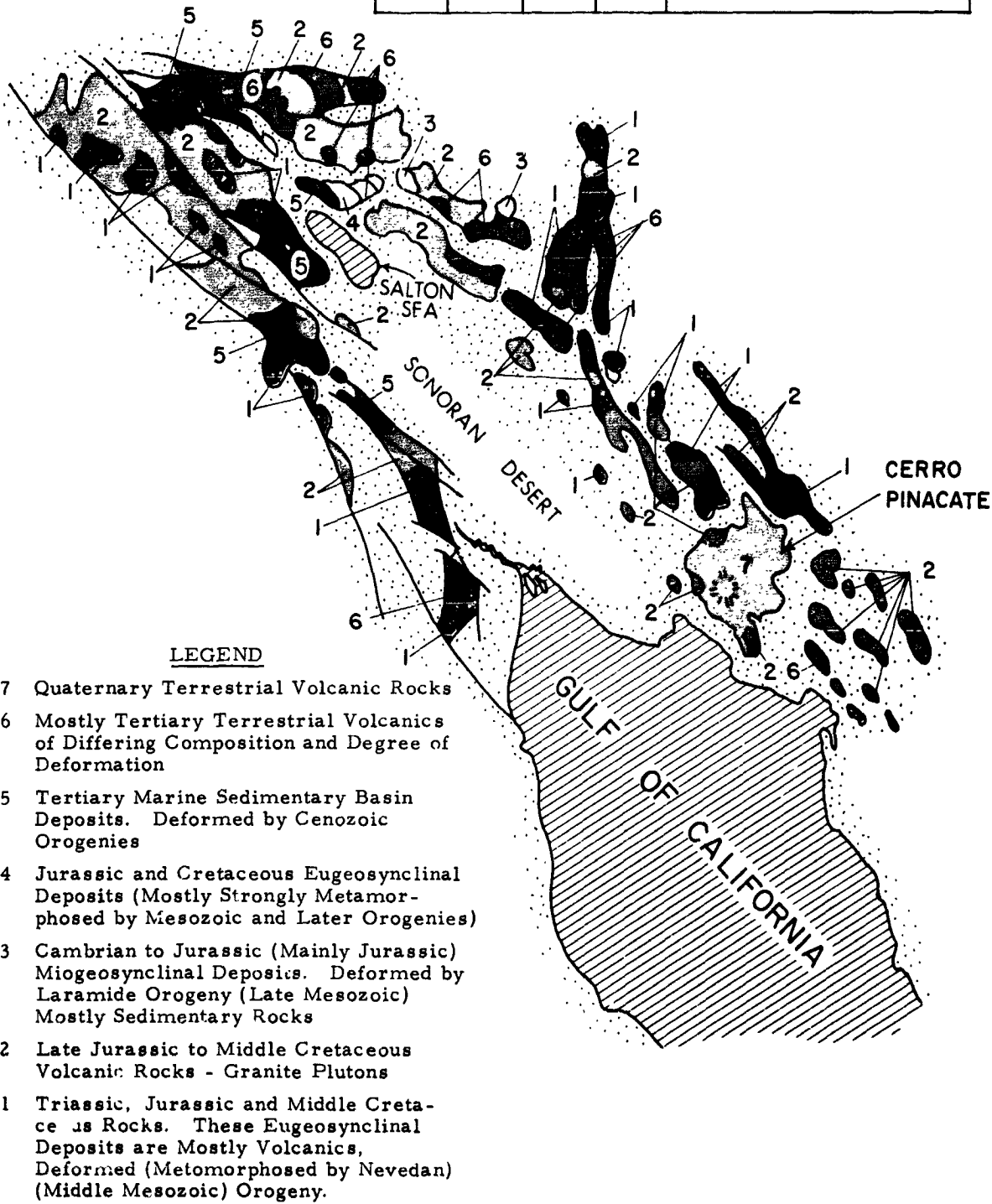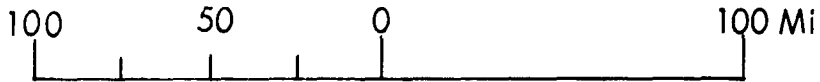     (Middle Mesozoic) Orogeny.

Figure A-18 Geologic and Tectonic Map of the Sonoran Desert Area
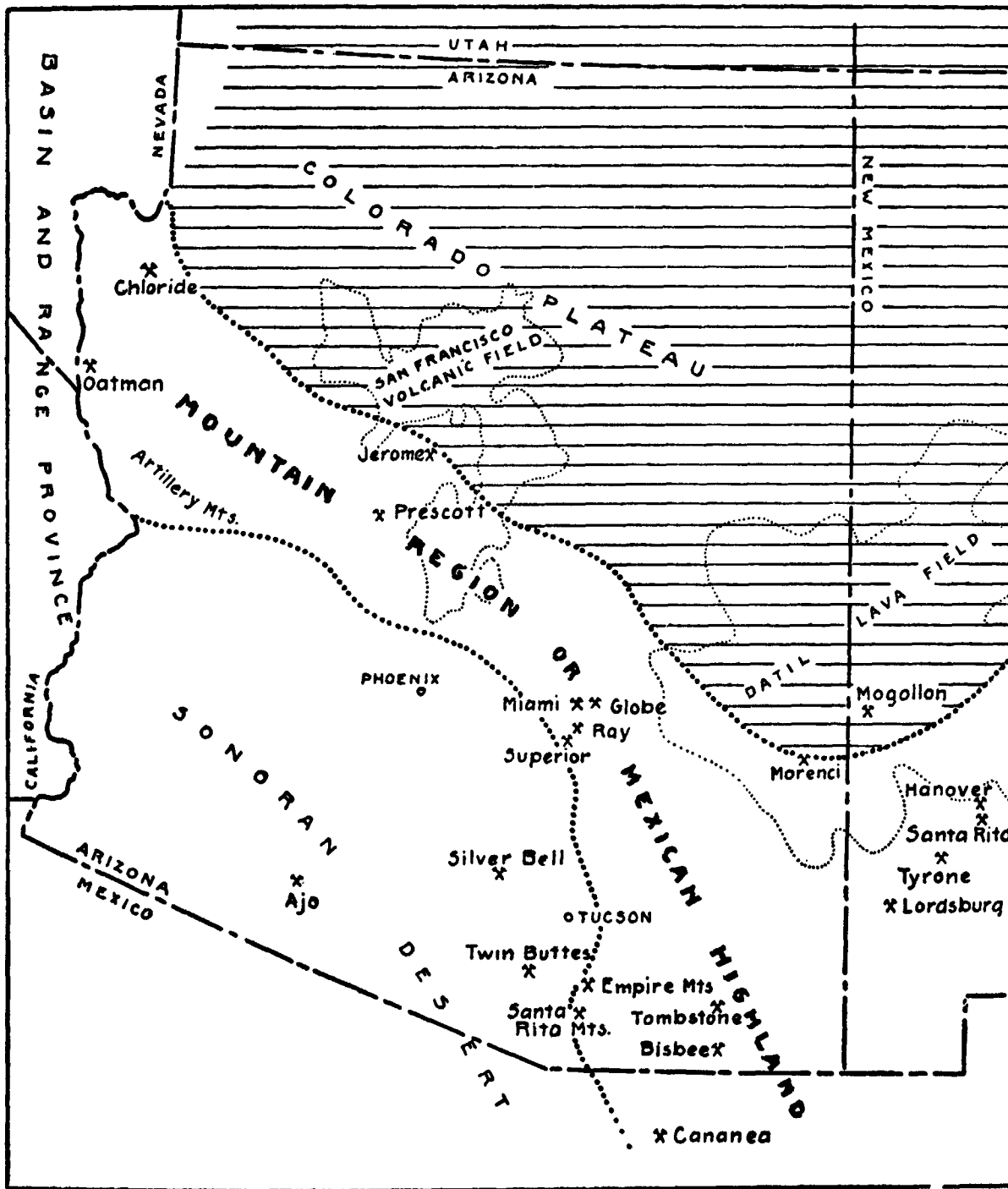
72

Figure A-19 Index Map of Arizona Showing the Central Mountain
Region and the Sonoran Desert Region. Both
Mountains and Desert Regions are Part of the Basin
and Range Physiographic Province

APPENDIX A

REFERENCES

1.  Clancy, P. A. and F. E. Rush, 1968: Water-Resources Appraisal of
    Smoke Creek - San Emidio Desert Area, Nevada and California;
    Water Resources Reconnaissance Series, U. S. Geological Survey
    Report No. 44.

2.  Geological Map of the United States, 1960, Scale 1/2,500,000: U. S.
    Geological Survey.

3.  Owyhee River, Map NK-11, 1959, Scale 1/1,000,000: U. S. Geological
    Survey.

4.  The Times Atlas, 1957, The Americas, V, Scale 1/2,500,000: Boston,
    Houghton Mifflin Company, The Riverside Press, Cambridge.

5.  National Atlas, 1969, Land-Surface Forms, Sheet No. 62, 86, 90, Scale
    1/7,500,000: U. S. Geological Survey

6.  Great Salt Lake, Map NK-12, 1955, Scale 1/1,000,000: U. S Geological
    Survey.

7.  Spencer, E. W., 1969: Introduction to the Structure of the Earth, McGraw-
    Hill Book Company.

8.  Eardley, A. J, 1962: Structural Geology of North America, Harper and
    Row Publishers.

9.  Ransome, F. L., 1933:"General Geology and Summary of Ore Deposits:
    in Ore Deposits of Southwest," Intern. Geol. Congr. Guidebook No. 14,
    pp 1-122.

10. Gilluly, J., 1937: "Physiography of the Ajo Region, Arizona", Bulletin,
    Geol. Soc. Am. 48, pp 323-347

11. King, R. E., 1939: "Geological Reconnaissance in Northern Sierra Madre
    Occidental of Mexico", Bulletin, Geol. Soc. Am. 50, pp 1625-1722.

12. Tectonic Map of North America, 1969, Scale 1/5,000,000: U S. Geological
    Survey.

13. Thornbury, W. D., 1965: Regional Geomorphology of the United States,
    John Wiley and Sons, Inc.

APPENDIX B

REFLECTANCE CURVES

The available optical data utilized in this study covers the visible and near-infrared spectrum to coincide with the proposed RBV and MSS spectral bands.

The following list correlates the referenced spectral reflectance curves for the three proposed calibration sites:

Smoke Creek Desert            Refs. 1, 2, 3, 5 and 7

Great Salt Lake Desert         Refs. 1, 2, 4, 5 and 7

Sonoran Desert               Refs. 1, 2, 3, 4 and 7

Literature references for the curves:

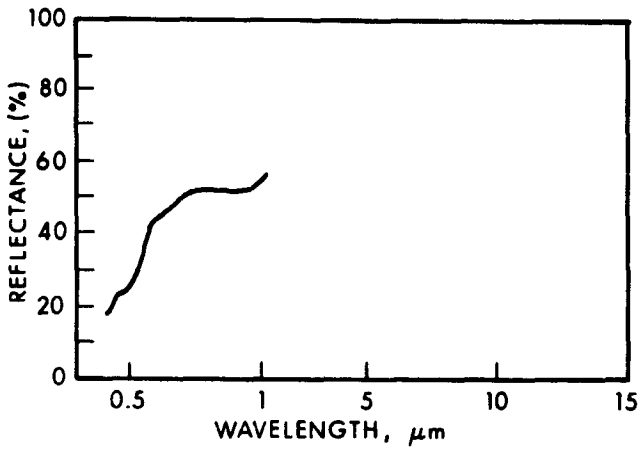| Author | Reference No. | Figure Nos. |
|---|---|---|
| Earing and Smith | 1 | 1 - 6 |
| Steiner and Guterman | 2 | 7 - 10 |
| Coulson, et al | 3 | 11, 12, 15 and 18 |
| Ashburn, et al | 4 | 13 |
| Krinov | 5 | Not reproduced |
| Orr, et al | 6 | 14 and 16 |
| Kropotkin, et al | 7 | Not reproduced |
| Kondrat'yev | 8 | 19 |
| Kondrat'yev | 9 | 17, 20 and 21 |

Figure B-1    Reflectance for Dry Yellowish
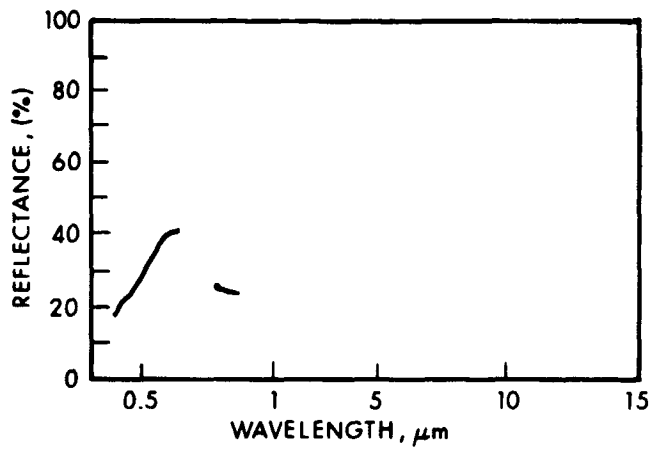Sand



Figure B-2    Reflectance for Whitish, Normal
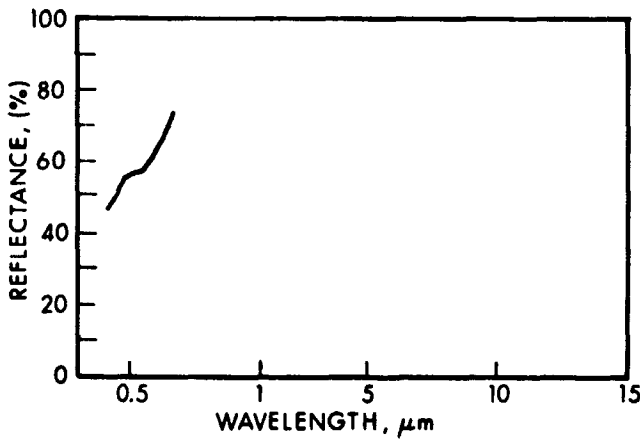Desert



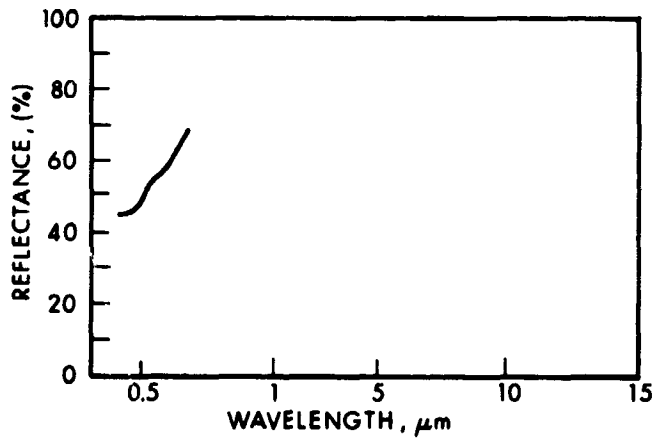Figure B-3    Reflectance for Salt Bed



Figure B-4    Reflectance for Non-Saline
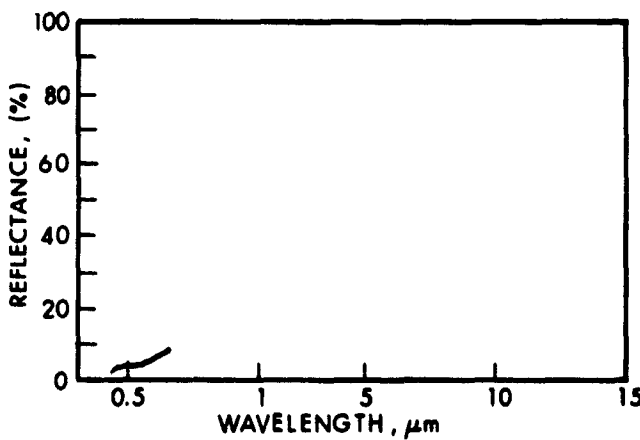Playa



Figure B-5    Reflectance for Light-Red
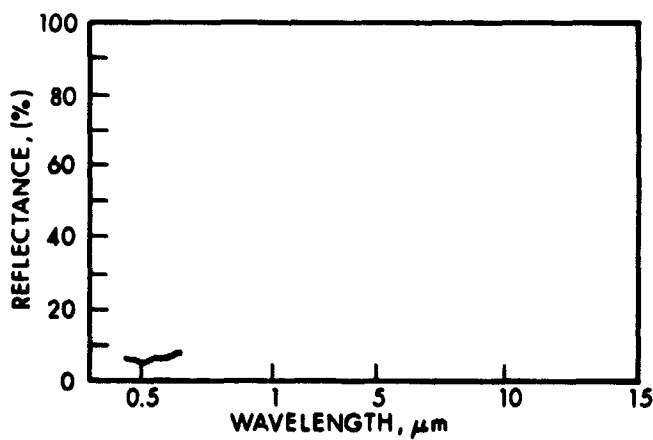Ground



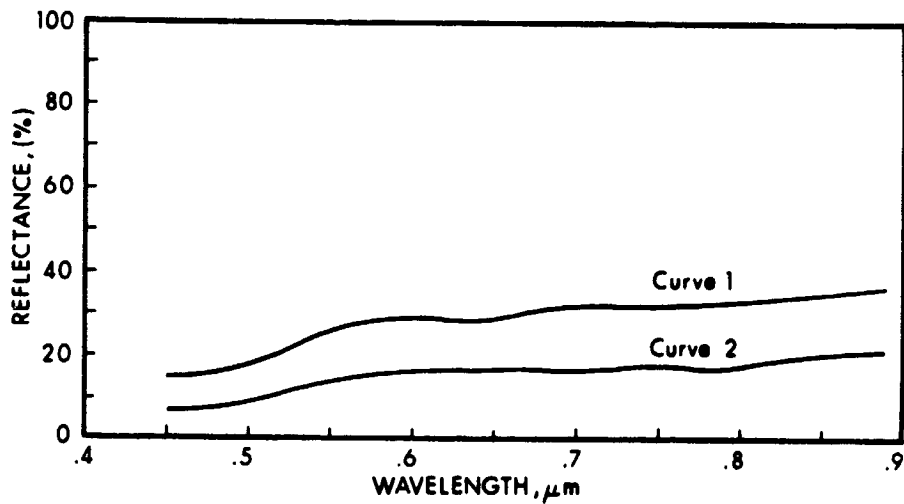Figure B-6    Reflectance for Dark Volcanic
Rock

76

Figure B-7    Reflectances for Dry (Curve 1) and Wet (Curve 2)
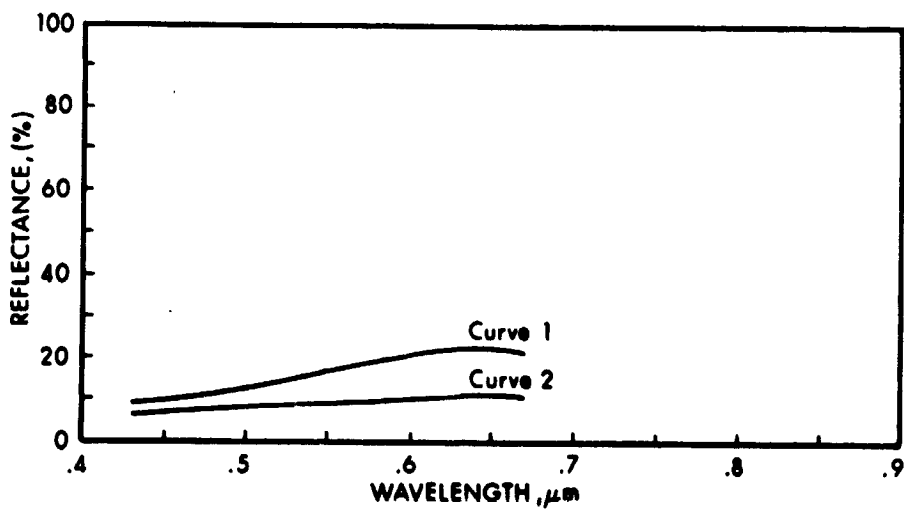Yellow Sand



Figure B-8    Reflectances for Volcanic Rock (Curve 1 is Freshly
Broken, Yellow-Gray Color and Curve 2 is Covered
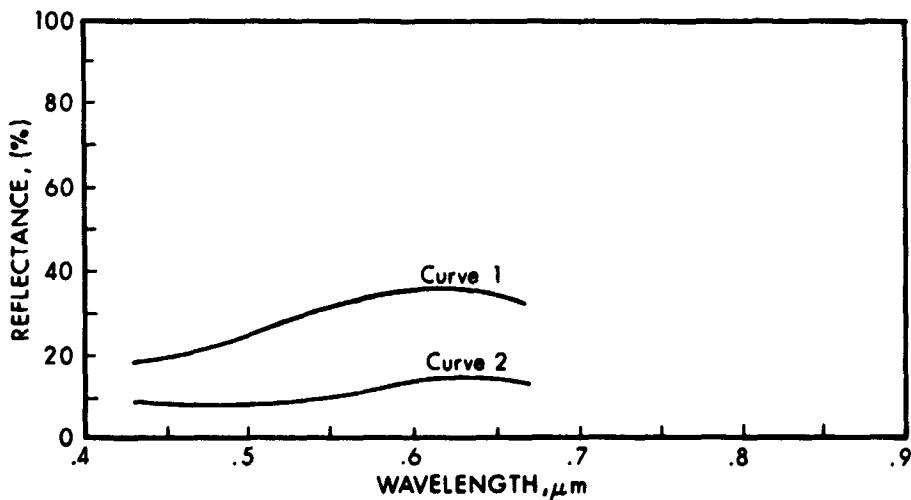with Desert Varnish, Black Color)

Figure B-9  Reflectances for Clay. (Curve 1 is Dark-Gray, Covered with a Thin Salt Crust and Curve 2 is Dark-Gray, Salt Crust Scratched Off.)
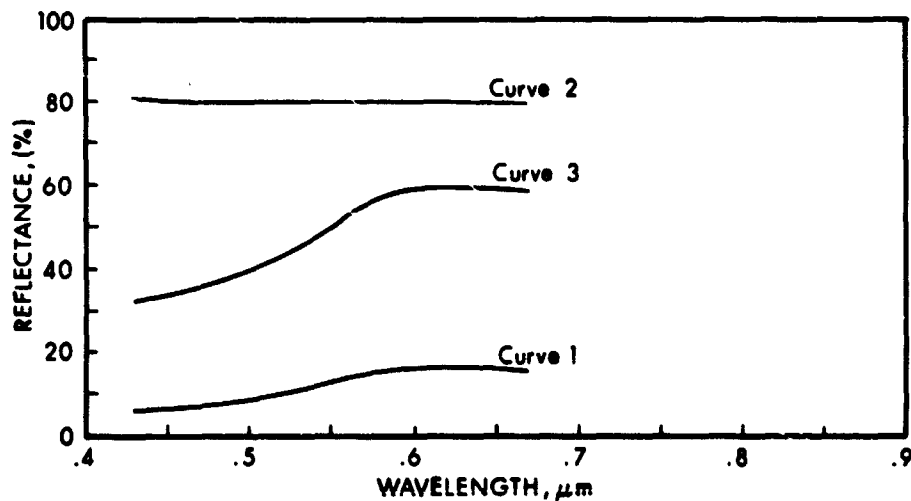


Figure B-10 Reflectances for Salt Crust. (Curve 1 is Dark Area of the Kel,-Kor Shor (Salt Lake), Curve 2 is Fresh and Moist Salt Crust in the Kel, -Kor Shor Area and Curve 3 is Soiled by Sand and Dust, Bed of the Aktam River.)
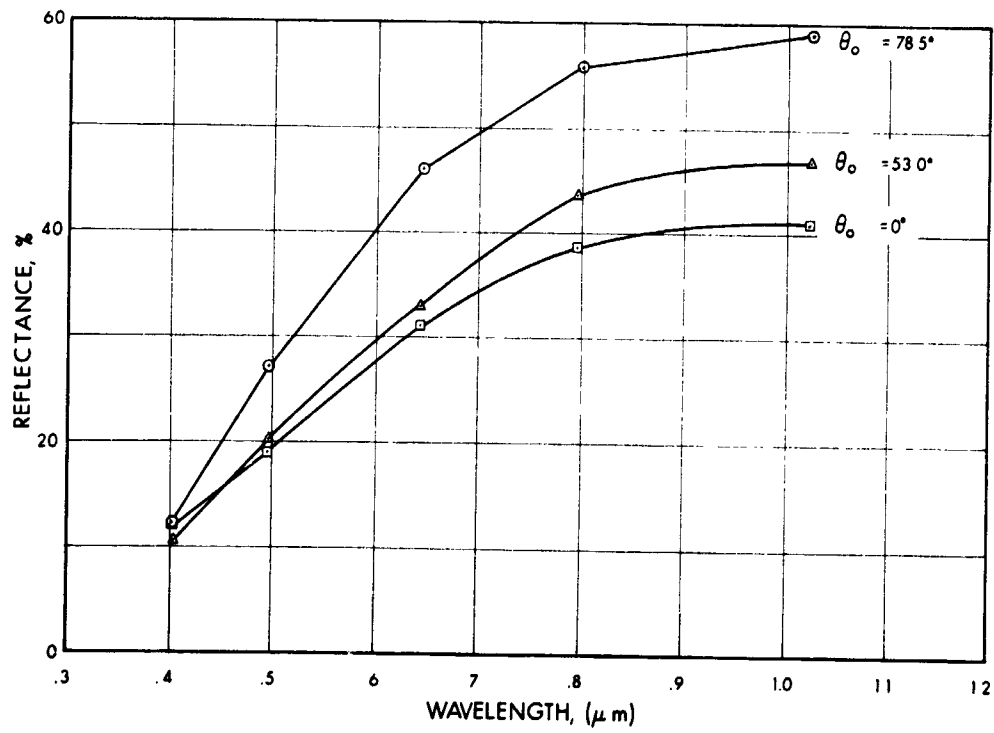
Figure B-11  Reflectance of Desert Sand at the Nadir, for 0°, 53° and 78.5° Solar Nadir Angles
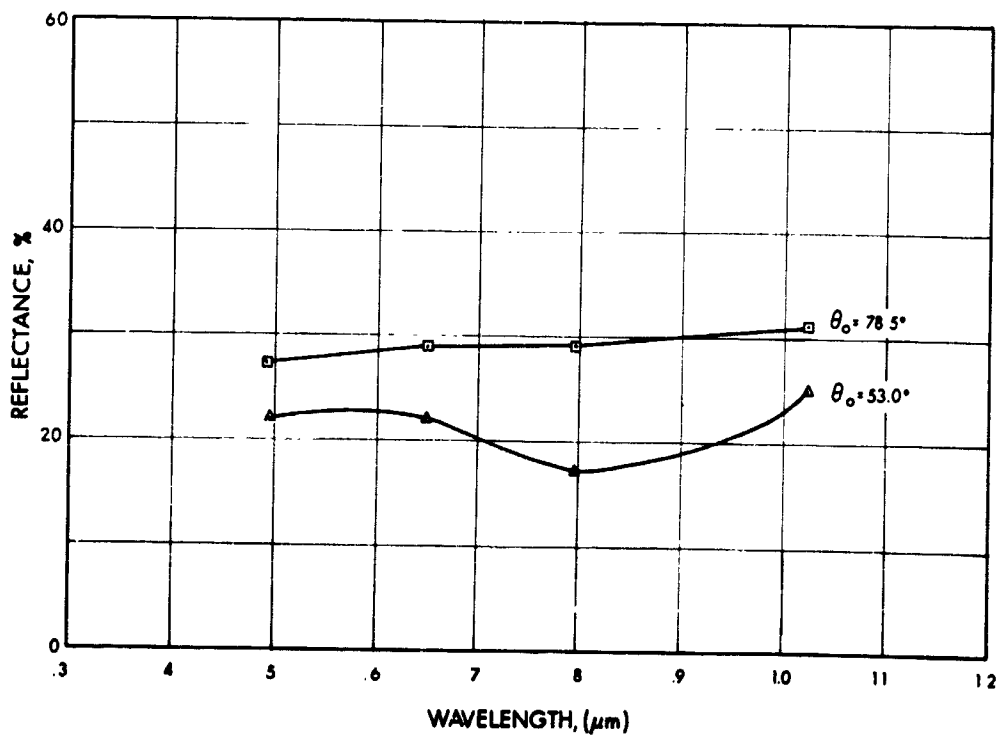


Figure B-12  Reflectance of Crushed Limestone (1/2 to 3/4 inch) at the Nadir, for 53° and 78.5° Solar Nadir Angles
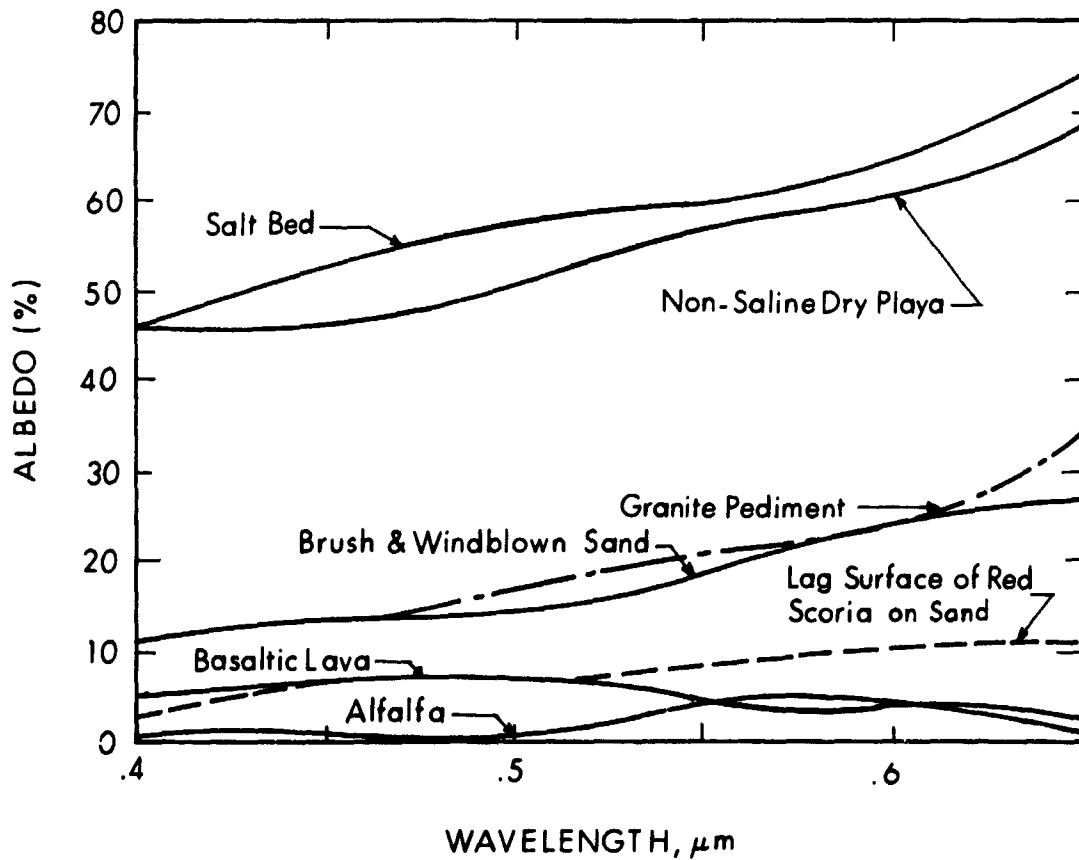
Figure B-13 Diffuse Reflectance of Representative Types of Desert Surfaces
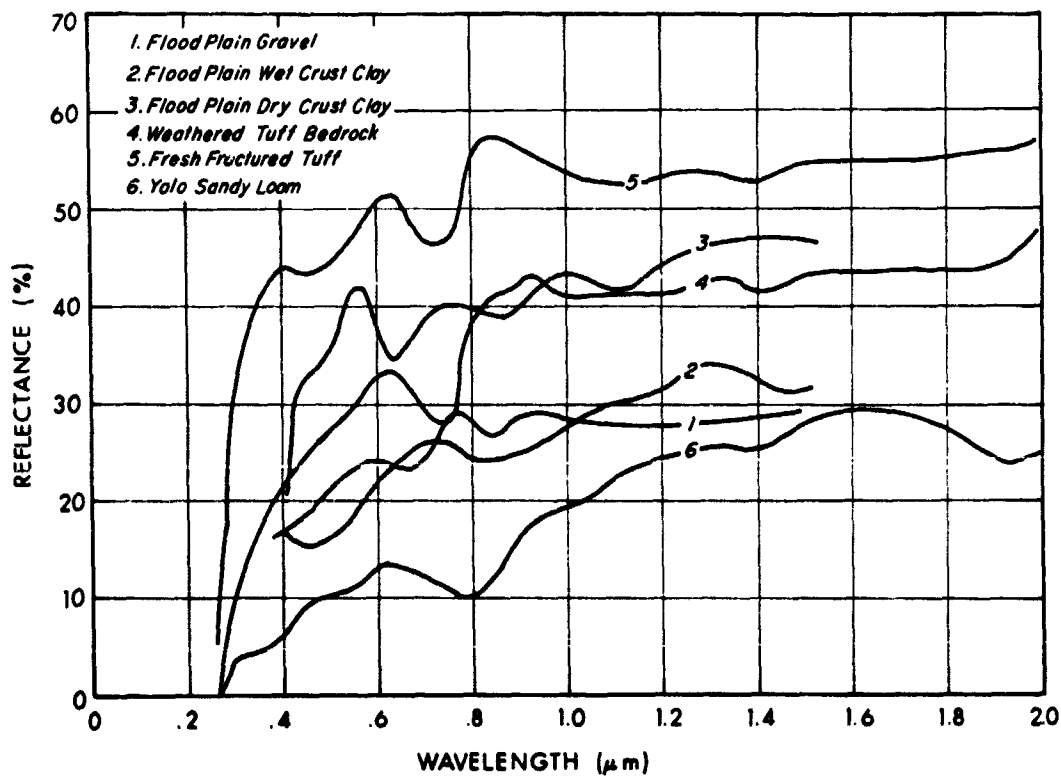


Figure B-14 Reflectance Curves for Soils and Rocks
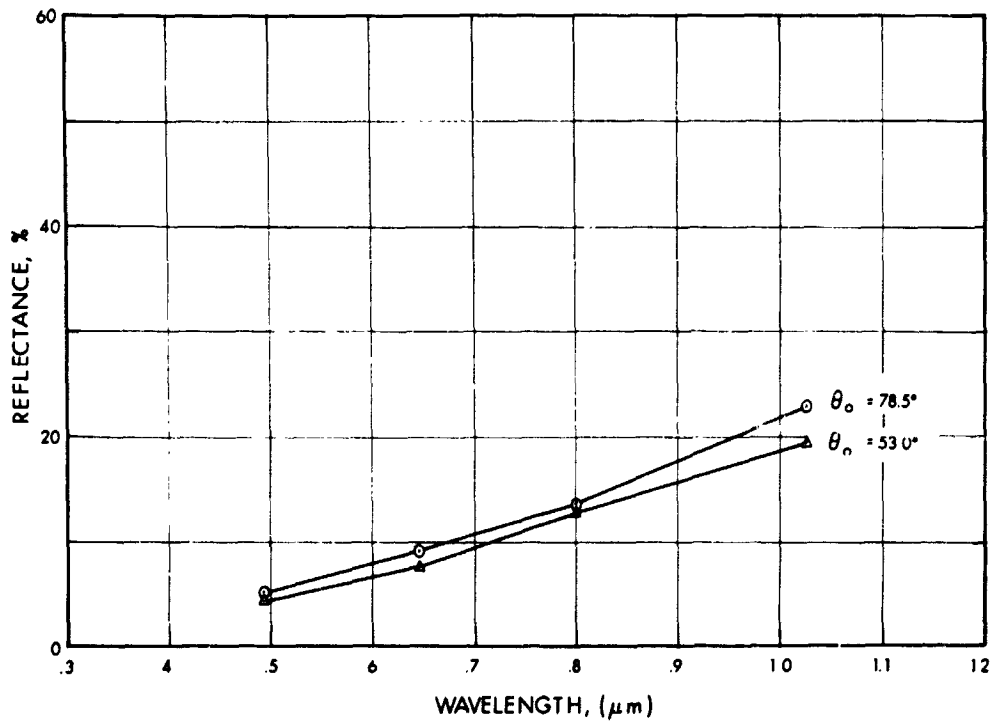
Figure B-15 Reflectance of Black Loam Soil at the Nadir, for 53° and 78. 5° Solar Nadir Angles
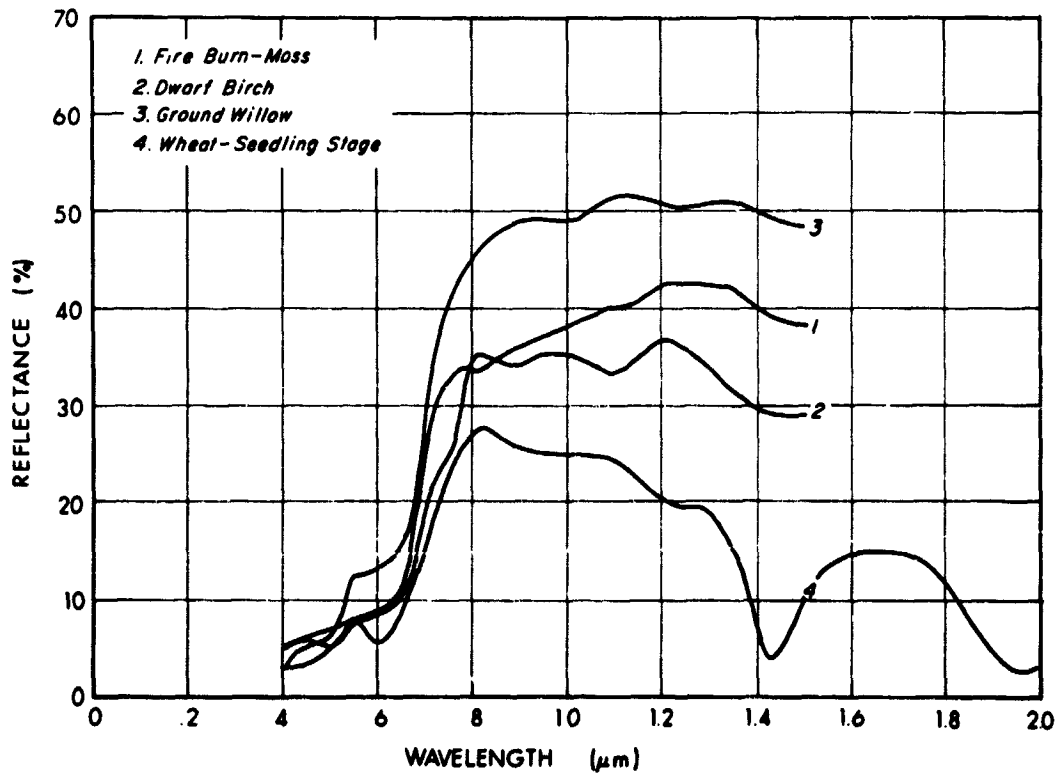


Figure B-16 Spectral Reflectance Curves for Vegetation

81
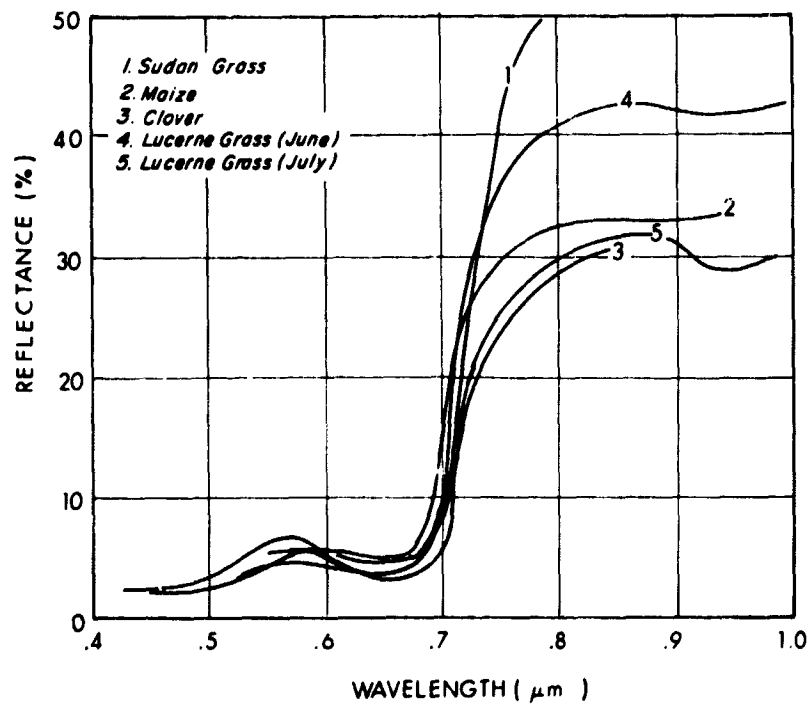
Figure B-17 Spectral Albedo of Different Vegetation
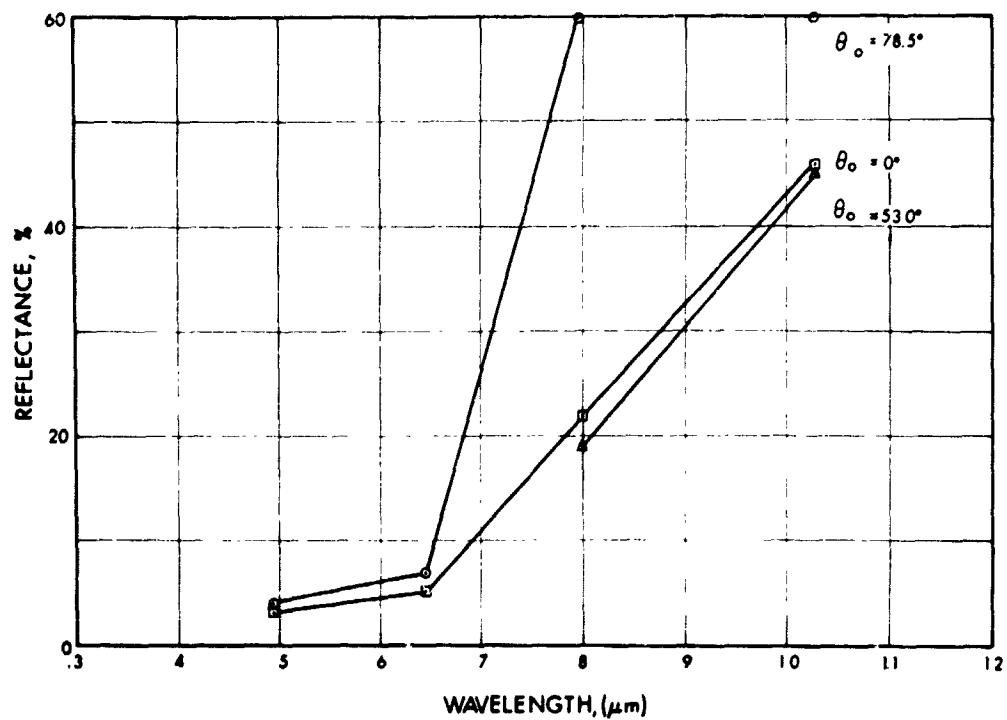


Figure B-18  Reflectance of Clipped Green Grass at the Nadir
for $0°$, $53°$ and $78.5°$ Solar Nadir Angles
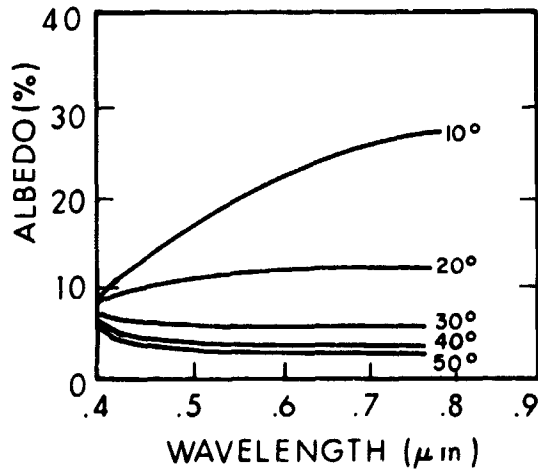
Figure B-19 Spectral Albedo of Water for Total Radiation for a
Cloudless Sky as a Function of Solar Altitude
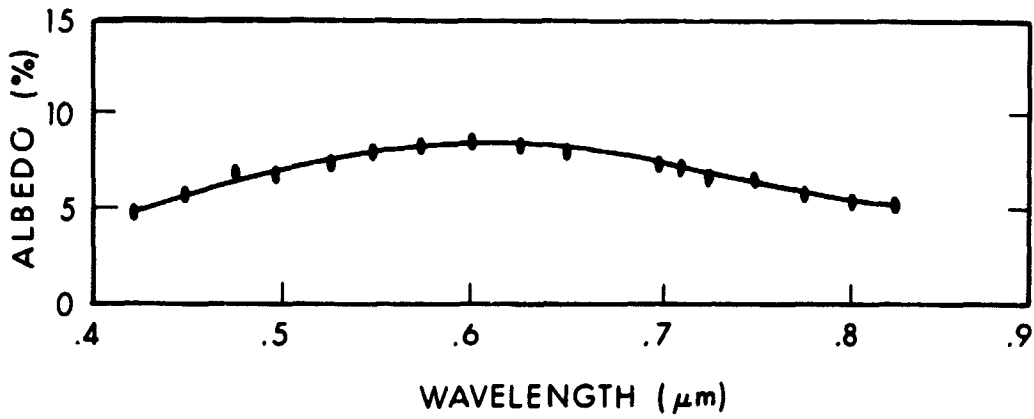


Figure B-20 Spectral Albedo of a Water Surface. (Measured over a
Lake with Depth of 60 to 70 cm.)
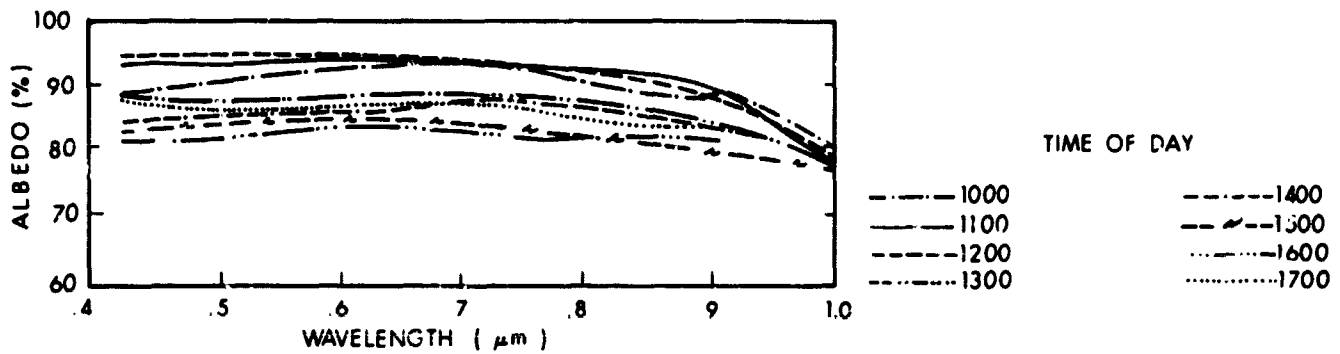


Figure B-21 Spectral Albedo of Snow Cover (Dry Snow) in Clea. Weather,
1963

# APPENDIX B

## REFERENCES

1. Earing, D. G. and J. A. Smith, 1966: Target Signature Analysis Center Data Compilation, Willow Run Labs., The University of Michigan.

2. Steiner, D. and T. Guterman, 1966: Russian Data on Spectral Reflectance of Vegetation Soil and Rock Types, European Research Office, U S Army, Contract DA-91-EUC-3863/OI-652-0106.

3. Coulson, K. L., G M Bouricius and E. L. Gray, 1965: Effects of Surface Reflection on Radiation Emerging from the Top of a Planetary Atmosphere, Report No. R65-SD64, Space Sciences Laboratorv, General Electric Company, Philadelphia (G65-80148), 147 p.

4. Ashburn, E. V. and R G Weldon, 1956: "Spectral Diffuse Reflectance of Desert Surfaces," JOSA, 46, 583-586, No. 8.

5. Krinov, E. L., 1947: "Spectral Reflectance Properties of Natural Formations," (in Russian): Translation by National Research Council of Canada, TT-439, Ottawa (1953).

6. Orr, D. G., S. E Dwornik and L. M. Young, 1963: Reflectance Curves of Soils, Rocks, Vegetation and Pavement, Research Report No. 7746-RR, U S Army Engineer Research and Development Laboratories, Fort Belvoir, Va., AD 410588.

7. Kropotkin, M A. and B. P. Kozyrev, 1964: "Study of the Reflection Spectra of Natural and Synthetic Materials in the .7 - 100 Micron Range," Optics and Spectroscopy, 17. 136.

8. Kondrat'yev, K. Y., 1965: "Actinometry" (in Russian), NASA Technical Translation F-9712.

9. Kondrat'yev, K. Y., Z. F Mironova and A N. Otto, 1964: "Spectral Albedo of Natural Surfaces," Pure and Applied Geophysics, 59, 207-216.

APPENDIX C

SPECTRAL REFLECTANCE OF TEST SITE SURFACE COVERS

C.1    Semi-Desert and Desert Vegetation[1]

The plants of the semi-desert and desert zone can. with respect to their reflectance characteristics, be broken down roughly into two groups:

1.    Mesophytic plants are dark and cover the soil densely.

2.    Xerophytic and halophytic plants are light in tone;  their leaves are narrow or absent completely and they may be covered by salt precipitations.

Semi-Desert and desert plants undergo seasonal changes.   The most sensitive of these changes are those due to pigmentation and to surface effects.   Relatively slight changes in pigmentation will appear in the quality of the visible spectral reflectance.   Pigmentation changes, such as leaf chlorosis, can occur because of abnormal soil chemistry.   During summer, the vegetation on the higher lying terrain dries out and becomes sparse.   At the same time, the vegetational cover in depressions is still dense and green.   Later in the year, the meadow vegetation in the depressions may also turn its color and become less dense.   Due to the high reflectance of the bare soil, however, the contrast between the sparsely vegetated depressions and bare upland is then enhanced rather than reduced.

For the infrared spectral region only a few data are available.   Nothing can be said with respect to a comparison of the infrared reflectance of the two vegetation groups mentioned above.   It can be concluded, however, that contrasts between soils and vegetation are lower in the infrared than in the visible region.   The red spectral band often separates vegetation and soils.   In some cases, however, this may give excessive contrasts, as for sand areas, for example, where the ratio between the brightness of bare sand in the red wavelengths and that of vegetation may be as high as 5:1.

Data on the reflectance of vegetation and soil types over fresh or saline ground water have been compiled for spectral intervals shown in Table C-1.

---

[1] The material in this subsection is largely taken from Ref. 2.   The reader is referred to this book for a more comprehensive treatment of this subject.

TABLE C-1

REFLECTANCE OF DESERT VEGETATION AND SOIL TYPES

| Type of indicator | Reflectance in % | | | |
|---|---|---|---|---|
| Spectral Region | Blue | Green | Red | Visible |
| Wavelength (μm) | 0.43-0.49 | 0.51-0.59 | 0.61-0.69 | 0.43-0.69 |
| **Over Fresh Ground Water** | | | | |
| Meadow chestnut soil | 8.5 | 11.7 | 13.6* | 11.3* |
| Crested wheat grass | 3.9 | 5.8 | 7.5* | 5.7* |
| Couch grass (probably quack grass) | 3.0 | 4.9 | 7.8* | 5.3* |
| Barkhan sand, top a | 17.5 | 23.3 | 28.3 | 23.4 |
| id., top b | 13.8 | 20.5 | 26.6 | 20.8 |
| id., slope | 10.0 | 15.8 | 18.5 | 15.1 |
| Stable cover sand | 11.2 | 13.2 | 14.8 | 13.2 |
| Deflation basin with vegetation | 7.2 | 8.6 | 9.4 | 8.5 |
| Reed | 5.3 | 8.8 | 5.1 | 6.5 |
| Camel's thorn | 4.3 | 7.6 | 6.1 | 6.1 |
| Tamarisk | 3.5 | 7.4 | 6.6 | 6.0 |
| Ruderal herbs on flood plain | 2.7 | 7.8 | 4.1 | 5.0 |
| Couch grass association | 1.7 | 5.0 | 3.5 | 3.5 |
| Sand polyn | 6.0 | 8.0 | 7.0 | 7.1 |
| Woodreed and blue grass | 5.4 | 7.5 | 6.1 | 6.4 |
| Licorice | 4.6 | 6.8 | 5.2 | 5.6 |
| **Over Saline Ground Water** | | | | |
| Saline meadow-chestnut soil | 12.4 | 15.8 | 19.0* | 15.7* |
| Wormwood (probably black polyn) | 6.6 | 10.3 | 12.2* | 9.7* |
| Salt-tolerating couch grass | 7.0 | 10.0 | 12.4* | 9.8* |
| Bijurgun association | 9.0 | 14.0 | 15.6 | 13.1 |
| White polyn association | 3.2 | 6.8 | 7.2 | 5.9 |
| White polyn | 7.4 | 10.3 | 9.2 | 9.1 |
| Old river bed | 12.8 | 15.3 | 17.4 | 15.3 |
| Annual saltwort | 10.1 | 14.4 | 14.8 | 13.3 |

* Data incomplete for spectral interval specified.

(Steiner, D. and T. Guterman, Ref. 2.)

It should also be noted that reflectance measurements taken on single plant leaves or branches do not permit reliable predictions of photographic tones. The reflectance measurements should be on whole plants or groups of plants. Due to the relatively low density of many individual plants and of the vegetational cover as a whole, the underlying soil surface will always affect the measurements. This may explain the flatness of many spectral reflectance curves without the clear maximum and minima otherwise typical for vegetation.

Laboratory and in situ measurements by Coulson and others (Refs. 3 through 6) have shown that visible and near-infrared reflectances of grass, soil, and sand surfaces depend on the angle of incident radiation. This dependence increases markedly at angles of $>78.5°$, especially in the infrared and for grass and desert sand (see Figures B-11, B-12, B-15 and B-18 of Appendix B).

The reflectance, R, of a soil area, A, which is partially covered with vegetation may be expressed simply as

$$R = \frac{A_v R_v + A_s R_s}{A} \tag{1}$$

where

v refers to vegetation

and s refers to soil.

Soils usually have higher reflectances than plants in the visible, thus a surface of mixed bare soil and vegetation will reflect less than bare soil. However, the reverse is true in the near-infrared where plants have a higher reflectance than soil.

C.2 Soils

### Reflectance as a Function of Soil Texture [2]

Generally a decrease of grain size results in an increase of reflectance when measured by ground-based sensors. This increase is caused by heavier light scattering and lower extinction of light passing through the particles. Also, the area covered by microshadows occurring between particles under oblique

---

[2] The reader is referred to Ref. 2 for a more comprehensive review of this subject and a definition of terms.

87

illumination becomes smaller. This fact is in contrast to experiences made with air photographic tones. On air photos, finely textured soil materials usually have a darker tone than coarse soils. This, however, is the result of either a higher water retention or a higher content of organic matter or both in the former; i. e., differences in soil moisture and humus content in general overshadow differences in soil texture.

The shape of the spectral curves does not change very much from one grain size category to another. Quartz, biotite and muscovite have neutral colors in all cases. A slight change of color can be observed for microcline and epidote.

### Reflectance as a Function of Soil Moisture

The effect of soil moisture on reflectance is summarized below and is graphically illustrated in Figures C-1 and C-2.

1. Dry soils have the highest reflectances. The maximum reflectance, however, depends on the type of soil. Sandy soils having higher reflectances than loamy soils.

2. Until the hygroscopic (absorbed) moisture content is reached, there is almost no change of reflectance.

3. Additional moisture (above the hygroscopic limit) results in a marked decrease of reflectance. It is caused by the excess water which surrounds the soil particles and fills the voids between particles.

4. The change from low to high reflectance also depends on the type of soil (Figure C-1). For sandy loams this change occurs between 0.3 and 2-3% (Curve 1), for light clay loams between 2.0-2.5 and 11-12% (Curve 14a), for clays between 4-5 and 20-25% (Curve 14), and for humic blue-gray soils between 7 and 30% (Curves 77 and 104) of moisture capacity in a sample.

5. The magnitude of reflectance fluctuation also depends on soil type. The decrease of brightness is greatest for dark soils; i. e., soils having a high humic content. For example, the reflectance of the blue-gray saline soil No. 104 (Figure C-1) is a common chernozem, the corresponding drop is from 12 to 5% only.

6. When the soils are covered by a thin film of water, reflectance rises again due to specular reflection.

As far as the color of soils being affected by a change of moisture is concerned, except for a slight tendency of the yellow-red component to become more pronounced relative to the remainder of the spectrum, the shape of the curves does not change with an alteration of the moisture content. It can be concluded that the color of soils is not influenced significantly by a variation of moisture.

### Reflectance as a Function of Humus and Iron Oxide Content

The spectral characteristics of iron oxides depend very much on the degree of oxidation and hydration of the iron ions. Magnetite $(Fe_3O_4)$, being a mixture of bivalent and trivalent iron, is black with a slight blue-green tint as can be seen from the maximum in Curve 2 of Figure C-3 near 0.45 $\mu$m. Hermatite $(Fe_2O_3)$, on the other hand, is colored distinctly red and the reflectance increases from about 2-1/2% in the blue (near 0.50 $\mu$m) to about 13% in the red region (near 0.65 $\mu$m), Curve 1 of Figure 3. For a comparison, see also the similar curve for limonite $(Fe[OH]_3)$ in Curve 3 of Figure C-3.

Humus and iron oxides are both distributed in the soil in colloidal form and coat the mineral grains and microaggregates as a thin veneer. When their content is low, a large part of the grain surfaces is uncovered, and a small change of the amount of humus and iron oxide may bring about a considerable change of brightness. Once the particles are covered, however, an increase in the humus-iron oxide percentage has practically no visible effect any more.

The spectral reflectance characteristics of soils are governed basically by the ratio of humus to iron oxide. For a low ratio, spectral curves have, in general, a distinct maximum in the red spectral zone, because then the color of $Fe_2O_3$ dominates. An increase of the humus content relative to the iron oxide, i. e., an increasing ratio, levels out the spectral curve more and more. In addition, the type of the organic material present in the soil has also an influence on the spectral distribution of reflected light. Soils with a dominance of fulvic acid, for example, reflect more intensively in the red band than in the rest of the visible spectrum.

### Reflectance as a Function of Mineralogical Composition of Soils

Average percentage reflectance of the blue, the green and the red spectral interval, as well as for the whole visible spectrum, are given in Table C-2. Quartz, biotite and muscovite are completely spectrally neutral or nearly so, whereas microcline, garnet and epidote have curves which slope upward from
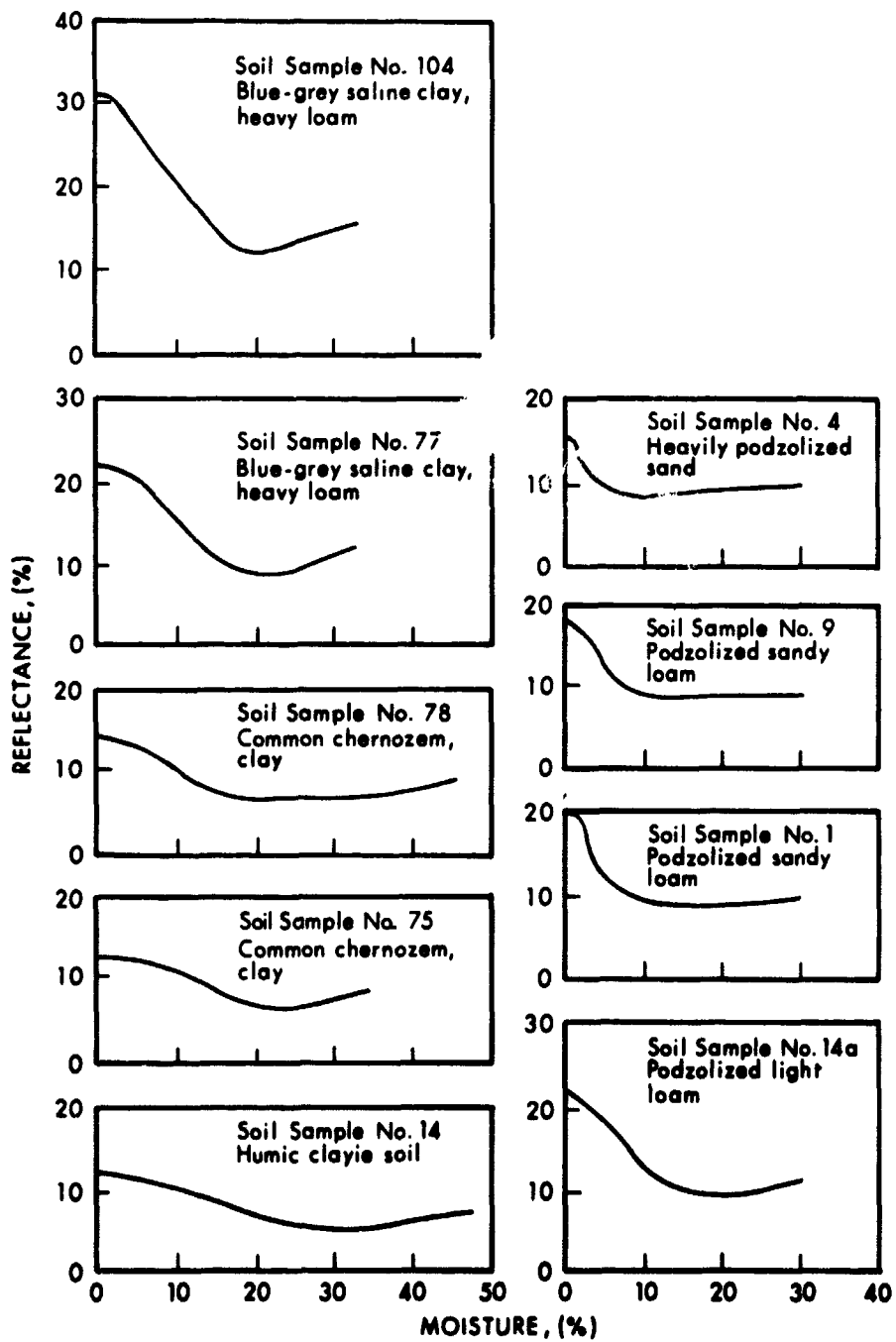
89

Figure C-1    Dependence of Visible Light Reflectance on Soil
Moisture Content for a Number of Soil Types
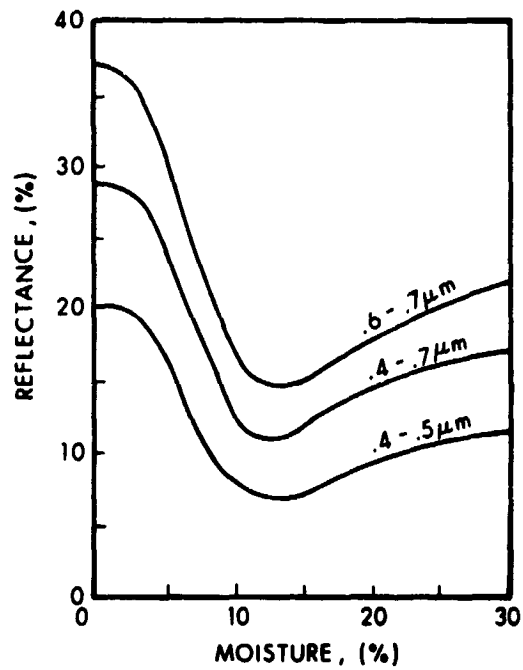
Figure C-2    Dependence of Light Reflectance on Soil Moisture
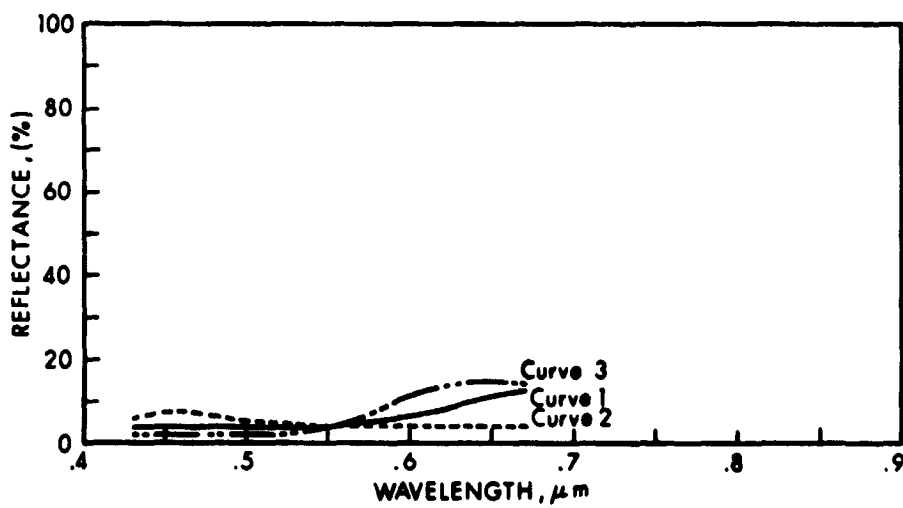              for Takyr Soils



Figure C-3    Comparison of Reflectances for Magnetite, Hematite
              and Limonite

91

the blue to the red part of the spectrum. Also, orthoclase has a maximum in the yellow and red region. The differences with respect to general brightness are great, quartz being the brightest (93% reflectance) and biotite the darkest (7%) among the minerals investigated.

TABLE C-2

REFLECTANCE OF VARIOUS MINERALS FOR THE 0.01 mm GRAIN
FRACTION IN SELECTED SPECTRAL INTERVALS

| Mineral Spectral Region Wavelength ($\mu$m) | Reflectance in % | | | |
|---|---|---|---|---|
| | Blue 0.43-0.49 | Green 0.51-0.59 | Red 0.61-0.67 | Visible 0.43-0.67 |
| Quartz | 92.9 | 93.0 | 93.5 | 93.1 |
| Biotite | 7.4 | 7.4 | 7.4 | 7.4 |
| Muscovite | 59.3 | 60.3 | 60.2 | 60.0 |
| Microcline | 61.4 | 71.7 | 80.7 | 71.3 |
| Garnet | 11.0 | 18.3 | 30.3 | 19.7 |
| Epidote | 18.6 | 34.7 | 36.5 | 30.3 |

(Steiner, D. and T Guterman, Ref. 2.)

It must be expected that, as a result of these variations, soils forming on dissimilar lithologies will show up differently on aerial photographs. And, in fact, soils having different spectral intensities do show up visually in different color tones. Mineralogical influence on spectral reflectance and, hence, on color should not be over-estimated, however. Differences in spectral reflection characteristics are not only caused by variations in the content of minerals, but also by other factors, among these especially humus, iron oxide concentration, and degree of weathering.

Reflectance as a Function of Soluble Salt Content

Soils in arid areas may have a high salt content which affects reflectance. This influence is especially promounced if a salt crust is formed on the soil surface. Figure C-4 shows the spectral reflectance curves for three types of soluble salts common in soils; namely, sodium carbonate ($Na_2CO_3$), Curve 1; sodium chloride ($NaCl$), Curve 2; potassium hydrogen sulfate ($KHSO_4$), Curve 3.

All these salts, being white materials, have an almost uniform and very high reflectance (65 to 89%) throughout the whole visible spectrum. As a result of this color neutrality, soils containing free salts do not change their spectral characteristics unless the salts form a superficial crust, thus becoming considerably brighter.

### Reflectance as a Function of Surface Structure

Differences in physical and chemical properties of soils manifest themselves in differences of surface structure. For example, the surface of common chernozems (black soils) is, in general, flat and has only a few narrow cracks here and there. Heavily solonized (saline) chernozems on the other hand have a clumpy structure with large cracks. Solonetz (saline) soils are criss-crossed by a dense network of desiccation cracks with smooth polygons in between. The surface of solonchaks (saline) is almost structureless and covered by salt precipitates.

The presence of microshadows causes rough surfaces to appear as a mosaic of bright and dark areas. This will probably be below the resolution of the ERTS data and therefore be relatively unimportant. They are discussed here in the context of the more general subject of ground reflectance. One factor governing the overall reflectance of such surfaces is the intensity of light re-emission from individual shadow and light areas. The shadow areas, i. e. , areas not receiving direct sunlight, have a brightness which is about ten times lower than that of areas illuminated by the sun. Deep and wide cracks on the soil surface are even darker.

As far as the general brightness is concerned, the smooth surface reflects light most intensively, followed by the surface with furrows parallel and that with furrows perpendicular to the direction of cast shadows. The differences are small, however. It seems that, in the last case, the lower brightness of the shadow areas is almost fully compensated for by the higher brightness of the sloping surfaces exposed to full sunlight. Color is also not appreciably affected by surface structure.

### C. 3    Influence of Weathering on Surface Reflectance

In most cases, the spectral reflectance of undisturbed surface covers is different from that of freshly uncovered surfaces (surface stripped off its surficial veneer). The reasons are the following:

1.  A thin cover of foreign material deposited by wind or water may overlie the surface.

2.  Lichens may grow on rocks. Due to the color of this vegetational cover, the color of the rock surface does not alter significantly, but its brightness drops by a factor of about 2.5.

3.  As a result of the weathering process, the soil and rock surface is partly destroyed; fissures develop and easily soluble or nonresistant components are removed. Generally, the brightness of the weathered rock surface is considerably higher.

4.  A thin salt crust consisting of easily soluble salts, such as sodium chloride, sodium sulfate, magnesium sulfate or gypsum may develop on the surface. These typical solonchak salts are usually washed away during rains and since they are typical for dry saline areas only, compensation may easily be made for them.

5.  In very hot areas desert varnish may be formed. Figure C-5 shows a comparison of the reflectance of unweathered volcanic rock of yellow-green color (Curve 1) with that of the same type of rock covered by black desert varnish (Curve 2). Accordingly, the general brightness of the varnished rock drops and the spectral reflectance curve assumes a more neutral shape.

The differences in the mineralogical composition of rocks, which originally give rise to differences in spectral reflectance characteristics, may be leveled out during the process of soil formation. After some time, all materials approximate a final weathering product which is rich in colloidal particles and colored by iron compounds.
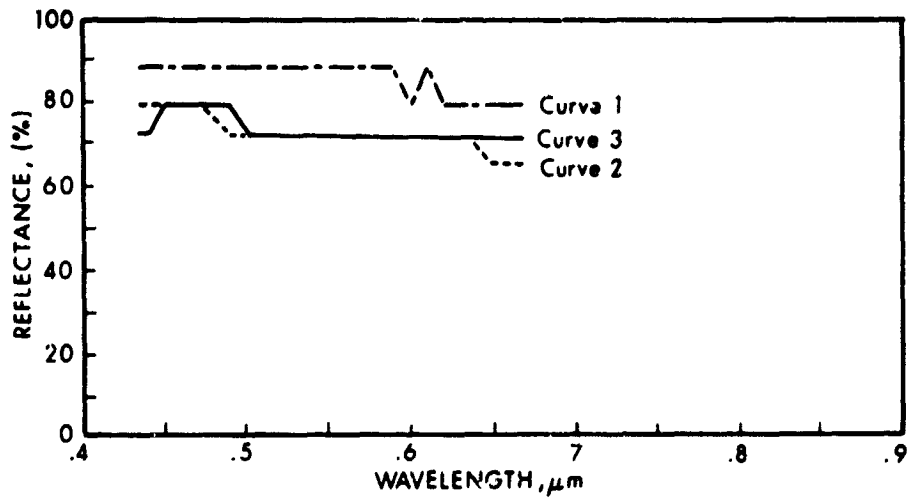
94

Figure C-4    Comparison of Reflectances for Sodium Carbonate,
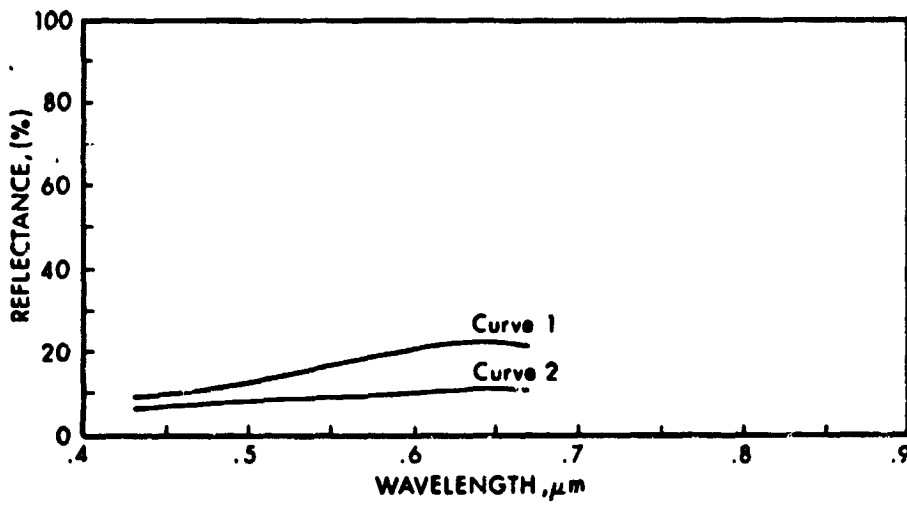Sodium Chloride and Potassium Hydrogen Sulfate



Figure C-5    Comparison of Reflectances of Unweathered
and Weathered (Varnished) Volcanic Rock

PRECEDING PAGE BLANK NOT FILMED

APPENDIX C

REFERENCES

1.  Shay, J. R. (ed), 1970: <u>Remote Sensing, with Special Reference to Agriculture and Forestry</u>, National Academy of Sciences, Washington, D. C

2.  Steiner, D. and T. Guterman, 1966: <u>Russian Data on Spectral Reflectance of Vegetation, Soil, and Rock Types</u>, European Research Office, U. S Army, Contract DA-91-591-EUC-3863/OI-652-0106.

3.  Coulson, K. L., G. M. Bouricius and E. L. Gray, 1965: "Optical Reflection Properties of Natural Surfaces," <u>J. of Geophysical Research</u>, <u>70</u>, 4601-4611.

4.  Coulson, K. L., 1966: "Effects of Reflection Properties of Natural Surfaces in Aerial Reconnaissance," <u>Appl. Optics</u>, <u>5</u>, 905-917.

5.  Coulson, K. L., 1968: "Effect of Surface Reflection on the Angular and Spectral Distribution of Skylight," <u>J. of Atmos. Sci.</u>, <u>25</u>, 759-770.

6.  Coulson, K. L., G. M. Bouricius and E L. Gray, 1965: <u>Effects of Surface Reflection on Radiation Emerging from the Top of a Planetary Atmosphere</u>, Report No. R65-SD64, Space Sciences Laboratory, General Electric Company, Philadelphia, 147 p, (G65-80148).

7.  LeGault, R, 1970: <u>Sources of Electromagnetic Radiation</u>, AIAA Paper No. 70-287, Annapolis, Md.